

**Stable Haptic Interaction with Virtual Environments**

by

**Richard J. Adams**

A dissertation submitted in partial fulfillment of the  
requirements for the degree of

**DOCTOR OF PHILOSOPHY**

University of Washington

1999

Program Authorized to Offer Degree: Department of Electrical Engineering

19991108 128

REPORT DOCUMENTATION PAGE			Form Approved OMB No. 0704-0188	
Public reporting burden for this collection of information is estimated to average 1 hour per response, including the time for reviewing instructions, searching existing data sources, gathering and maintaining the data needed, and completing and reviewing the collection of information. Send comments regarding this burden estimate or any other aspect of this collection of information, including suggestions for reducing this burden, to Washington Headquarters Services, Directorate for Information Operations and Reports, 1215 Jefferson Davis Highway, Suite 1204, Arlington, VA 22202-4302, and to the Office of Management and Budget, Paperwork Reduction Project (0704-0188), Washington, DC 20503.				
1. AGENCY USE ONLY (Leave blank)	2. REPORT DATE 19.Oct.99	3. REPORT TYPE AND DATES COVERED DISSERTATION		
4. TITLE AND SUBTITLE STABLE HAPTIC INTERACTION WITH VIRTUAL ENVIRONMENTS		5. FUNDING NUMBERS		
6. AUTHOR(S) CAPT ADAMS RICHARD J				
7. PERFORMING ORGANIZATION NAME(S) AND ADDRESS(ES) UNIVERSITY OF WASHINGTON		8. PERFORMING ORGANIZATION REPORT NUMBER		
9. SPONSORING/MONITORING AGENCY NAME(S) AND ADDRESS(ES) THE DEPARTMENT OF THE AIR FORCE AFIT/CIA, BLDG 125 2950 P STREET WPAFB OH 45433		10. SPONSORING/MONITORING AGENCY REPORT NUMBER  FY99-293		
11. SUPPLEMENTARY NOTES				
12a. DISTRIBUTION AVAILABILITY STATEMENT Unlimited distribution In Accordance With AFI 35-205/AFIT Sup 1		12b. DISTRIBUTION CODE  <b>DISTRIBUTION STATEMENT A</b> <b>Approved for Public Release</b> <b>Distribution Unlimited</b>		
13. ABSTRACT (Maximum 200 words)				
14. SUBJECT TERMS			15. NUMBER OF PAGES 122	
			16. PRICE CODE	
17. SECURITY CLASSIFICATION OF REPORT	18. SECURITY CLASSIFICATION OF THIS PAGE	19. SECURITY CLASSIFICATION OF ABSTRACT	20. LIMITATION OF ABSTRACT	

University of Washington

Abstract

Stable Haptic Interaction with Virtual Environments

by Richard J. Adams

Chairperson of the Supervisory Committee

Professor Blake Hannaford

Department of Electrical Engineering

A haptic interface is a kinesthetic link between a human operator and a virtual environment. It allows the user of a virtual reality system to 'feel' objects in a virtual world. This dissertation addresses fundamental stability and performance issues associated with haptic interaction. It generalizes and extends the concept of a virtual coupling network, an artificial link between the haptic display and a virtual environment, to include both impedance and admittance models of haptic interaction. A benchmark example is used to expose an important duality between these two cases. Linear circuit theory is employed to develop necessary and sufficient conditions for the stability of a haptic simulation, assuming the human operator and virtual environment are passive. This approach leads to design procedures for virtual coupling networks which give maximum performance while guaranteeing stability.

Two-port absolute stability criteria are used to develop explicit control law design bounds for three detailed haptic display implementations: the basic impedance display, the impedance display with force compensation, and the admittance display. The strengths and weaknesses of each approach are illustrated through numerical and experimental results for two different haptic devices: the planar High Bandwidth Force Display and the Excalibur three-axis force display. The examples highlight the ability of the proposed design approach to handle some of the most difficult problems in control law synthesis for haptics, including structural flexibility and non-collocation of sensors and actuators. Good agreement is observed between theoretically predicted and experimental results.

An absolutely stable haptic interface, designed using these methods, is the centerpiece of a Virtual Building Block training study. This study investigates the benefits of haptic feedback for training a manual task in a virtual environment. Three groups of test operators are exposed to different treatments before being asked to build a LEGO™ biplane model: virtual training with force feedback, virtual training without force feedback, and no training. Results show training with haptic feedback has a significant impact on performance in the manual real-world task.



## TABLE OF CONTENTS

List of Figures.....	iii
List of Tables.....	v
Chapter 1 An Introduction to Haptics.....	1
1.1 Touch and the “Sixth Sense” .....	1
1.2 Haptic Displays.....	2
1.2.1 The Early Years.....	2
1.2.2 Into the 90’s and Beyond.....	3
1.3 Keeping Things Under Control.....	8
Chapter 2 State-of-the-Art in Control of Haptic Interfaces.....	9
2.1 The Foundation, Control for Telerobotics.....	9
2.2 Modern Haptics.....	10
2.3 New Contributions.....	13
Chapter 3 Review of Network Theory.....	14
3.1 Network Representations .....	14
3.2 Analog Systems.....	15
3.3 Two-Port Representations.....	18
3.4 Duality.....	20
3.5 Stability .....	24
Chapter 4 Two-Port Framework for Haptic Interaction.....	29
4.1 The Human Operator.....	30
4.2 The Virtual Environment.....	32
4.3 The Haptic Interface.....	36
4.3.1 The Haptic Display.....	36
4.3.1.1 Impedance Displays.....	36
4.3.1.2 Admittance Displays.....	37
4.3.2 Virtual Coupling Network.....	38
4.4 Performance.....	40
4.5 Human-Virtual Environment Coupling.....	41
Chapter 5 Benchmark Problem.....	43
5.1 Impedance Display.....	43
5.1.1 Conventional Design.....	44
5.1.2 Proposed Design Procedure.....	46
5.2 Admittance Display.....	50
5.2.1 Conventional Design.....	51
5.2.2 Proposed Design Procedure.....	51
5.3 Duality .....	56
5.4 Extensions .....	57
Chapter 6 Advanced Implementations.....	58
6.1 Device Model.....	58
6.2 Haptic Display Implementations.....	59
6.2.1 Impedance Display - Basic.....	59
6.2.2 Impedance Display - with Force Compensation.....	61

6.2.3 Admittance Display.....	63
6.3 Virtual Coupling Implementations.....	64
6.4 Design for Absolute Stability.....	66
6.4.1 Impedance Display - Basic.....	66
6.4.2 Impedance Display - with Force Compensation.....	67
6.4.3 Admittance Display.....	70
6.4.4 Impact of Human Model on Stability Conditions.....	71
6.5 Performance.....	71
6.5.1 Impedance Display - Basic.....	72
6.5.2 Impedance Display - with Force Compensation.....	72
6.5.3 Admittance Display .....	72
Chapter 7 Design and Experimental Results for the High-Bandwidth Force Display.....	73
7.1 Modeling.....	74
7.2 Design for Absolute Stability.....	75
7.2.1 Impedance Display - Basic.....	75
7.2.2 Admittance Display.....	76
7.3 Experimental Results.....	77
7.4 Performance.....	80
Chapter 8 Design and Experimental Results for the Excalibur Haptic Display.....	82
8.1 Modeling.....	83
8.2 Design for Absolute Stability.....	84
8.2.1 Impedance Display - Basic.....	84
8.2.2 Impedance Display - with Force Compensation.....	85
8.2.3 Admittance Display.....	87
8.3 Experimental Results.....	88
8.4 Performance.....	90
Chapter 9 Virtual Building Block Training Study.....	95
9.1 Motivation.....	96
9.2 Apparatus .....	97
9.2.1 Excalibur Force Display.....	97
9.2.2 Virtual Building Block Software.....	98
9.3 Experimental Design.....	99
9.3.1 Matching Test.....	100
9.3.2 Treatments.....	102
9.3.3 Experimental Procedure.....	102
9.4 Results.....	103
9.4.1 Analysis of Variance.....	104
9.4.2 Post Hoc Analysis - Tukey HSD.....	106
9.4.3 Discussion.....	108
Chapter 10 Conclusions and Future Work.....	110
References.....	112

## LIST OF FIGURES

<i>Number</i>	<i>Page</i>
1.1 The PHANToM Haptic Display.....	4
1.2 The Pen-Based Force Display .....	5
1.3 The High-Bandwidth Force Display .....	6
1.4 Excalibur .....	6
3.1 A One-Port Network .....	15
3.2 Two-Port Analog Systems .....	20
3.3 Dual Network Construction .....	23
3.4 Terminated Two-Port Network .....	25
3.5 Two-Port Network Terminated by One-Port Networks .....	26
3.6 Stability-Activity Diagram .....	28
4.1 Network Model of Haptic Simulation .....	29
4.2 Stable Haptic Simulation .....	30
4.3 Human Operator Impedance Model .....	32
4.4 Revised Network Model of Haptic Simulation .....	33
4.5 Stable Haptic Simulation with Virtual Environment Activity and Human Impedance Models .....	35
4.6 Haptic Interface Two-Port .....	36
4.7 McGill University Pantograph .....	37
4.8 A PUMA-based Haptic Display .....	38
4.9 Spring-Damper Virtual Coupling .....	39
4.10 Impedance Range .....	41
5.1 A Benchmark Haptic Display .....	43
5.2 Benchmark Impedance Display .....	44
5.3 Haptic Simulation with Impedance Display .....	46
5.4 Mechanical Analog of Spring-Damper Virtual Coupling .....	46
5.5 Benchmark Admittance Display .....	50
5.6 Haptic Simulation with Admittance Display .....	52
5.7 Mechanical Analog of Mass-Damper Virtual Coupling .....	52
6.1 Basic Impedance Display Implementation .....	60
6.2 Impedance Display with Force Compensation Implementation .....	62
6.3 Admittance Display Implementation .....	63
7.1 HBFD Hardware .....	73
7.2 Lumped-Mass Model of HBFD Flexibility .....	74
7.3 Basic Impedance Display Numerical Design .....	76
7.4 Admittance Display Numerical Design .....	77
7.5 Simple Haptic Simulation Based on the HBFD .....	78
7.6 Impedance Range for Impedance and Admittance Display .....	81
8.1 Excalibur Hardware .....	82
8.2 Basic Impedance Display Virtual Coupling Design .....	85
8.3 Impedance Display Force Regulator Design .....	86

8.4	Impedance Display with Force Compensation Virtual Coupling Design .....	87
8.5	Admittance Display Virtual Coupling Design .....	88
8.6	Impedance Range for Three Haptic Display Implementations .....	91
8.7	Impedance Range with Modified Admittance Display .....	94
9.1	Virtual and Real Biplane Models .....	95
9.2	The Virtual Building Block System .....	98
9.3	Matching Test Hydrofoil Boat Model .....	101
9.4	Mean Biplane Completion Time versus Iteration .....	105

## LIST OF TABLES

<i>Number</i>	<i>Page</i>
3.1 Electrical-Mechanical Analog Pairs .....	16
3.2 Connections in Electrical-Mechanical Analog Pairs .....	17
3.3 Two-Port Representations .....	18
3.4 Mappings Between Two-Port Representations .....	19
3.5 Correspondence of Parameters in Electrical-Mechanical Analogs .....	20
3.6 Single Element Electrical and Mechanical Dual Pairs .....	21
3.7 Correspondence of Parameters for Dual Networks .....	22
3.8 Construction of Mechanical Dual Using Electrical Analogs .....	24
5.1 Correspondence in Impedance/Admittance Display Duality .....	56
6.1 Virtual Coupling Implementations .....	66
7.1 Theoretical Versus Experimental Gains for the HBFD .....	80
8.1 Theoretical Versus Experimental Gains for Excalibur .....	90
9.1 LEGO™ Model Completion Times in Seconds .....	103
9.2 <i>p</i> -levels for VBB Study .....	104
9.3 Pair-Wise Comparisons Using Tukey HSD .....	107

## ACKNOWLEDGEMENTS

My love and appreciation go to my confidante, companion, and expert proof reader, Paula Adams. After reading countless drafts of this dissertation and the technical papers it spawned, she could have probably defended the thesis herself.

Special thanks goes to my advisor, Blake Hannaford, for providing the right combination of guidance and elbow room to create an ideal research environment.

Dan Klowden, University of Washington undergraduate in Computer Science and Engineering, was instrumental in the Virtual Building Block (VBB) training study. He made modifications and enhancements to the VBB software which were necessary to conduct the tests described in Chapter 9. Dan carried a large portion of the workload in the actual administration of the experiments and was a great brain-storming partner.

Thanks also to Manuel Moreyra of Hapitc Technologies Inc. for his assistance in developing the analytical model of the Excalibur force display. It was Manuel who actually built both the HBFD and Excalibur hardware, making the experimental studies possible.

I am grateful to the folks at Boeing Phantom Works, most notably Bill McNeely and Jim Troy, for loaning me the force sensor used in the Excalibur experimental studies.

Finally, my appreciation goes to the U.S. Air Force for sending me to the University of Washington to pursue a doctorate.

## DEDICATION

To Connor William Adams and his soon to arrive sibling. May God bless you as He has blessed me with you.

## Chapter 1

# An Introduction to Haptics - A New Paradigm for Human-Computer Interaction

*Some classes of animals have all the senses, some only certain of them, others only one, the most indispensable, touch. Aristotle, 350 B.C.*

### 1.1 Touch and the “Sixth Sense”

Aristotle described five basic human faculties: sight, hearing, touch, smell, and taste [1]. Of these, only the first two have been widely exploited in human-computer interaction. The video monitor and, to a lesser extent, the audio system are the primary conduits of information. They allow us to see and hear a rendering of the digital data inside a computer. This audio-visual representation is extremely limited in contrast to a human's rich, multi-sensory perception of reality. Current computers are especially poor in conveying information on physical properties such as inertia, friction, compliance, temperature, and roughness. These qualities are best communicated by a relatively unexplored means of human-computer dialogue, haptic interaction. The word haptic refers to something “of or relating to the sense of touch” [2].

The sense of touch involves many different types of receptors in the skin which detect varying levels of pressure, vibration, temperature, and pain. Closely related to touch is a lesser known “sixth sense” which Aristotle neglected. Kinesthesia is the sense of awareness which permits us to detect the position and motion of our body in space, as well as its internal tensions. This information is derived primarily from receptors in muscles, joints, and tendons. When a human contacts and manipulates the environment, the sense of touch and kinesthesia are heavily intertwined. If we squeeze an orange, we detect its firmness through the pressure sensors in our fingers as well as the movement of our joints and tension in our muscles. Light forces and vibrations are detected for the most



part through touch. Large forces and the resulting movements are sensed primarily through kinesthesia. In this work, we will use the term haptic to describe both touch and kinesthesia.

## 1.2 Haptic Displays

A device configured to provide haptic information to a human is called a *haptic display*. Just as a video display allows the user to see a computer generated scene, a haptic display permits the user to “feel” it. The size, shape, and function of these devices are as varied as the human receptors which they target. Tactile displays, a subclass of haptic displays, target the vibration and pressure sensing elements of touch. Other haptic displays generate larger motions and forces which are sensed through both touch and kinesthesia. These are often called hand controllers or manipulanda and can resemble joysticks or robotic manipulators. The present study focuses on this second class of haptic displays.

### 1.2.1 The Early Years

It was early work in telerobotics, motivated by the need to remotely manipulate hazardous nuclear materials, which spawned the first manipulanda. In the 1950's, researchers at Argonne National Laboratory developed a two arm master manipulator, with five degrees of freedom in each arm, which provided force-feedback cues to a human operator. This manipulandum controlled a kinematically similar slave robot which carried out the master's commands within a hazardous environment [3], [4]. Another pioneering system, named Handyman, was built for the AEC-USAF Aircraft Nuclear Propulsion Program in 1958 [5]. The Handyman manipulandum was the first force-feedback exoskeletal master. The operator literally strapped a robotic device to each arm to remotely control an anthropomorphically designed two-arm slave robot. With the advent of the space program, the focal point for teleoperation shifted to NASA and the Jet Propulsion Laboratory. A number of master devices resulted, including an anthropomorphic exoskeletal system driven by harmonic drive actuators [6] and a six degree-of-freedom hand controller [7].

As the power of computers expanded in the 80's, so too did the need for improved human-computer interaction. Virtual reality opened the possibility of moving beyond the drab 2-D world of conventional desktop systems to an immersive, multi-sensory environment. Applications of haptic display went beyond teleoperation into the more general and expansive field of data exploration and manipulation. One of the first examples of haptic interaction with a virtual environment was project GROPE at the University of North Carolina [8], [9]. The project explored the use of force feedback for scientific visualization. Using a seven degree-of-freedom manipulandum, the operator performed a molecular docking task. The user experienced attractive and repulsive forces while attempting to manipulate a virtual molecule into a stable configuration with other molecules in a computer simulation. The field of haptics moved further into virtual reality with Margaret Minsky's Sandpaper system [10]. A two degree-of-freedom force feedback joystick communicated with a computer generated virtual environment to simulate haptic primitives such as masses, springs, dampers, and textures.

Interest in haptic systems was not limited to the United States. At the University of Tsukuba in Japan, Hiroo Iwata developed a nine degree-of-freedom device which applied forces to the operator's hand to simulate grasping of complex virtual objects [11]. In one of the earliest examples of haptic display for virtual prototyping, the user was able to hold a virtual camera, sensing its geometry and mass properties. Unfortunately, the application suffered from an acute lack of computing power, permitting less than four frames per second. A dramatic increase in processing speed would be required to achieve a high degree of fidelity in the "feel" of complex virtual objects.

### **1.2.2 Into the 90's and Beyond**

The field exploded in the 1990's as researchers and corporations discovered more and more uses for force feedback technology. The availability of cheap computing power made highly sophisticated real-time simulations possible. One important catalyst in this frenzy of research was the development and commercialization of the PHANToM family

of haptic displays [12]. Thomas Massie and Kenneth Salisbury built the first version of this three degree-of-freedom fingertip device at MIT's Artificial Intelligence Laboratory in 1993. Since its incorporation later that year, SensAble Technologies has shipped hundreds of PHANToM's to customers around the world. The availability of an out-of-the-box solution allowed researchers to focus their efforts on the development of advanced applications and the study of human factors issues in haptic interaction. A line drawing of the original PHANToM is shown in Fig. 1.1.

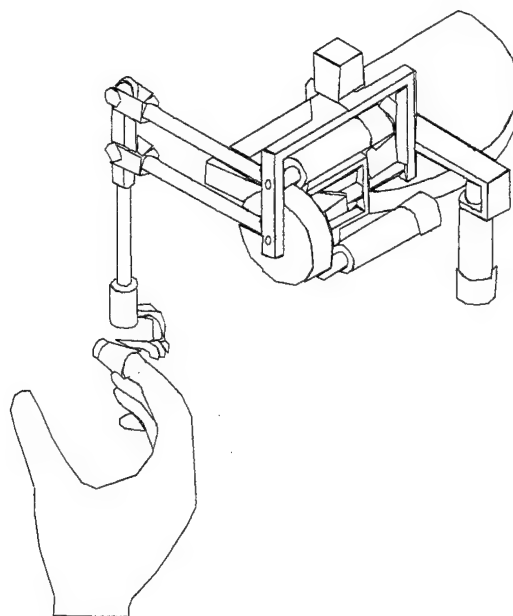


Fig. 1.1. The PHANToM Haptic Display

The commercial success of the PHANToM did not curtail the development of new haptic devices. Their numbers are, in fact, too great to cite each in detail. Some representative examples and applications follow. At the University of Washington, a small, portable, desk-top system was developed for interaction with three degree-of-freedom environments, the Pen-Based Force Display (PBFD) [13]. This compact device, shown in Fig. 1.2, demonstrated the potentiality of the integration of haptic displays into portable electronic devices such as lap-top computers. The PBFD was used in a ground-breaking demonstration of force feedback over the Internet. Two geographically separated players participated in a game of "Force Feedback Multi-player Squash" [14]. One, located in

Seattle, WA used the PBFD. Another, situated at the Universita di Padova, Italy used a different haptic display, the PantoMouse. An adaptive scheme was used to ensure the dynamics of the simulation were compatible with the network-induced time delay.

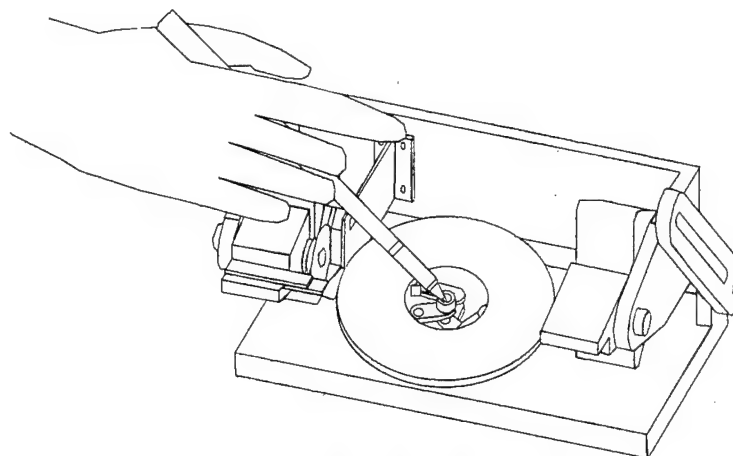


Fig. 1.2. The Pen-Based Force Display

Another compact master device, conceived at Carnegie Mellon University for teleoperation, departs from more conventional designs by suspending the handle using magnetic levitation [15]. Subsequent versions of the device have been used at the University of British Columbia as haptic interfaces to virtual environments [16], [17]. The six degree-of-freedom design provides a virtually frictionless mechanism at the expense of being limited to a very small workspace. An improved magnetic levitation device, the PowerMouse, is under commercial development for the research market.

While small, desk-top manipulanda, such as those mentioned above, are useful for many applications, others demand a much larger workspace and higher force output. The University of Washington High-Bandwidth Force Display (HBFD), pictured in Fig. 1.3, is a two degree-of-freedom hand controller built in response to this requirement [18]. Industry demand for this technology led to the creation of a spin-off company, Haptic Technologies Inc. (HTI), by HBFD creator Manuel Moreyra. HTI went on to develop a three degree-of-freedom device, Excalibur, which provides a large workspace and high forces through direct drive motors and a novel steel cable transmission. A line drawing of

Excalibur is shown in Fig. 1.4. A gimbal system is under development to extend Excalibur to six actuated degrees-of-freedom.

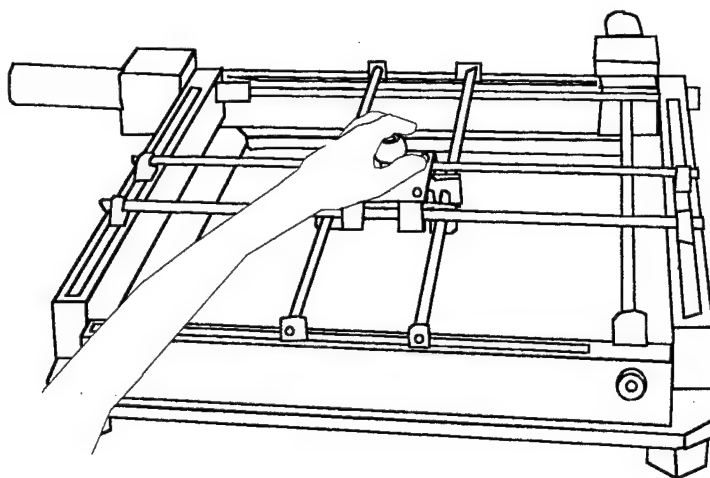


Fig. 1.3. The High-Bandwidth Force Display

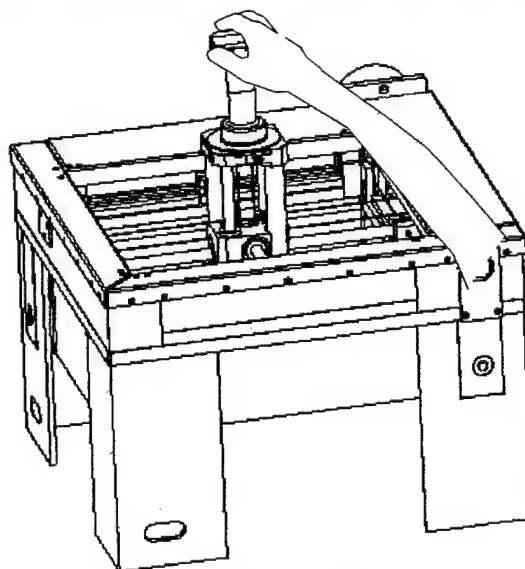


Fig. 1.4. Excalibur

In contrast to manipulanda which provide forces only to the user's hand or fingers, exoskeletal systems may generate sensations affecting an entire limb. One such device was developed at the Scuola Superiore Sant' Anna in Pisa, Italy [19]. A seven degree-of-freedom exoskeletal arm, worn by a human operator, conveys forces generated on a virtual arm in a computer simulation. The Sarcos Dexterous Arm Master is another

exoskeleton-like system with contact points at the forearm and upper arm of the user. It uses hydraulic actuation to provide high force output in ten degrees-of-freedom. The Sarcos device is being used to provide force feedback in CAD applications [20].

The early history of force feedback technology was dominated by research applications. This changed in 1996 when CH Products released the first consumer level haptic display, the Force FX joystick. As a pioneer, this product was plagued by poor marketing and low acceptance within the computer game programming community. Microsoft entered the picture in 1997 with the Sidewinder Force Feedback Pro joystick. By working with the Immersion Corporation to integrate force feedback technology into the industry standard DirectX API, they gained rapid acceptance among programmers. The improved design of this device, along with aggressive marketing and an existing distributor base, brought force feedback to the forefront of the computer game market. Logitech joined the mix in 1998 with the WingMan Force joystick, a cable-driven device which raised the bar for fidelity in consumer haptic systems. The consumer market penetration of haptics continues with the arrival of numerous force feedback steering wheels for use with racing simulators. The ultimate acceptance of haptic technology may come with the integration of force feedback into the ubiquitous desk-top mouse. This is the hope of Immersion and their partner Logitech in the unveiling of the FEELit Mouse.

The advance of haptic technology is not likely to slow any time soon. The rapid evolution of the field leads one to speculate on where it will lead. What is the supreme vision for haptics? One answer is that the ultimate haptic system is one in which the user cannot distinguish between the virtual and the real. The subject might be made to experience a swim in the ocean or to climb a rocky cliff. Reflecting once again on the complexity of the human senses of touch and kinesthesia, the field still has a very long way to go. Fortunately, between the current state-of-the-art and that ultimate vision, there are many exciting applications!

### 1.3 Keeping Things Under Control

The field of haptics is highly interdisciplinary. To successfully build a haptic display, a knowledge of mechanical design, kinematics, and dynamics is required. Electrical engineering expertise is needed to build power electronics to drive the motors, circuitry to read the sensors, and analog-to-digital/digital-to-analog conversions to interface the device to a computer. Computer science knowledge is used in developing device drivers and in programming the actual application. To design the application, specialized expertise may be needed. If it is a surgery simulator, medical doctors must be consulted. If it is a CAD program, the software end-users should be integrated into the design process. Human factors is also an important component. How should a device target the human senses to best create a compelling sense of presence? What level of fidelity is required? What are the risks of trauma or injury to the human operator?

One discipline which has lagged behind the rapid growth of haptics is control engineering, the study of system stability and the design of control laws for stability and performance. The control engineer is concerned with ensuring the haptic system, including the haptic display, the application software, and the human operator, remains stable while creating a compelling sense of haptic presence. In contrast to telerobotic systems, where control engineering has always played an integral role, controls has been largely forgotten in the application of haptic displays as human-computer interface devices. This is evidenced by the propensity for haptic simulations, both demos and advanced applications, to encounter instabilities. One example is the Force FX joystick, which can become quite unstable when used with the out-of-the-box demo program. An LED 'dead-man' switch turns force feedback off when the stick is released, but when the user holds the stick with a light grip, the joystick flails back and forth uncontrollably. Many applications of PHANTOM devices are known to experience oscillations at points in the workspace. While often discounted by computer scientists as "noise" or "vibrations", these oscillations are actually the consequence of an unstable control law design.

## Chapter 2

### State-of-the-Art in Control of Haptic Interfaces

The existence of physical interaction between human and machine distinguishes haptic displays from other robotic manipulators. When the operator interacts with a manipulandum, the dynamical properties of the device are altered. This variability in system behavior presents a significant challenge for control law design. The control engineer cannot simply apply textbook techniques, such as root locus or Bode design, and hope to come up with a viable result. Solutions tailored to the haptic interface problem are required.

#### 2.1 The Foundation, Control for Telerobotics

Telerobotics provided the impetus for early control theory advances in haptic systems. An important development was the adaptation of two-port network theory to the analysis of teleoperators. In the late 1980's at MIT, Thomas Sheridan and his staff used two-port models and passivity criteria to design control gains for a master-slave manipulator [21]. By forcing the two-port impedance matrix of the teleoperator system to be positive real, they guaranteed stability for any passive slave environment and any passive human impedance.

At the Jet Propulsion Laboratory, Blake Hannaford characterized several common teleoperator architectures in terms of the two-port hybrid matrix [22]. He showed the hybrid matrix provides convenient interpretations of performance in bilateral teleoperation. The effects of control law changes on individual hybrid matrix parameters provided useful intuition into stability and performance tradeoffs [23].

Passivity and two-port methods were used extensively by Robert Anderson for bilateral control with time delay [24]. He developed stability criteria based on the two-port scattering matrix and proved stability for time delayed teleoperation by forcing master-



slave communication to act as a lossless transmission line [25]. This work culminated in the development of a modular robot control architecture, SMART, which guaranteed overall system stability by forcing individual modules to satisfy passivity criteria [26].

J. Edward Colgate recognized that teleoperator passivity, as a condition for stability robustness, could be overly conservative. He leveraged advances in the field of robust control to provide a necessary and sufficient condition for the stability of the coupled system based on the structured singular value of the scattering matrix [27]. In a break with previous researchers, he acknowledged the mixed continuous-discrete nature of the stability problem and showed passivity techniques could be applied to such systems [28].

An underlying assumption of the aforementioned stability results based on passivity theory is that the human operator behaves as a passive impedance. Considering the existence of neural feedback within the neuromuscular system, it would seem as though some level of activity in the resulting impedance would be inevitable. In the mid-1980's at MIT, Neville Hogan set out to characterize the neuromuscular mechanics of the human arm. He discovered that while the neuromuscular system is internally complex, it exhibits externally simple, spring-like behavior [29]. The significance of this result is the human arm is guaranteed stable when coupled to any external system which is itself passive. Furthermore, Hogan observed that while humans can modulate the impedance of their limbs (by tightening or relaxing opposing muscles), it requires up to 1.5 seconds to consciously initiate an impedance change [30]. Human arm impedance can therefore be considered as both passive and constant for the purposes of studying system stability.

## **2.2 Modern Haptics**

One of the first studies of stability issues particular to haptic interaction with virtual environments took place at the MIT Media Laboratory [10] under the direction of Margaret Minsky. They took a relatively unsophisticated approach to the problem. Assuming second-order dynamics for the manipulandum and human arm, modeling digital

delay as a second-order Taylor series expansion, and using a constant spring for the virtual environment, they evaluated closed loop stability by calculating the roots of the resulting characteristic equation. Overall system stability was described as a tradeoff between three primary factors: sampling period, device damping, and virtual stiffness.

Colgate and his group at Northwestern University sought a more rigorous stability result for manipulanda under sampled-data control. They adopted the concept of a passive man-machine interface as a criteria for stability robustness [31]. Their approach, motivated by previous work in telerobotics, eliminated the requirement for a human impedance model and included an improved representation of digital delay effects. For a simple haptic device, characterized by a mass and a viscous damping coefficient, they showed damping to be the only device property to influence stability in a haptic simulation [32]. For the emulation of virtual walls, a sufficient condition was found relating device damping to sampling period, virtual stiffness, and virtual damping.

As computers grew faster and cheaper, researchers built haptic feedback into increasingly complex virtual reality simulations. A problem soon became apparent. The stability of haptic feedback was dependent on the intricate interactions taking place in the virtual world. The impedance properties and geometry of each object in the virtual environment had to be selected so that no between-object interaction could possibly generate an instability. The number and complexity of objects in a compelling simulation, such as a surgery trainer or a CAD system, made this approach intractable. In 1995, Colgate, Stanley, and Brown proposed the introduction of a "virtual coupling" between the haptic display and the virtual environment to eliminate this problem [33]. Researchers had previously observed, for a given haptic device with a given sampling rate, there existed a maximum stiffness (or, more correctly, impedance) which could be emulated by a virtual wall while maintaining stability. In complex virtual environments, this maximum stiffness was sometimes exceeded due to mechanical advantage between virtual objects. The virtual coupling, an artificial spring-damper connecting the haptic display to the

simulation, effectively limited the maximum control impedance to that of the coupling itself. Theoretically, introduction of the virtual coupling made stable haptic simulation of infinitely complex virtual worlds possible. J. Michael Brown explored conditions under which the virtual coupling parameters guaranteed a passive interface to the human operator. He developed design criteria for an arbitrary discrete-time passive environment [34] and for a non-passive virtual mass simulation [35].

Zilles and Salisbury from the MIT Artificial Intelligence Laboratory presented their own technique for stable haptic rendering of complex virtual objects at the 1995 IROS conference [36]. Their approach was to servo the haptic display to an artificial "god-object" which conformed to the virtual environment. MIT's god-object was actually a special case of Northwestern's virtual coupling, for point contact with a static virtual environment. The two works were complimentary in the sense that Northwestern provided a strong theoretical basis while MIT demonstrated a relatively sophisticated application of the approach. Two-years later, Stanford University presented an extension to the god-object technique, the "virtual proxy" [37]. The group, led by Oussama Khatib, coupled a PHANTOM device to a three degree-of-freedom constraint based simulation using their special version of the virtual coupling. They succeeded in rendering static models containing more than 24,000 polygons.

The virtual coupling represented a critical departure from previous approaches to haptic rendering. Once a virtual coupling was designed for a particular haptic display, it could be coupled to any simulation which was discrete-time passive (or nearly passive), and stability would be ensured. Previously, a virtual environment had to be tuned and tested for a particular haptic display, with no stability guarantee other than that provided through extensive experimentation. If a new haptic display was introduced, the simulation would have to be re-tuned and re-tested all over again. While important, the results of Colgate et. al. [33], [34] were limited in three important ways. The haptic device, represented by a simple mass and damping coefficient, was assumed rigid with collocated sensors and

actuators. They considered only one class of haptic displays, “impedance displays” which measure motion and display force. A second class, “admittance displays” which measure force and display motion, was not considered. These two classes of haptic displays were first recognized by Yoshikawa [38]. Finally, Northwestern University’s virtual coupling results assumed a particular class of virtual environment, those which accept forces and return the resulting motions. This type of simulation is often referred to as constraint-based or as an “admittance environment”. A more common implementation is one which accepts positions and velocities and returns forces. This class of virtual environment is labeled penalty-based or “impedance environment”.

### **2.3 New Contributions**

This dissertation extends the concept of a virtual coupling to admittance displays and treats the problem of stable haptic interaction in a more general framework which encompasses any combination of haptic display and virtual environment causality. Chapter 4 describes this new two-port framework for haptic interaction. Its central element is the use of Llewelyn’s criteria for “absolute stability” as a tool for the design and evaluation of virtual coupling networks. In Chapter 5, a benchmark example illustrates fundamental stability and performance tradeoffs in haptic display and brings to light an important duality between the impedance and admittance models of haptic interaction. Chapter 6 presents a more general formulation of the absolute stability criteria which can be applied to devices with structural flexibility and sensor dynamics. Chapters 7 and 8 submit numerical applications of virtual coupling design for absolute stability on two different haptic displays. Both impedance and admittance type haptic display implementations as well as impedance and admittance causality virtual environments are demonstrated. These designs, for the HBFD and Excalibur, are validated experimentally on actual hardware.

## Chapter 3

### Review of Network Theory

The study of stability and control of haptic interfaces to virtual and remote environments is heavily rooted in network theory. To the modern control engineer, the relationship between the control of haptic displays and this antiquated discipline may seem curious. While many of the original breakthroughs in control theory were offshoots of the study of linear circuit networks, the field has since progressed to more exciting frontiers such as  $H_\infty$  optimization and fuzzy logic. What is the reason for this reversion to the time-honored techniques of the past? The answer is that network representations are a natural way of describing the physical interaction between human and machine which is critical in the study of haptic systems.

#### 3.1 Network Representations

Linear network theory originally evolved in pursuit of improved analysis and design techniques for analog circuits. Central to the characterization of these electrical systems is the concept of “ports”, terminal pairs at which a circuit can be accessed. A voltage,  $e$ , and a current,  $i$ , exist at each port. The network representation of a circuit describes the constraints enforced by the circuit between these voltages and currents. A network with  $n$  ports,  $\mathcal{N}_n$ , is completely described by the totality of its admissible signal pairs [39].

$$\left\{ \left[ e_k, i_k \right]_{t_0}^{t_f}, k = 1, 2, \dots, n \right\} = \mathcal{N}_n \quad (3.1)$$

This set theoretic representation is the most compact characterization of a network. Control engineers commonly use transfer functions to represent linear system behavior. When describing a system in transfer function form, a set of input and output signals are identified. No such differentiation is made in network theory. A network is characterized by the *relationship* between voltages and currents. Consider a linear time-invariant one-port network,  $\mathcal{N}$ , shown in Fig. 3.1.

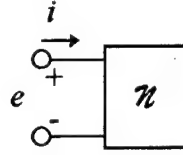


Fig. 3.1. A One-Port Network,  $\mathcal{N}$

This network can be characterized by the transfer function from current to voltage,  $z(s)$ ,

$$\left\{ \left[ e, i \right]_{t_0}^{t_f} : e(s) = z(s)i(s) \right\} = \mathcal{N} \quad (3.2)$$

or by the transfer function from voltage to current,  $y(s)$ .

$$\left\{ \left[ e, i \right]_{t_0}^{t_f} : i(s) = y(s)e(s) \right\} = \mathcal{N} \quad (3.3)$$

The former is called an impedance function, the latter an admittance function. (3.2) and (3.3) are equivalent, both characterize the network equally well.

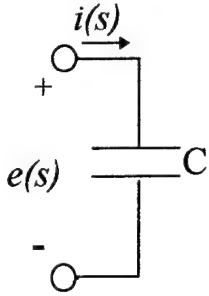
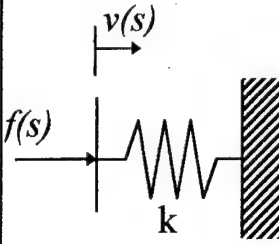
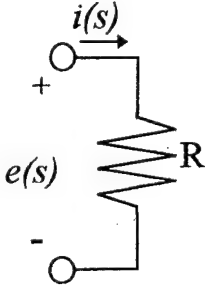
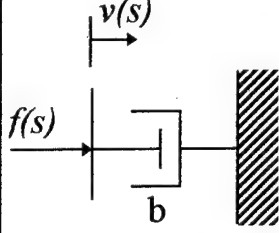
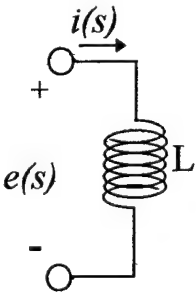
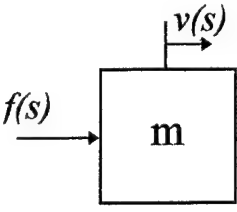
Human-to-device interaction in haptic display is also best characterized in network terms. When grasping a manipulandum, the human operator is not sensing force and commanding velocity, nor is the user sensing velocity and applying a force. When operator-device contact takes place, a new velocity-force *relationship* is enforced. Just as electrical circuit behavior is modified when a resistor is added to a network, so too are the basic dynamical properties of the haptic display changed when the device is grasped by the human operator. The point of human-to-device contact is a point of access, a port, to a mechanical network.

### 3.2 Analog Systems

Network theory is not restricted to electrical circuits. The same concepts may be brought to bear for many classes of engineering systems which undergo energetic interactions between elements [40]. The application of network theory to haptic displays takes advantage of analogous behavior between electrical and mechanical systems. Electrical-mechanical analog networks enforce equivalent relationships between *effort* and *flow*. For the mechanical system, forces replace voltages in representing effort, while velocities

replace currents in describing flow. Table 3.1 shows electrical-mechanical analog pairs for some basic linear network elements.

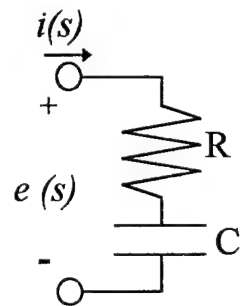
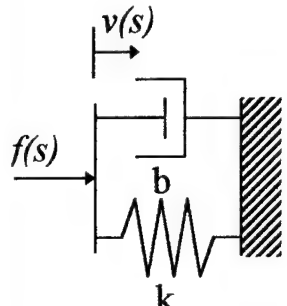
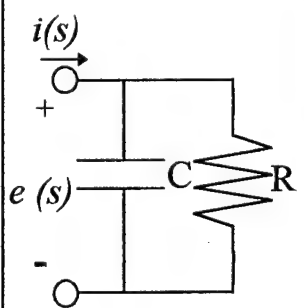
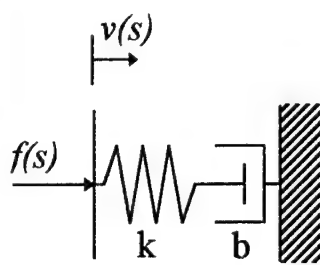
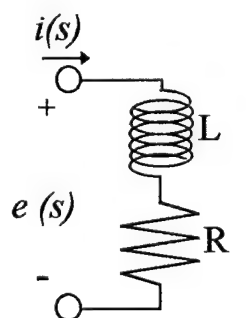
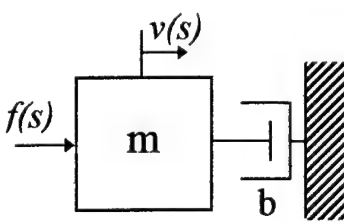
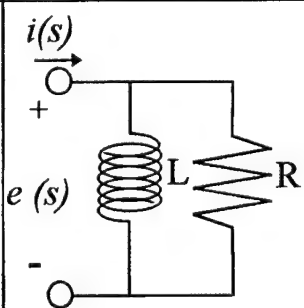
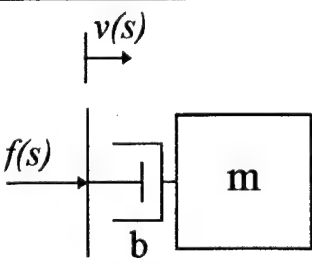
Table 3.1. Electrical-Mechanical Analog Pairs

electrical system		mechanical system	
capacitor $e(s) = \frac{1}{Cs} i(s)$			spring $f(s) = \frac{k}{s} v(s)$
resistor $e(s) = R i(s)$			damper $f(s) = b v(s)$
inductor $e(s) = Ls i(s)$			mass $f(s) = ms v(s)$

More complex networks comprised of these basic electrical elements can be represented as analogous mechanical systems. When two electrical elements are connected in series, their combined impedance is additive,  $z_{total}(s) = z_1(s) + z_2(s)$ . In a mechanical system, an additive impedance is achieved by connecting two elements in parallel. Conversely, electrical elements connected in parallel have additive admittance,  $y_{total}(s) = y_1(s) + y_2(s)$ . A combined additive admittance in mechanical systems is achieved by connecting elements

in series. Examples of series and parallel electrical one-ports and their mechanical analogs are shown in Table 3.2.

Table 3.2. Connections in Electrical-Mechanical Analog Pairs

electrical system $e(s) = z(s)i(s)$		mechanical analog $f(s) = z(s)v(s)$	
<p>series</p> $z(s) = R + \frac{1}{Cs}$			<p>parallel</p> $z(s) = b + \frac{k}{s}$
<p>parallel</p> $y(s) = \frac{1}{R} + Cs$ $z(s) = \frac{1/C}{s + 1/RC}$			<p>series</p> $y(s) = \frac{1}{b} + \frac{s}{k}$ $z(s) = \frac{k}{s + k/b}$
<p>series</p> $z(s) = Ls + R$			<p>parallel</p> $z(s) = ms + b$
<p>parallel</p> $y(s) = \frac{1}{Ls} + \frac{1}{R}$ $z(s) = \frac{Rs}{s + R/L}$			<p>series</p> $y(s) = \frac{1}{ms} + \frac{1}{b}$ $z(s) = \frac{bs}{s + b/m}$



### 3.3 Two-Port Representations

Networks with two pairs of accessible terminals, or two-ports, are especially useful in characterizing the exchange of energy between a human operator and a remote or virtual environment. Electrical two-port networks enforce a relationship between the currents and voltages at the accessible ports:  $i_1$ ,  $i_2$ ,  $e_1$ , and  $e_2$ . Mechanical two-ports are represented by the constraints they impose between velocities and forces:  $v_1$ ,  $-v_2$ ,  $f_1$ , and  $f_2$ . The negative sign on  $v_2$  is necessary to maintain consistency in the notion of flow between electrical and mechanical systems. The six possible two-by-two transfer function representations of a two-port are shown in Table 3.3.

Table 3.3. Two-Port Representations

impedance matrix $Z$	$\begin{bmatrix} f_1 \\ f_2 \end{bmatrix} = \begin{bmatrix} z_{11} & z_{12} \\ z_{21} & z_{22} \end{bmatrix} \begin{bmatrix} v_1 \\ -v_2 \end{bmatrix}$	admittance matrix $Y$	$\begin{bmatrix} v_1 \\ -v_2 \end{bmatrix} = \begin{bmatrix} y_{11} & y_{12} \\ y_{21} & y_{22} \end{bmatrix} \begin{bmatrix} f_1 \\ f_2 \end{bmatrix}$
hybrid matrix $H$	$\begin{bmatrix} f_1 \\ -v_2 \end{bmatrix} = \begin{bmatrix} h_{11} & h_{12} \\ h_{21} & h_{22} \end{bmatrix} \begin{bmatrix} v_1 \\ f_2 \end{bmatrix}$	alternate hybrid matrix $G$	$\begin{bmatrix} v_1 \\ f_2 \end{bmatrix} = \begin{bmatrix} g_{11} & g_{12} \\ g_{21} & g_{22} \end{bmatrix} \begin{bmatrix} f_1 \\ -v_2 \end{bmatrix}$
transmission matrix $ABCD$	$\begin{bmatrix} f_1 \\ v_1 \end{bmatrix} = \begin{bmatrix} A & B \\ C & D \end{bmatrix} \begin{bmatrix} f_2 \\ -v_2 \end{bmatrix}$	inverse transmission matrix $ABCD$	$\begin{bmatrix} f_2 \\ -v_2 \end{bmatrix} = \begin{bmatrix} \mathcal{A} & \mathcal{B} \\ \mathcal{C} & \mathcal{D} \end{bmatrix} \begin{bmatrix} f_1 \\ v_1 \end{bmatrix}$

For a particular network, one or more of these forms may not exist. For example, if the impedance matrix is singular, the admittance matrix, its inverse, does not exist. Outside of such cases, each of the six matrices can be derived from any of the others. The mapping from any two-port form to any alternate form is given in Table 3.4.

Table 3.4. Mappings Between Two-Port Representations

TO FROM	Z	Y	H	G	ABCD	$\overline{ABCD}$
Z	$\begin{matrix} z_{11} & z_{12} \\ z_{21} & z_{22} \end{matrix}$	$\begin{matrix} \frac{z_{22}}{\Delta_z} & -\frac{z_{12}}{\Delta_z} \\ -\frac{z_{21}}{\Delta_z} & \frac{z_{11}}{\Delta_z} \end{matrix}$	$\begin{matrix} \frac{\Delta_z}{z_{22}} & \frac{z_{12}}{z_{22}} \\ -\frac{z_{21}}{z_{22}} & \frac{1}{z_{22}} \end{matrix}$	$\begin{matrix} \frac{1}{z_{11}} & -\frac{z_{12}}{z_{11}} \\ \frac{z_{21}}{z_{11}} & \frac{\Delta_z}{z_{11}} \end{matrix}$	$\begin{matrix} \frac{z_{11}}{z_{21}} & \frac{\Delta_z}{z_{21}} \\ \frac{1}{z_{21}} & \frac{z_{22}}{z_{21}} \end{matrix}$	$\begin{matrix} \frac{z_{22}}{z_{12}} & -\frac{\Delta_z}{z_{12}} \\ -\frac{1}{z_{12}} & \frac{z_{11}}{z_{12}} \end{matrix}$
Y	$\begin{matrix} \frac{y_{22}}{\Delta_y} & -\frac{y_{12}}{\Delta_y} \\ -\frac{y_{21}}{\Delta_y} & \frac{y_{11}}{\Delta_y} \end{matrix}$	$\begin{matrix} y_{11} & y_{12} \\ y_{21} & y_{22} \end{matrix}$	$\begin{matrix} \frac{1}{y_{11}} & -\frac{y_{12}}{y_{11}} \\ \frac{y_{21}}{y_{11}} & \frac{\Delta_y}{y_{11}} \end{matrix}$	$\begin{matrix} \frac{\Delta_y}{y_{22}} & \frac{y_{12}}{y_{22}} \\ -\frac{y_{21}}{y_{22}} & \frac{1}{y_{22}} \end{matrix}$	$\begin{matrix} -\frac{y_{22}}{y_{21}} & -\frac{1}{y_{21}} \\ \frac{y_{21}}{y_{21}} & -\frac{y_{11}}{y_{21}} \end{matrix}$	$\begin{matrix} -\frac{y_{11}}{y_{12}} & \frac{1}{y_{12}} \\ \frac{y_{12}}{y_{12}} & -\frac{y_{22}}{y_{12}} \end{matrix}$
H	$\begin{matrix} \frac{\Delta_h}{h_{22}} & \frac{h_{12}}{h_{22}} \\ -\frac{h_{21}}{h_{22}} & \frac{1}{h_{22}} \end{matrix}$	$\begin{matrix} \frac{1}{h_{11}} & -\frac{h_{12}}{h_{11}} \\ \frac{h_{21}}{h_{11}} & \frac{\Delta_h}{h_{11}} \end{matrix}$	$\begin{matrix} h_{11} & h_{12} \\ h_{21} & h_{22} \end{matrix}$	$\begin{matrix} \frac{h_{22}}{\Delta_h} & -\frac{h_{12}}{\Delta_h} \\ -\frac{h_{21}}{\Delta_h} & \frac{h_{11}}{\Delta_h} \end{matrix}$	$\begin{matrix} -\frac{\Delta_h}{h_{21}} & -\frac{h_{11}}{h_{21}} \\ \frac{h_{21}}{h_{21}} & -\frac{1}{h_{21}} \end{matrix}$	$\begin{matrix} \frac{1}{h_{12}} & -\frac{h_{11}}{h_{12}} \\ \frac{h_{12}}{h_{12}} & \frac{\Delta_h}{h_{12}} \end{matrix}$
G	$\begin{matrix} \frac{1}{g_{11}} & -\frac{g_{12}}{g_{11}} \\ \frac{g_{21}}{g_{11}} & \frac{\Delta_g}{g_{11}} \end{matrix}$	$\begin{matrix} \frac{\Delta_g}{g_{22}} & \frac{g_{12}}{g_{22}} \\ -\frac{g_{21}}{g_{22}} & \frac{1}{g_{22}} \end{matrix}$	$\begin{matrix} \frac{g_{22}}{\Delta_g} & -\frac{g_{12}}{\Delta_g} \\ -\frac{g_{21}}{\Delta_g} & \frac{g_{11}}{\Delta_g} \end{matrix}$	$\begin{matrix} g_{11} & g_{12} \\ g_{21} & g_{22} \end{matrix}$	$\begin{matrix} \frac{1}{g_{21}} & \frac{g_{22}}{g_{21}} \\ \frac{g_{11}}{g_{21}} & \frac{\Delta_g}{g_{21}} \end{matrix}$	$\begin{matrix} -\frac{\Delta_g}{g_{12}} & \frac{g_{22}}{g_{12}} \\ \frac{g_{11}}{g_{12}} & -\frac{1}{g_{12}} \end{matrix}$
ABCD	$\begin{matrix} \frac{A}{C} & \frac{\Delta_A}{C} \\ \frac{1}{C} & \frac{D}{C} \end{matrix}$	$\begin{matrix} \frac{D}{B} & -\frac{\Delta_A}{B} \\ -\frac{1}{B} & \frac{A}{B} \end{matrix}$	$\begin{matrix} \frac{B}{D} & \frac{\Delta_A}{D} \\ -\frac{1}{D} & \frac{C}{D} \end{matrix}$	$\begin{matrix} \frac{C}{A} & -\frac{\Delta_A}{A} \\ \frac{1}{A} & \frac{B}{A} \end{matrix}$	$\begin{matrix} A & B \\ C & D \end{matrix}$	$\begin{matrix} \frac{D}{\Delta_A} & -\frac{B}{\Delta_A} \\ -\frac{C}{\Delta_A} & \frac{A}{\Delta_A} \end{matrix}$
$\overline{ABCD}$	$\begin{matrix} \frac{D}{B} & -\frac{\Delta_A}{B} \\ -\frac{1}{B} & \frac{A}{B} \end{matrix}$	$\begin{matrix} \frac{A}{C} & \frac{\Delta_A}{C} \\ \frac{1}{C} & \frac{D}{C} \end{matrix}$	$\begin{matrix} \frac{C}{A} & -\frac{\Delta_A}{A} \\ \frac{1}{A} & \frac{B}{A} \end{matrix}$	$\begin{matrix} \frac{B}{D} & \frac{\Delta_A}{D} \\ -\frac{1}{D} & \frac{C}{D} \end{matrix}$	$\begin{matrix} \frac{D}{\Delta_A} & -\frac{B}{\Delta_A} \\ -\frac{C}{\Delta_A} & \frac{A}{\Delta_A} \end{matrix}$	$\begin{matrix} A & B \\ C & D \end{matrix}$
$\Delta_x = x_{11}x_{22} - x_{12}x_{21}$						

Using the previously developed relationships for electrical-mechanical analog systems, mechanical two-port analogs can be formed from electrical two-port networks. The correspondence of parameters is shown in Table 3.5.

Table 3.5. Correspondence of Parameters in Electrical-Mechanical Analogs

electrical system		mechanical system	
voltage	$e_1, e_2$	force	$f_1, f_2$
current	$i_1, i_2$	velocity	$v_1, -v_2$
inductance	$L$	mass	$m$
resistance	$R$	damping	$b$
reciprocal capacitance	$1/C$	stiffness	$k$

Fig. 3.2 shows an example of an electrical two-port network and its mechanical analog, a coupled two-mass system. By making the appropriate substitution of variables, the two systems have equivalent transfer function representations.

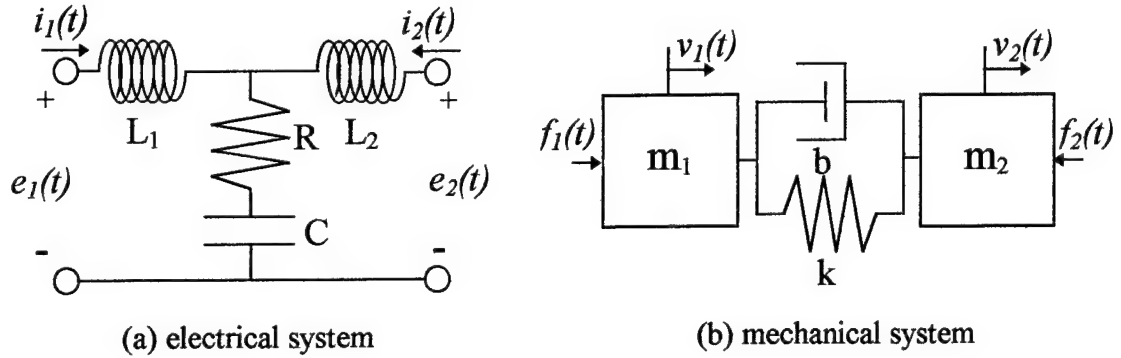


Fig. 3.2. Two-Port Analog Systems

### 3.4 Duality

A special relationship may exist between two networks which allows one network to be reconstructed from another using a simple substitution of variables.

*Definition 3.1:* Two networks,  $\mathcal{N}$  and  $\mathcal{N}'$ , are said to be *dual* if for every

admissible signal pair  $[e, i]_{t_0}^{t_f} \in \mathcal{N}$ , there exists an admissible signal pair

$[e', i']_{t_0}^{t_f} \in \mathcal{N}'$ , such that  $e'(t) = i(t)$  and  $i'(t) = e(t)$ . Likewise, for every

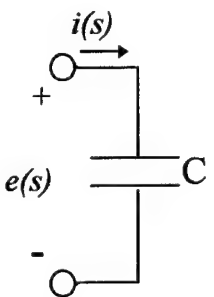
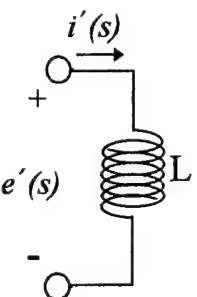
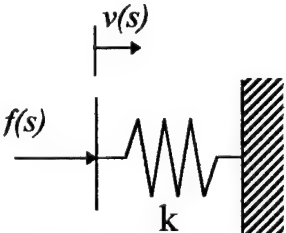
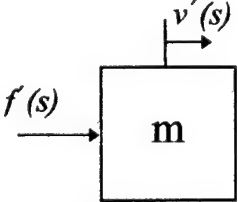
admissible signal pair  $[e', i']_{t_0}^{t_f} \in \mathcal{N}'$ , there exists an admissible signal pair

$[e, i]_{t_0}^{t_f} \in \mathcal{N}$ , such that  $e(t) = i'(t)$  and  $i(t) = e'(t)$  [39].

Frequently, the analysis of one network can be simplified by relating it to a better understood dual form. This concept of duality is useful in the analysis and design of haptic interfaces.

Dual networks can be found for both electrical and mechanical networks. In both cases, the relationship between efforts and flows in the original system is reversed in the dual network. Table 3.6 shows examples of single element one-ports and their duals.

Table 3.6. Single Element Electrical and Mechanical Dual Pairs

	dual pairs	
electrical	$i(s) = Cs e(s)$ 	$e'(s) = Ls i'(s)$ 
mechanical	$v(s) = s/k f(s)$ 	$f'(s) = ms v'(s)$ 

For more complex networks, dual forms are less obvious. Given a planar electrical circuit constructed of the one-port elements shown in Table 3.1, it is possible to systematically construct its dual using a graphical procedure. [41].

1. Draw the circuit from which the dual is to be formed.
2. Place a node symbol in the center of each mesh and a ground reference node outside of the network.
3. In a separate space, draw a duplicate set of nodes. These provide the basis for dual network construction.
4. For each network element, draw a line between two adjacent nodes such that the line crosses a mesh boundary only once.
5. For each line drawn on the original network, add the dual network element in the new network between the corresponding nodes.

Table 3.7 shows the correspondence of parameters and elements.

Table 3.7. Correspondence of Parameters for Dual Networks

current, $i_1$	voltage, $e_1'$
voltage, $e_1$	current, $i_1'$
current, $i_2$	voltage, $-e_2'$
voltage, $e_2$	current, $-i_2'$
inductance, L	capacitance, C
resistance, R	conductance, $1/R$

An example of this procedure is given in Fig. 3.3 for a four element two-port network. First, the two-port is terminated by inserting voltage sources at each port. These voltage sources become current sources in the dual network. Note that series elements in the original network become parallel (shunt) elements in the dual system. Likewise, parallel elements become series elements in the dual network. The impedance matrix of Fig. 3.3(a) is identical to the admittance matrix Fig. 3.3(f). Likewise the hybrid matrix of the original network is equal to the alternate hybrid matrix of its dual.

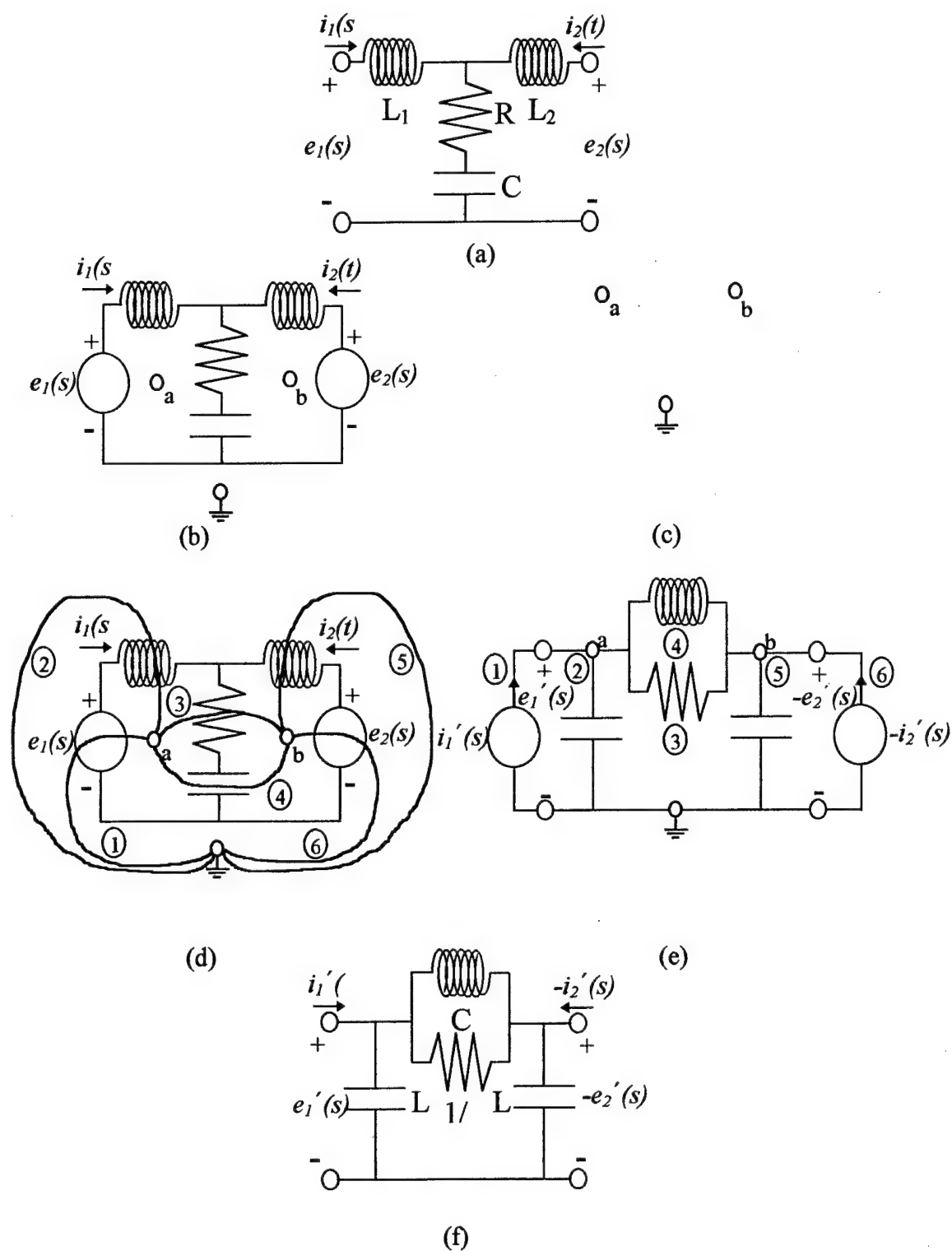
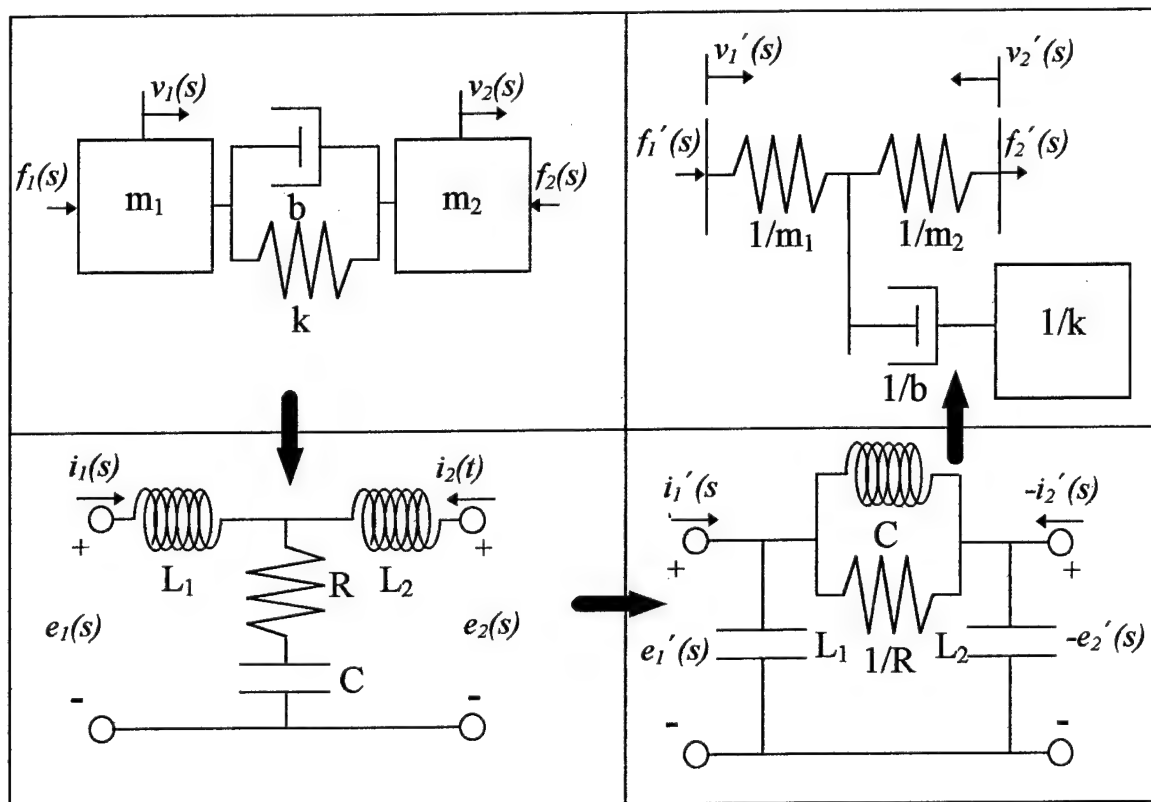


Fig. 3.3. Dual Network Construction

There is no systematic procedure for directly finding the dual of a mechanical network. It is possible though to find the electrical analog of a mechanical network, find its dual using the graphical approach outlined above, and then build the mechanical analog of the dual electrical network. The result is a mechanical network which is dual to the original mechanical system. This procedure is illustrated in Table 3.8 for the example of a coupled two mass network.

Table 3.8. Construction of Mechanical Dual Using Electrical Analogs



### 3.5 Stability

The notion of system stability is fundamental to the controls engineer. When perturbed from equilibrium, will the energy of the system increase, decrease, or remain constant with time? Stability of a two-port network is an open-ended question. In order to evaluate its

stability, one must first decide how it will be terminated. Let's consider a linear time-invariant two-port,  $\mathcal{N}$ , loaded by a second two-port,  $\mathcal{N}_L$ , as shown in Fig. 3.4.

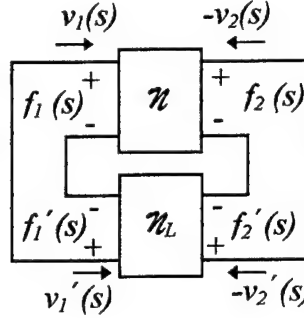


Fig. 3.4. Terminated Two-Port Network

The stability of the system can now be defined in terms of the roots of the closed-loop characteristic equation resulting from the termination of  $\mathcal{N}$  by a particular  $\mathcal{N}_L$ .

**Definition 3.2:** A terminated continuous linear two-port network is *stable* if and only if the corresponding characteristic equation has no roots in the right half  $s$ -plane and only simple roots on the imaginary axis.

Often, the exact loading to which a network will be subjected is not known. In this case, we would like to be able to characterize stability for a given class of loading conditions.

Of particular interest are *passive* two-port imbeddings.

**Definition 3.3:** The two-port network,  $\mathcal{N}_L$ , with initial energy storage  $\mathcal{E}(0)$  is *passive* if and only if,

$$\int_0^t (f_1'(\tau)v_1'(\tau) + f_2'(\tau)(-v_2'(\tau)))d\tau + \mathcal{E}(0) \geq 0 \quad \forall t \geq 0 \quad (3.4)$$

for all admissible forces  $(f_1', f_2')$  and velocities  $(v_1', -v_2')$ .

This means  $\mathcal{N}_L$  is incapable of delivering energy beyond that which has been previously been delivered to it. It is a passive absorber of energy. The stability problem is now reduced to finding under what condition the coupled system in Fig. 3.4 will remain stable for a passive, but otherwise arbitrary  $\mathcal{N}_L$ . The requirement is that an immittance matrix,  $P$ , characterizing  $\mathcal{N}$  must be *positive real* [28]. Valid immittance forms are impedance,  $Z$ ,



admittance,  $Y$ , hybrid,  $H$ , and alternate hybrid,  $G$ . The positive realness of any of these matrices is necessary and sufficient for the passivity of the linear network  $\mathcal{N}$ .

**Definition 3.4:** The two-port immittance matrix  $P$  is *positive real* if and only if  $P$  has no poles in the right half  $s$ -plane, only simple poles on the imaginary axis, and

$$\begin{aligned} \operatorname{Re}(p_{11}) &\geq 0, \quad \operatorname{Re}(p_{22}) \geq 0, \\ \operatorname{Re}(p_{11})\operatorname{Re}(p_{22}) - \left| \frac{p_{21} + p_{12}}{2} \right|^2 &\geq 0, \quad \forall \omega \geq 0. \end{aligned} \quad (3.5)$$

A special case of the arbitrary passive two-port loading described above is one which creates no cross-coupling between the ports of  $\mathcal{N}$ . Under this restriction,  $\mathcal{N}_L$  can be redrawn as two one-port terminations, as shown in Fig. 3.5.

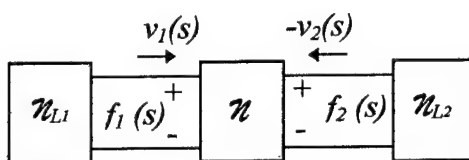


Fig. 3.5. Two-Port Network Terminated by One-Port Networks

Each of the imbedded one-ports are arbitrary passive networks. The stability of such a system can be described in terms of *absolute stability*. Necessary and sufficient conditions for absolute stability are provided by Llewellyn's stability criteria [42].

**Definition 3.5:** A network characterized by the two-port immittance matrix  $P$  is *absolutely stable* if and only if  $P$  has no poles in the right half  $s$ -plane, only simple poles on the imaginary axis, and

$$\begin{aligned} \operatorname{Re}(p_{11}) &\geq 0, \\ 2\operatorname{Re}(p_{11})\operatorname{Re}(p_{22}) &\geq |p_{12}p_{21}| + \operatorname{Re}(p_{12}p_{21}), \quad \forall \omega \geq 0. \end{aligned} \quad (3.6)$$

Together, these two inequalities imply  $\operatorname{Re}(p_{22}) \geq 0$ .

We will also make use of the term *potential instability*,

**Definition 3.6:** A two-port network is *potentially unstable* if it is not absolutely stable.

The conditions for the passivity of  $\mathcal{N}$  and those for its absolute stability can be compared using a *stability-activity diagram* [43]. To simplify notation, it is useful to define some intermediate variables,

$$r_{11} = \operatorname{Re}(p_{11}) \quad (3.7)$$

$$r_{22} = \operatorname{Re}(p_{22}) \quad (3.8)$$

$$r_{121} = \operatorname{Re}(\sqrt{p_{12}p_{21}}). \quad (3.9)$$

Note that both (3.5) and (3.6) require the driving point functions to have non-negative real parts. The difference between passivity and absolute stability lies in the last inequality of each condition. The final condition for passivity in (3.5) can be rewritten in terms of the intermediate variables as,

$$\frac{r_{121}^2}{r_{11}r_{22}} + \frac{(|p_{12}| - |p_{21}|)^2}{4r_{11}r_{22}} \leq 1. \quad (3.10)$$

Likewise, the last condition for absolute stability in (3.6) can be expressed as,

$$\frac{r_{121}^2}{r_{11}r_{22}} \leq 1. \quad (3.11)$$

By judiciously choosing a set of dimensionless variables,

$$x = \frac{r_{121}}{\sqrt{r_{11}r_{22}}} \quad \text{and} \quad y = \frac{\|p_{12}\| - \|p_{21}\|}{2\sqrt{r_{11}r_{22}}}, \quad (3.12)$$

we find that (3.10) delineates the interior of a unit circle,  $x^2 + y^2 = 1$ , and (3.11) defines the area to the left of a vertical line at  $x = 1$ . Since  $x$  and  $y$  are always positive, we are only interested in the upper-right quadrant of the  $x$ - $y$  plane. The resulting stability-activity diagram is shown in Fig. 3.6. It is clear that a passive network will always be absolutely stable, but an absolutely stable network is not necessarily passive. By examining  $y$  in (3.12), we observe the discrepancy between passivity and absolute stability is created by

the difference in the magnitude of the off-diagonal terms of the immittance matrix. In fact, the two criteria are identical for the special case of a *reciprocal* network  $\mathcal{N}$ .

**Definition 3.7:** A network characterized by a valid immittance form is *reciprocal* if any of the following are true:

$$z_{21} = z_{12}, \quad y_{21} = y_{12}, \quad h_{21} = -h_{12}, \quad \text{or} \quad g_{21} = -g_{12}.$$

For a reciprocal network, the stability-activity diagram collapses to a line at  $y = 0$  and the criteria for both passivity and absolute stability become  $x \leq 1$ .

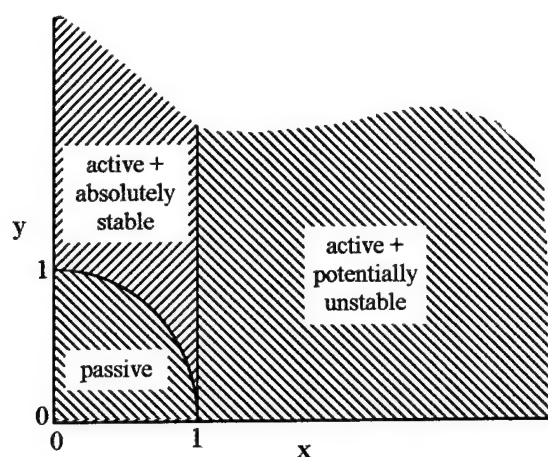


Fig. 3.6. Stability-Activity Diagram

## Chapter 4

### Two-Port Framework for Haptic Interaction

The goal of control law design for haptic displays is to provide the human operator with a compelling sense of haptic presence in a virtual environment, while guaranteeing the stability of the overall system. To ensure safe operation, preventing physical harm to both man and machine, the total energy of the system must remain bounded. Network theory and two-port models are invaluable in characterizing the energetic interactions within a haptic system. Fig. 4.1 shows the three primary elements in a network model of haptic simulation: the human operator, the virtual environment, and the haptic interface [44].

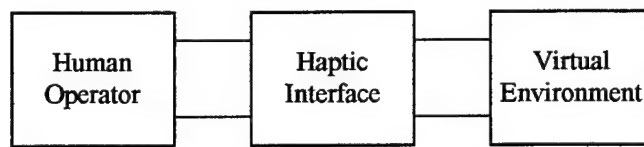


Fig. 4.1. Network Model of Haptic Simulation

The central element in this model is the *haptic interface*, a two-port which characterizes the exchange of energy between the human and the virtual world. It is critical in both stability and performance analysis. The haptic interface two-port is terminated at one end by the human operator, who physically interacts with the device at the point of human-machine contact. At the other end is the virtual environment, which creates a velocity-force relationship at a point of information exchange with the control elements of the haptic interface. If we assume the human operator and the virtual environment are arbitrary passive one-ports, then, by definition, the haptic simulation is guaranteed stable if the haptic interface two-port is *absolutely stable*. The concept is illustrated in Fig. 4.2.

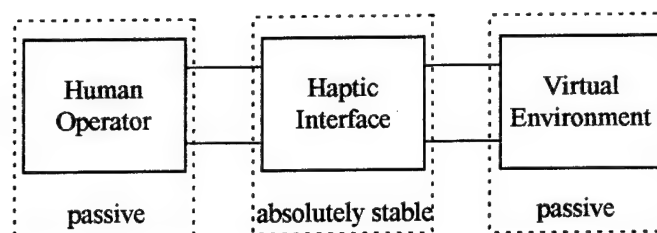


Fig. 4.2. Stable Haptic Simulation

Considerable attention will be given to achieving an absolutely stable haptic interface two-port. Before exploring methods to realize this goal, we should investigate the properties of the terminal elements of the haptic simulation, upon which the overall stability result is predicated. The following sections examine the human operator and virtual environment in more detail.

#### 4.1 The Human Operator

It is both impractical and unnecessary to develop a complete biological/behavioral model of the human operator. We are interested only in the biomechanical interactions between the human and the haptic device. No passive contact between the two should ever result in an unstable system. For example, in the case of a hand controller, the operator should be able to grasp the handle lightly, tightly, or not at all, without inducing undamped motion. More formally speaking, the human should be unable to destabilize the system by modulating limb impedance using muscular contraction or changes in musculoskeletal geometry (posture). This does not preclude erratic motion intentionally induced by the operator. The haptic interface should not prevent the user from making willful movements.

Since we are only interested in the biomechanical properties of the human operator, a greatly simplified model of human impedance is possible. Hogan showed a human interacting with a hand controller could be modeled as an arbitrary passive impedance [29], [30]. By demonstrating its inherently spring-like behavior, he showed the human

arm would remain stable when coupled to any passive mechanical device. There are two means by which a subject can change the impedance properties of a limb. The first is by symmetrically modulating muscle activation (i.e. tight or loose grip). By increasing muscle tension, effective joint stiffness is magnified. The second is by changing limb posture, thereby altering the kinematic relationship between motion in joint-space and Cartesian-space. For the human arm, maximum stiffness is achieved in the radial direction (shoulder to hand) by fully extending the elbow. Elbow stiffness in that direction theoretically becomes infinite, leaving shoulder musculature as the primary source of compliance. The dominant effect of musculoskeletal geometry on Cartesian-space stiffness of the human arm was confirmed by Mussa-Ivaldi et. al. [45]. They experimentally derived stiffness ellipses for different arm postures on several human subjects. Among four subjects, the highest level of stiffness measured was  $825 \text{ N/m}$ , achieved at an elbow-extended posture.

While experimental studies suggest the validity of a passive characterization of human impedance, another more heuristic argument can be made. In everyday experience, we do not encounter instability when manipulating passive physical objects. If the haptic interface presents a passive port to the human operator, the device will always appear to the human as an inanimate object. It will behave as a collection of masses, springs, dampers, unilateral constraints, and other passive elements. None of these has the ability to generate energy, only to give back or absorb the energy which the human creates. Such a device can never be the source of an instability, no more than a real-life inanimate object, such as a pencil, could. The human operator is free to force undamped motion through intentional excitation, but the haptic interface will not contribute to a buildup of kinetic or potential energy.

For some haptic interfaces, representing the human operator as an arbitrary passive impedance can actually be overly conservative. Arbitrary passivity allows for the extreme cases of zero human impedance (no contact with the device) and a perfectly rigid (infinitely stiff) human grasp. If the operator is somehow attached to the haptic device, so

that contact cannot be broken, we may want to assume some minimum level of human impedance,  $Z_{\min}$ . On the other hand, no matter how the human interacts with the haptic interface, the operator will never achieve infinite stiffness. Conservatism due to overestimation of human stiffness can be eliminated by postulating a maximum impedance level,  $Z_{\max}$ , for the operator. Fig. 4.3 shows how the model of haptic simulation can be modified to include minimum and maximum levels of human impedance.

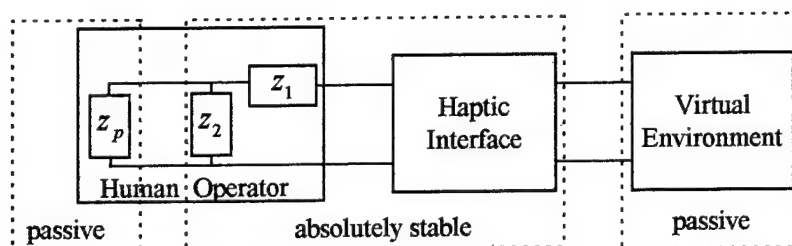


Fig. 4.3. Human Operator Impedance Model

We characterize the human operator in terms of three impedances,  $Z_p$ ,  $Z_1$ , and  $Z_2$ .  $Z_p$  is an arbitrary passive impedance function,  $Z_1 = Z_{\min}$ , and  $Z_2 = Z_{\max} - Z_{\min}$ . Notice that when  $Z_p$  is zero (short circuit) the resulting human impedance is  $Z_{\min}$ . When  $Z_p$  is infinite (open circuit), the resulting human impedance is  $Z_1 + Z_2 = Z_{\max}$ . These characterizations of minimum and maximum human impedance are included with the haptic interface in the test for absolute stability. The improved human operator representation makes it easier to guarantee the stability of the haptic simulation, bringing theoretical results closer to experimental observations.

## 4.2 The Virtual Environment

The virtual environment is a computer generated model of a physically motivated scene. It provides the haptic interface with a relationship between motions and forces which reflect the dynamics at a port of interaction within the virtual world. The virtual environment is defined by the application. In a surgery simulator, it may represent the interaction

between a surgeon's tools and the patient's tissue. In a CAD program, it may simulate the interactions between parts in an assembly.

Since the virtual environment is a computer simulation of reality, it is a digital process. Velocities and forces at the port of interaction between the environment and the haptic interface are defined only at discrete instances in time. This is in contrast to the interaction port between the haptic interface and the human operator, which is characterized by continuous variables. We will distinguish between the two by referring to the former case as an *information port*, the latter as a *physical port*. In the absence of a modifier, the term *port* implies *physical port*.

The human operator affects the velocity,  $v_h$ , and force,  $f_h$ , at the physical port of contact with the haptic interface. The virtual environment modulates the velocity,  $v_e^*$ , and force,  $f_e^*$ , at the information port between the haptic interface and the virtual environment. The star superscript identifies a discrete variable. These variables are shown in Fig. 4.4.

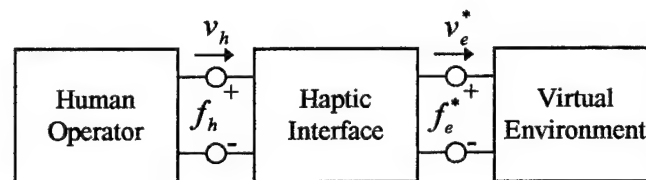


Fig. 4.4. Revised Network Model of Haptic Simulation

An implementation of a virtual environment defines a relationship between  $v_e^*$  and  $f_e^*$ . One of these must be identified as an input, the other as an output to the digital simulation. There are thus two possible classes of implementations. *Impedance environments* accept velocities (or positions) and generate forces. *Admittance environments* accept forces and return velocities (or positions).

Impedance environments have to-date been the most prevalent in haptic simulations. A common example is the ubiquitous virtual wall simulation, defined simply as



$f_e^* = K(x_e^* - x_{wall}^*)$  if  $x_e^* > x_{wall}^*$  and  $f_e^* = 0$  otherwise. The environmental position,  $x_e^*$ , is the integral of the velocity,  $v_e^*$ . This virtual wall model is an example of a penalty based approach, the most common form of impedance environment [10], [12], [14], [17], [31]. The main advantage of penalty methods is the ease of implementing static virtual worlds. They can be formulated simply as three-dimensional extensions of the virtual wall model above. The disadvantage of the penalty approach becomes apparent when implementing more complex, dynamic simulations. The spring-based model of the environment leads to a stiff set of differential equations which is difficult to stably integrate with a reasonable step size.

Admittance environments are finding increased acceptance in haptic simulations. In an admittance environment, the motion of an object is calculated in response to an external force. When objects collide, the response is often derived using constraint based techniques. A simple constraint based admittance implementation of a virtual wall would first calculate the response,  $v_e^*$ , of an object to an applied force,  $f_e^*$ . If the updated object position,  $x_e^*$ , penetrated the virtual wall,  $x_e^* > x_{wall}^*$ , then it would set  $x_e^* = x_{wall}^*$  and  $v_e^* = 0$ . More complex simulations require considerably more involved computations. Constraint approaches are already common in the computer science community for physics based modeling. The primary disadvantage of these techniques for haptics is the use of back-stepping in time to determine the exact moment of a collision. The resulting simulation cannot guarantee a deterministic frame rate which is required to ensure the stability of the haptic system. Enhancements to existing algorithms and increased computing power at reduced cost should soon overcome this problem. A number of admittance environments have already been successfully demonstrated [36], [46], [47].

The framework proposed in this work requires the virtual environment to create a passive mapping between the information port variables,  $v_e^*$  and  $f_e^*$ . It is intuitive that the simulation of physically motivated effects (masses, springs, dampers) with a virtual world

should obey the energy conservation laws of physics, and thus be passive. However, formulating numerical integration routines which achieve strict adherence to these laws can be difficult. Brown [35] showed that explicit discrete-time passive integration of the equations of motion is impossible. The current output of an explicit integration routine is a function only of previous input values. Implicit integration routines (current output is a function of current as well as past inputs) can be passive, but they must be solved using iterative techniques which are not conducive to real-time simulation. Fortunately, experience has demonstrated that absolutely stable haptic interfaces are very robust when coupled to explicit virtual environments which are “almost” passive [34], [48].

If the activity in an explicit virtual environment can be characterized and bounded, it may be possible to design a haptic interface which accounts for the non-passivity of the integration routine. Such a haptic interface must supply enough additional passivity to offset virtual environment activity. The concept is illustrated in Fig. 4.5.

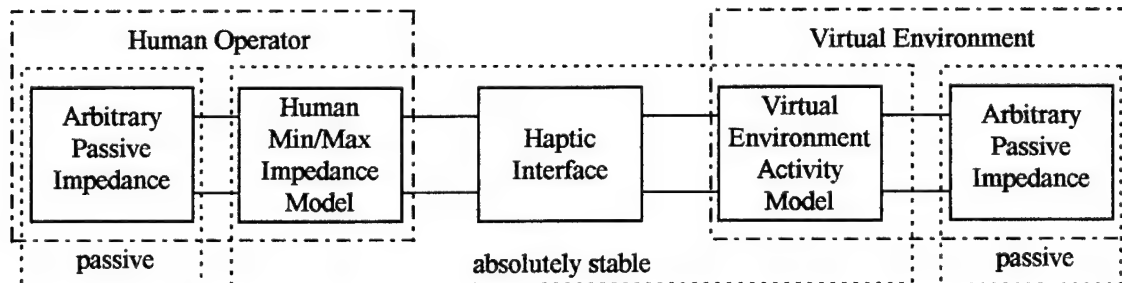


Fig. 4.5. Stable Haptic Simulation with Virtual Environment Activity and Human Impedance Models

Efficient representation of the activity of an explicit integration algorithm is an unsolved problem. One of the biggest challenges in describing environmental activity is that its level is a function of the virtual environment parameters (mass, damping, etc.), so any characterization is model dependent.

### 4.3 The Haptic Interface

The haptic interface network encompasses everything that comes between the human operator and the virtual environment. It plays the role of translator between the real and the virtual world. To better understand the stability properties of the system, we separate the haptic interface into a cascade combination of two sub-networks. One of these is the haptic display, a mechanical device configured to convey kinesthetic cues to a human operator. The second is a virtual coupling network, an application-independent control element which connects the haptic display to the virtual environment. These two components are shown in Fig. 4.6.

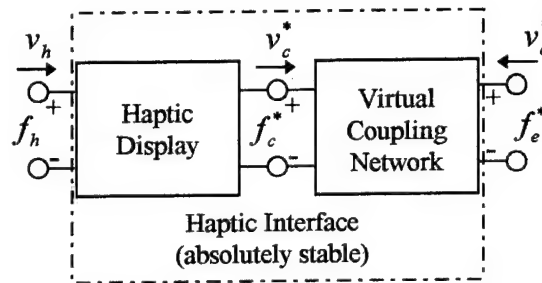


Fig. 4.6. Haptic Interface Two-Port

#### 4.3.1 The Haptic Display

Haptic displays vary greatly in kinematic structure, workspace, and force output. They can be broadly classified into two categories, those which “measure motion and display force” and those which “measure force and display motion” [38]. The former are referred to as *impedance displays*, the latter as *admittance displays*.

##### 4.3.1.1 Impedance Displays

A mechanical device which is configured to render a commanded force while providing a measurement of its position and/or velocity is called an impedance display. In this implementation, the variable  $f_c^*$  in Fig. 4.6 is an input to the haptic display and  $v_c^*$  is an output of the haptic display. Impedance displays typically have low inertia and are highly back-drivable. The well known PHANTOM [12] family of haptic displays (Fig. 1.1), the University of Washington PBF [14] (Fig. 1.2), and the McGill University Pantograph [49] (Fig. 4.7) fall into this class, along with many others.

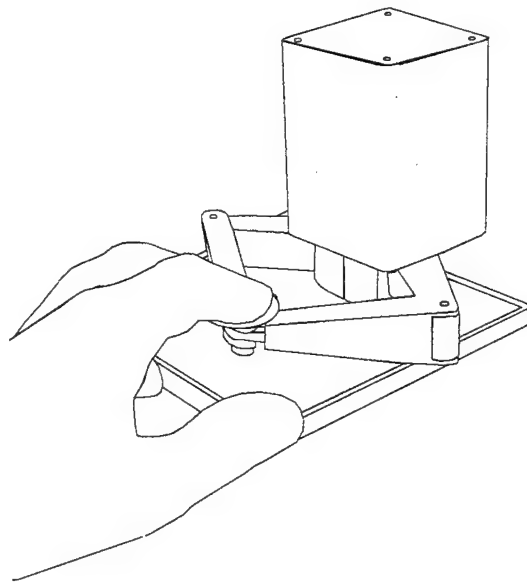


Fig. 4.7. McGill University Pantograph

#### 4.3.1.2 Admittance Displays

A device configured to track a commanded position or velocity while providing a measurement of force is called an admittance display. In this case, the variable  $v_c^*$  in Fig. 4.6 is an input to the haptic display and  $f_c^*$  is an output of the haptic display. Admittance displays are often high-inertia, non back-drivable manipulators fitted with force sensors and driven by a position or velocity control loop. Examples include Carnegie Mellon University's WYSIWYF Display [50] and the Iowa State/Boeing virtual aircraft control column [51] (Fig. 4.8), both of which are based upon PUMA 560 industrial robots.

The choice of an impedance or admittance display implementation is often driven by practical considerations. An impedance implementation can be the simplest and least expensive option, all that is required is an actuator and a measurement of position or velocity. The addition of a force sensor, required for an admittance display implementation, may not be practical on a very small, lightweight device such as the PBFD. On the other hand, a non-backdrivable manipulator or a system with high-gear ratios may not be amenable to an impedance implementation. Such devices are more likely

found in a research or industrial setting, where the additional complexity and cost of an admittance implementation are more tenable. In some cases, the choice of an impedance or admittance implementation is not as obvious. The University of Washington HBFD (Fig. 1.3) and HTI's Excalibur (Fig. 1.4) are back-drivable devices which are equipped with force sensing. They may be configured as either impedance or admittance displays, resulting in the following question. Which implementation yields the best performance with guaranteed stability? An answer is pursued in the following chapters.

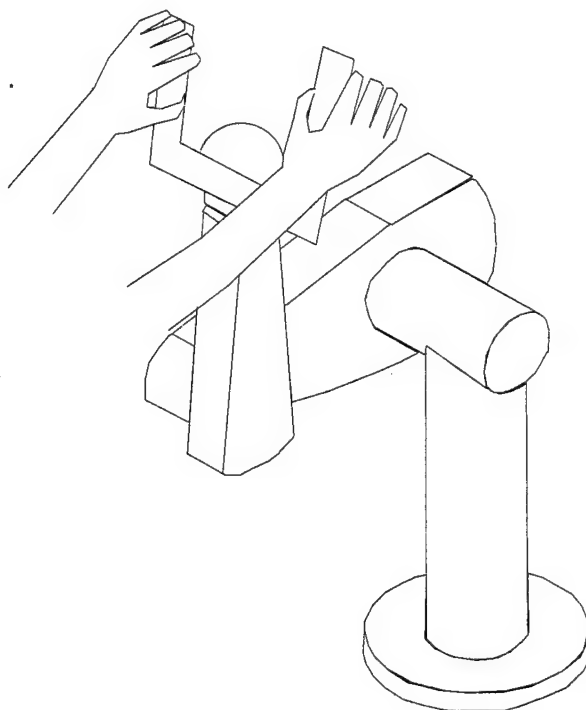


Fig. 4.8. A PUMA-based Haptic Display

#### 4.3.2 Virtual Coupling Network

Within the framework described in this thesis, the control engineer designs the virtual coupling network so the combined haptic interface two-port satisfies the conditions for absolute stability. The purpose of the virtual coupling is to make overall system stability independent of both the human operator and the virtual environment. It is a digital system, implemented in software, although it is often constructed to emulate the dynamics

of a mechanical system. The simplest form of a virtual coupling is a virtual spring-damper connected in parallel, which links the haptic display to the virtual environment. This type of coupling, while not directly designed for absolute stability, previously found application in connecting impedance displays to admittance environments [33], [36]. A graphical depiction of this special case is shown in Fig. 4.9. The haptic display, in this case a PHANTOM fingertip device, is linked to a virtual object through a virtual spring-damper. When the object collides with an infinitely rigid virtual wall, it is constrained to lie on its surface. The user 'feels' the virtual wall through the virtual coupling. When the virtual spring is stiff, the virtual wall feels stiff.

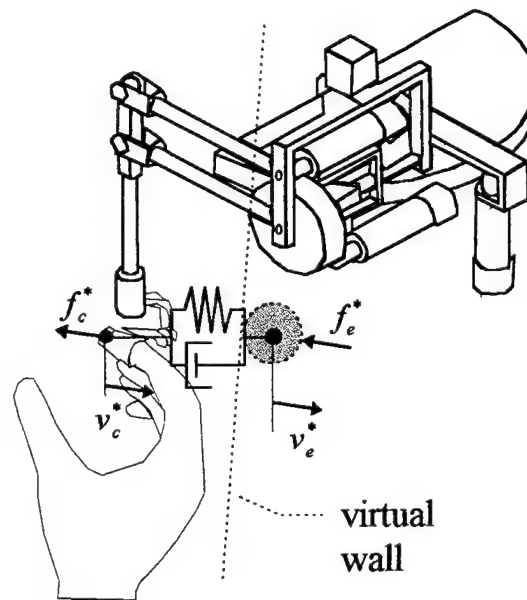


Fig. 4.9. Spring-Damper Virtual Coupling

For this simple coupling scheme, it is possible to experimentally tune the virtual stiffness and damping to achieve a stable simulation. This iterative approach is taken in previous virtual coupling implementations [36]. A more direct approach is to find explicit conditions which the virtual coupling must meet to achieve absolute stability. If the coupling parameters, stiffness and damping, are set such that the haptic interface is absolutely stable, then contact with the virtual wall (assumed to be passive) is guaranteed

to be stable. The absolute stability requirement limits the maximum achievable impedance of the coupling. If the stiffness parameter is set too high, the conditions for absolute stability will be violated and the simulation may become unstable. The following chapters reveal that this direct approach provides considerable intuition into the control design problem, intuition which is lost in the iterative tuning approach.

While the example above highlights the role of the virtual coupling network in achieving stability, it illustrates only one specific case, an impedance display linked to an admittance environment. A total of four combinations of haptic display and virtual environment implementations are possible: impedance display/impedance environment, impedance display/admittance environment, admittance display/impedance environment, and admittance display/admittance environment. The particular combination chosen defines the *causality structure* of the haptic simulation. The causality structure determines the inputs and outputs of the virtual coupling. For the example given above,  $v_c^*$  and  $v_e^*$  are inputs to the virtual coupling network,  $f_c^*$  and  $f_e^*$  are outputs. While this case has received some attention in the literature, the other three have not. This work addresses all four causality structures and provides a formal procedure for the construction of stabilizing virtual coupling networks. Details are presented in subsequent chapters.

#### 4.4 Performance

The haptic interface acts as a translator between port variables at the human operator and the virtual environment. Ideally, a haptic interface would be transparent, simply passing through these variables with minimal distortion. Transparency is the degree to which velocities and forces at one port match those at the other. A two-port with perfect transparency has the hybrid mapping [22],

$$\begin{bmatrix} f_h \\ -v_e^* \end{bmatrix} = \begin{bmatrix} 0 & 1 \\ -1 & 0 \end{bmatrix} \begin{bmatrix} v_h \\ f_e^* \end{bmatrix}. \quad (4.1)$$

Another measure of haptic performance, Z-width, was proposed by Colgate and Brown [52]. The Z-width of a haptic interface can be defined as the achievable range of impedance which it can stably present to the operator. This range is delimited by frequency dependent lower and upper bounds,  $Z_{\min}$  and  $Z_{\max}$ . An ideal haptic interface could simulate free motion without inertia or friction, as well as infinitely rigid and massive objects. In reality, the degree to which ideal performance is realized is limited by considerations of system stability. The Z-width bounds of an absolutely stable haptic interface two-port can easily be derived by exploring the limits of virtual environment impedance.  $Z_{\min}$  is determined by setting  $f_e^* = 0$  (short circuit, zero impedance environment).  $Z_{\max}$  is found by setting  $v_e^* = 0$  (open circuit, infinite impedance environment). These conditions are illustrated in Fig. 4.10.

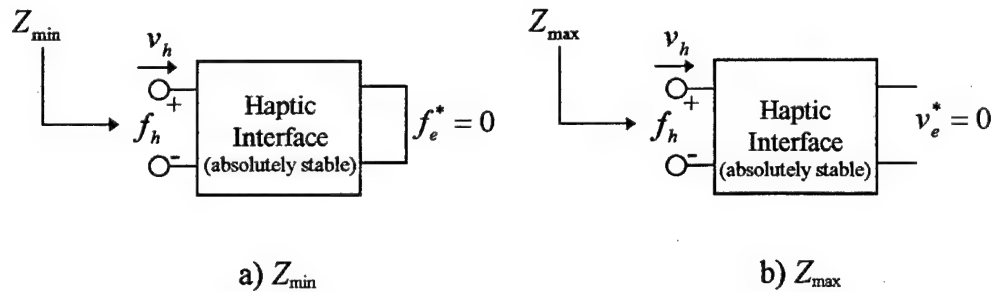


Fig. 4.10. Impedance Range

#### 4.5 Human-Virtual Environment Coupling

The network model of haptic simulation shown in Fig. 4.1 assumes that the human operator and the virtual environment are coupled only through the haptic interface. In most applications, this is not strictly true. Almost all haptic simulations also include an element of visual feedback between the virtual environment and the human. Some also include audio information. These additional sensory pathways create relationships between the behavior of the human operator and the state of the environment which may result in instabilities. The nature of such coupling is highly application specific.



Fortunately, it is highly unlikely that the addition of visual or audio feedback will cause an instability which is threatening to the human operator. There is a *frequency separation* between haptic interaction and the other sensory modes which permits issues of biomechanical stability to be treated apart from stability issues related to these other modes of interaction. Unstable modes of oscillation induced by adverse energetic interactions at the point of human-machine contact typically occur at frequencies above *10 Hz*. Human responses to visual and audio information must pass through the central nervous system, limiting the bandwidth of these higher level interactions to about *3 Hz*.

## Chapter 5

### Benchmark Problem

The following example, while simple, encompasses many of the most important factors which affect the stability and performance of haptic interfaces. These include open-loop device impedance, sample-hold effects, and, in the case of admittance displays, velocity loop bandwidth and closed-loop compliance. This benchmark problem reveals a number of fundamental issues in designing stable haptic interfaces and exposes an important duality between the impedance and admittance models of haptic interaction [53]. We consider a one degree-of-freedom, rigid manipulator with mass  $m$  and damping  $b$ , shown in Fig. 5.1.

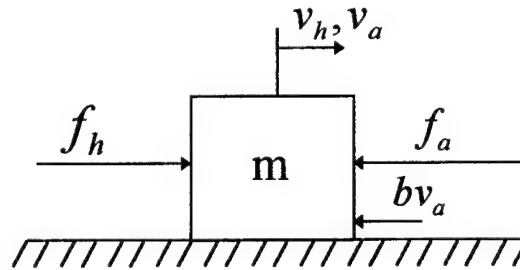


Fig. 5.1. A Benchmark Haptic Display

This device is governed by the equations of motion,

$$m\dot{v}_a + bv_a = f_h - f_a, \quad v_a = v_h. \quad (5.1)$$

The force of actuation,  $f_a$ , directly opposes the force applied by the human operator,  $f_h$ .

Since the device is rigid, the velocity at the handle,  $v_h$ , and the velocity at the point of actuation,  $v_a$ , are identical.

#### 5.1 Impedance Display

In the impedance model of haptic interaction, forces are applied to the human operator in response to measured displacements. It is straightforward to form an impedance display from the equations of motion of our benchmark system. The corresponding hybrid mapping is,

$$\begin{bmatrix} f_h \\ -v_a \end{bmatrix} = \begin{bmatrix} ms+b & 1 \\ -1 & 0 \end{bmatrix} \begin{bmatrix} v_h \\ f_a \end{bmatrix}. \quad (5.2)$$

### 5.1.1 Conventional Design

The causality structure best represented in the literature is impedance display/impedance environment [10], [12], [13], [17], [31]. One implementation of this structure is simply to set  $v_a = v_e$  and  $f_a = f_e$ . The resulting continuous-time immittance matrix is reciprocal and satisfies both the conditions for passivity (3.5) and absolute stability (3.6). We might be tempted to think our job is finished. To better understand the problem, sample-hold effects must be included. Fig. 5.2 shows the implementation of a sampled-data system using a zero-order hold on the force command input,  $f_c^*$ , and sampling the device velocity to get  $v_c^*$ .

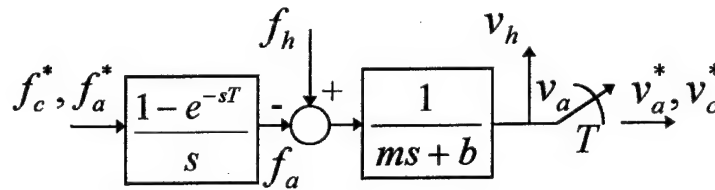


Fig. 5.2. Benchmark Impedance Display

The open loop device dynamics are discretized using Tustin's method which preserves the passivity of the impedance function [54],

$$Z_{d_l}(z) = (ms+b) \Big|_{s \rightarrow \frac{2}{T} \left( \frac{z-1}{z+1} \right)}. \quad (5.3)$$

To maintain simplicity in the analysis, we assume that any aliasing effects due to sampling are negligible, thanks either to the low-pass filtering effect of device dynamics or the introduction of an appropriate anti-aliasing filter before sampling. The zero-order hold can then be approximated as a low-pass filter with a steady state gain of  $T$  and 90 degrees phase lag at the Nyquist frequency. The sampler can be approximated as a static gain of

$1/T$ . With no loss of generality we can combine the sampler gain with the zero-order hold to get the normalized zero-order hold function,

$$ZOH(z) = \frac{1}{2} \frac{(z+1)}{z}. \quad (5.4)$$

We can now form the discrete hybrid matrix of the impedance display,

$$\begin{bmatrix} f_h \\ -v_c^* \end{bmatrix} = \begin{bmatrix} Z_{d_i}(z) & ZOH(z) \\ -1 & 0 \end{bmatrix} \begin{bmatrix} v_h \\ f_c^* \end{bmatrix}. \quad (5.5)$$

Note that (5.5) is not reciprocal ( $h_{12} \neq -h_{21}$ ). We test the impedance display for absolute stability by applying (3.6) to (5.5) to get,

$$\frac{\text{Re}(ZOH(z))}{|ZOH(z)|} \geq 1 \Leftrightarrow \cos(\angle ZOH(z)) \geq 1. \quad (5.6)$$

Since the zero-order hold (5.4) has a non-zero phase lag for  $0 < \omega < 2\pi/T$ , this condition is never satisfied. Thus, we see that, with  $v_d^* = v_e^*$  and  $f_c^* = f_e^*$ , the haptic interface will never be absolutely stable. This does not mean that the haptic simulation will necessarily be unstable, only that some combination of passive human operator and virtual environment exists that will destabilize the system. The biomechanical impedance properties of the human operator are unpredictable. The operator may decide to grasp the manipulator tightly, or release it altogether. It is difficult to guarantee stability when it is dependent on human operator behavior. We would therefore like to maintain a stable system for any level of human interaction, the only restriction being that the human operator is passive. In this conventional approach, it is left to the designer of the virtual environment to create a simulation which guarantees the stability of the haptic simulation. For complex virtual environments, this leads to a highly iterative tuning process which at best gives a conservative result. Since it is difficult to consider all possible events and configurations in a virtual world, even after this costly tuning procedure, there is no guarantee of stability. Additionally, this approach ties the design of the virtual environment to a specific haptic display. If a different display is coupled to the same environment, the system's stability properties change. This problem motivates the

introduction of a virtual coupling network which guarantees the stability of a haptic interface when coupled with any passive virtual environment and human operator.

### 5.1.2 Proposed Design Procedure

We now specify the haptic interface to be the cascade combination of a haptic display and a virtual coupling network. Our goal becomes to design the virtual coupling network such that the combined system is absolutely stable. Fig. 5.3 illustrates the concept.

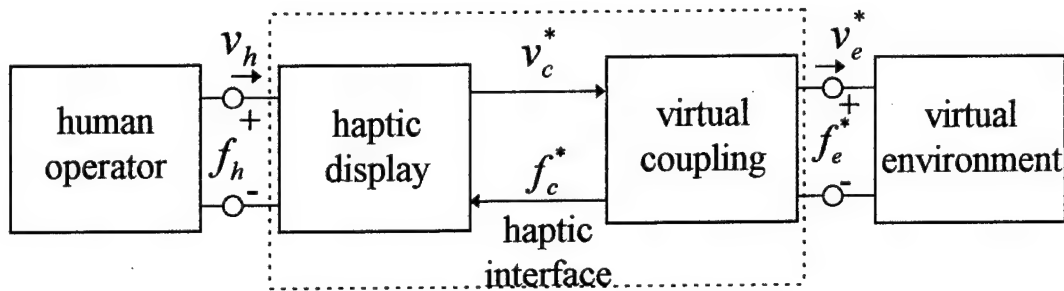


Fig. 5.3. Haptic Simulation with Impedance Display

In general, the virtual coupling network can have arbitrary structure. A physically motivated implementation is a spring-damper with stiffness,  $k_c$ , and damping,  $b_c$ , linking the haptic display to the virtual environment. Fig. 5.4 shows the mechanical analog of this coupling.

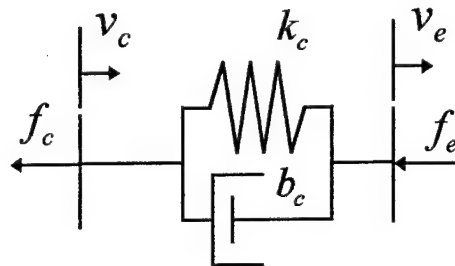


Fig. 5.4. Mechanical Analog of Spring-Damper Virtual Coupling

If we simulate an infinitely stiff environmental constraint, the stiffness perceived by the human operator is not infinite, but that of the virtual coupling. An optimal stability-

performance trade-off is achieved when virtual coupling stiffness is maximized, while preserving the absolute stability of the combined two-port.

Discretization of virtual coupling impedance is performed using a first difference approximation,

$$Z_{c_i}(z) = \left( b_c + \frac{k_c}{s} \right) \Big|_{s \rightarrow \left( \frac{z-1}{Tz} \right)}. \quad (5.7)$$

The hybrid mapping of the virtual coupling network is,

$$\begin{bmatrix} f_c^* \\ -v_e^* \end{bmatrix} = \begin{bmatrix} 0 & 1 \\ -1 & \frac{1}{Z_{c_i}(z)} \end{bmatrix} \begin{bmatrix} v_c^* \\ f_e^* \end{bmatrix}. \quad (5.8)$$

The hybrid mapping for the haptic interface is the cascade connection of the impedance display with the virtual coupling network,

$$\begin{bmatrix} f_h \\ -v_e^* \end{bmatrix} = \begin{bmatrix} Z_{d_i}(z) & ZOH(z) \\ -1 & \frac{1}{Z_{c_i}(z)} \end{bmatrix} \begin{bmatrix} v_h \\ f_e^* \end{bmatrix}. \quad (5.9)$$

Note that the only change from (5.5) to (5.9) is the insertion of the virtual coupling term in the lower-right block. Directly applying (3.6), the criteria for absolute stability are,

$$\operatorname{Re}(Z_{d_i}(z)) \geq 0, \operatorname{Re}(1/Z_{c_i}(z)) \geq 0, \quad (5.10)$$

and

$$\cos(\angle ZOH(z)) + \frac{2 \operatorname{Re}(Z_{d_i}(z)) \operatorname{Re}(1/Z_{c_i}(z))}{|ZOH(z)|} \geq 1. \quad (5.11)$$

We can make the following observations about (5.10) and (5.11),

- $\operatorname{Re}(Z_{d_i}(z))$  can be interpreted as the physical damping of the impedance display. It must be non-zero and positive for absolute stability to be possible. This is the level of damping the human operator feels when the virtual environment simulates free motion.

- $\text{Re}(1/Z_{c_i}(z))$  can be interpreted as the conductance of the virtual coupling. This function dictates the amount of “give” the human operator perceives in the haptic display when the virtual environment simulates a rigid constraint. Some minimum positive value of this “give” is necessary to achieve absolute stability.
- Larger values of  $\text{Re}(Z_{d_i}(z))$  permit smaller values of  $\text{Re}(1/Z_{c_i}(z))$ . This means that increasing device damping increases the maximum impedance that can be presented to the human operator. If we want to simulate rigid contact, significant physical damping in the haptic device is required. This observation is consistent with those made by Brown and Colgate [52].
- $\angle ZOH(z)$  is the phase loss due to sample-hold effects. Reducing the sampling frequency will cause an increase in this phase loss and require an augmentation in either device damping or “give” in the virtual coupling to maintain absolute stability. Manipulating (5.11) gives us the following condition for absolute stability.

$$\text{Re}(1/Z_{c_i}(z)) \geq \frac{1 - \cos(\angle ZOH(z))}{2 \text{Re}(Z_{d_i}(z))} |ZOH(z)| \quad (5.12)$$

Both sides of this inequality are functions of frequency. We now have a design procedure for the virtual coupling network. Plot the right-hand side of (5.12) versus frequency, then synthesize  $1/Z_{c_i}(z)$  so that its real part is positive and exceeds this lower-bound.

Note that if the inequality (5.12) holds, absolute stability is satisfied, regardless of whether an impedance or admittance type virtual environment is used. The only difference is in the implementation. The hybrid mapping of the virtual coupling network, (5.8), links the haptic display to the virtual environment in the impedance display/impedance environment case. If the virtual environment is modeled as an admittance, as is the case when using constraint based simulations, the same virtual coupling is implemented as,

$$\begin{bmatrix} f_c^* \\ f_e^* \end{bmatrix} = \begin{bmatrix} Z_{c_i}(z) & Z_{c_i}(z) \\ Z_{c_i}(z) & Z_{c_i}(z) \end{bmatrix} \begin{bmatrix} v_c^* \\ -v_e^* \end{bmatrix}. \quad (5.13)$$

We can therefore design the haptic interface without considering the virtual environment implementation, as long as it is passive. An interesting note is that a virtual coupling will always be needed to implement dissimilar causality structures. Without a coupling network, an impedance display must be paired with an impedance environment. Likewise, an admittance display could only be used with an admittance environment. The virtual coupling network permits all four causality structures to be used.

The hybrid matrix of the combined haptic interface network, (5.9), illustrates that to best approximate perfect transparency, (4.1),  $Z_{c_i}(z)$  should be as large as possible. This means for performance, we want high virtual stiffness and virtual damping. The best virtual coupling is therefore one that makes (5.12) an equality, providing the minimum level of compliance for absolute stability. The performance of the haptic interface can be quantified in terms of lower and upper bounds on the impedance perceived by the human operator,  $Z_p$ . By terminating the virtual environment port of (5.9),  $f_e^* = Z_e v_e^*$ , we can calculate the resulting one-port impedance function,

$$Z_p = \frac{f_h}{v_h} = Z_{d_i}(z) + \frac{Z_{c_i}(z)ZOH(z)Z_e}{Z_{c_i}(z) + Z_e}. \quad (5.14)$$

This is the impedance felt by the human operator for a given virtual environment,  $Z_e$ . The lower bound on  $Z$ -width is calculated by letting  $Z_e \rightarrow 0$ . The minimum impedance that an impedance-type haptic device can simulate is limited by its open-loop inertia and friction,

$$Z_{\min_I} = Z_{d_i}(z). \quad (5.15)$$

The upper bound is calculated by letting  $Z_e \rightarrow \infty$ . The resulting maximum impedance is the impedance of the open-loop device plus that of the virtual coupling.

$$Z_{\max_I} = Z_{d_i}(z) + Z_{c_i}(z)ZOH(z). \quad (5.16)$$

The two functions,  $Z_{\min_I}$  and  $Z_{\max_I}$ , define the  $Z$ -width of the haptic interface. We can combine (5.15) and (5.16) to get,

$$Z_{\max_I} = Z_{\min_I} + Z_{c_i}(z)ZOH(z). \quad (5.17)$$



This implies that to maximize  $Z$ -width, we should maximize virtual coupling impedance, or equivalently, minimize virtual coupling compliance.

## 5.2 Admittance Display

In the admittance model of haptic interaction, the display generates displacements in response to measured forces. We can derive such a display by adding a proportional-plus-integral ( $PI$ ) velocity control loop,

$$f_a^* = K_{PI}(z)(v_a^* - v_c^*), \quad (5.18)$$

and measuring force at the point of device-human contact. Note that  $PI$  feedback of velocity is equivalent to proportional-plus-derivative feedback of position. The  $PI$  form is used here for consistency in notation.  $v_c^*$  is the commanded velocity and  $f_c^* = f_m^*$  is the measured force. The admittance display is implemented according to Fig. 5.5.

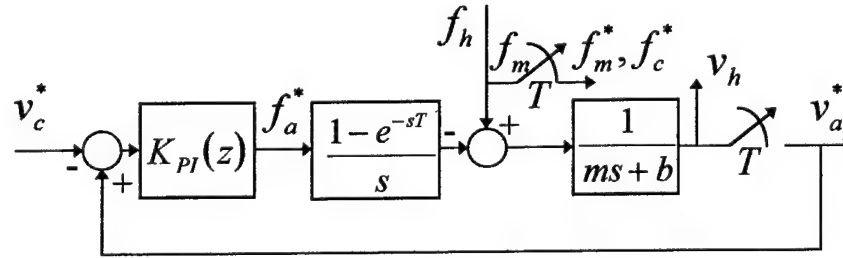


Fig. 5.5. Benchmark Admittance Display

The resulting alternate hybrid mapping for the discretized display is

$$\begin{bmatrix} v_h \\ f_c^* \end{bmatrix} = \begin{bmatrix} \frac{1}{Z_{d_A}(z)} & -T(z) \\ 1 & 0 \end{bmatrix} \begin{bmatrix} f_h \\ -v_c^* \end{bmatrix}, \quad (5.19)$$

where

$$T(z) = \frac{ZOH(z)K_{PI}(z)}{Z_{d_I}(z) + ZOH(z)K_{PI}(z)} \quad (5.20)$$

is the complementary sensitivity function which represents the ability of the velocity loop to track commands and

$$Z_{d_s}(z) = Z_{d_t}(z) + K_{PI}(z)ZOH(z), \quad (5.21)$$

is the driving-point impedance of the admittance display at the human operator port.

We can now make a very important observation. The network representation of the admittance display, (5.19), has a dual relationship to the network form of the impedance display, (5.5). Forces map to velocities, velocities map to forces, impedance functions map to admittance functions, and force transfer functions map to velocity transfer functions. This duality is useful when considering system stability and the design of virtual coupling networks.

### 5.2.1 Conventional Design

A simple admittance/admittance causality structure can be implemented without a virtual coupling by setting  $v_c^* = v_e^*$  and  $f_c^* = f_e^*$ . Is the resulting two-port passive? For this system, it is convenient to use the alternate hybrid matrix to check for absolute stability (5.19). The result is,

$$\frac{\operatorname{Re}(T(z))}{|T(z)|} \geq 1 \Leftrightarrow \cos(\angle T(z)) \geq 1. \quad (5.22)$$

Since  $\cos(\angle T(z)) < 1$  for any amount of lead or lag between the commanded and realized velocity, the admittance display is never absolutely stable.

### 5.2.2 Proposed Design Procedure

Our goal is to design a virtual coupling network such that the combined haptic interface network with an admittance display is absolutely stable. Fig. 5.6 shows the combined system.

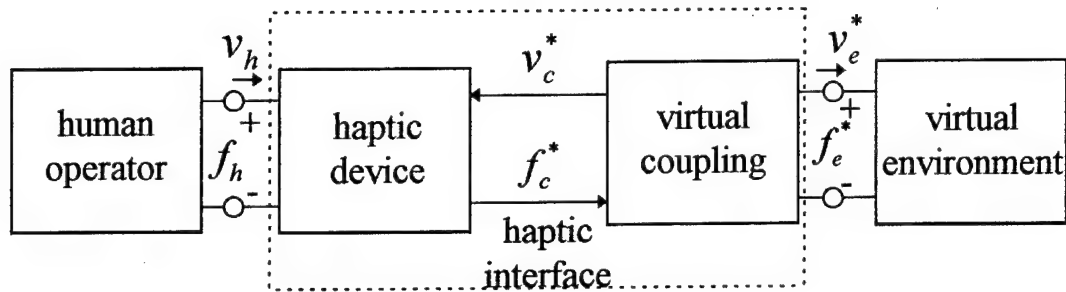


Fig. 5.6. Haptic Simulation with Admittance Display

The choice of a virtual coupling function is not intuitive in this case. We know that in a network sense, the admittance display is the dual of the impedance display. It follows that the coupling for the admittance display should be the dual of the impedance display virtual coupling network. The mechanical dual of the parallel spring-damper in Fig. 5.4 is a series mass-damper combination. Fig. 5.7 shows a free-body-diagram of this coupling scheme.

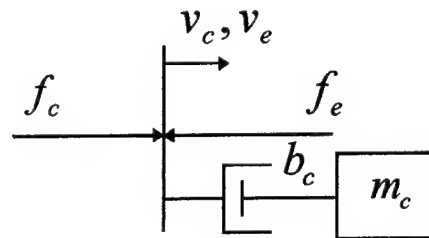


Fig. 5.7. Mechanical Analog of Mass-Damper Virtual Coupling

In this case, the virtual coupling aims to provide some minimum level of impedance for the virtual environment. It limits the degree to which the haptic interface can simulate free motion. The chosen coupling can be thought of as a frequency-dependent damper. It has zero steady-state resistance. At high-frequencies, the impedance of the mass becomes dominant, creating an effective damping of  $b_c$ . The admittance function of the virtual coupling is

$$Y_{c_A}(z) = \left( \frac{1}{b_c} + \frac{1}{m_c s} \right) \Bigg|_{s \rightarrow \left( \frac{z-1}{Tz} \right)} \quad (5.23)$$

The corresponding impedance function is  $Z_{c_A}(z) = 1/Y_{c_A}(z)$ . With the coupling in place, the human operator will always feel some level of viscosity and inertia in the haptic interface, even when the virtual environment simulates free motion. The best stability/performance trade-off is achieved when coupling impedance is set to the minimum level which makes the combined two-port absolutely stable.

The alternate hybrid form of the virtual coupling network is,

$$\begin{bmatrix} v_c^* \\ f_e^* \end{bmatrix} = \begin{bmatrix} 0 & -1 \\ 1 & Z_{c_A}(z) \end{bmatrix} \begin{bmatrix} f_c^* \\ -v_e^* \end{bmatrix} \quad (5.24)$$

The alternate hybrid mapping for the combined haptic interface network then becomes,

$$\begin{bmatrix} v_h \\ f_e^* \end{bmatrix} = \begin{bmatrix} \frac{1}{Z_{d_A}(z)} & -T(z) \\ 1 & Z_{c_A}(z) \end{bmatrix} \begin{bmatrix} f_h \\ -v_e^* \end{bmatrix} \quad (5.25)$$

With the virtual coupling in place, only the lower-right term has changed in the alternate hybrid matrix from (5.19) to (5.25). For absolute stability, the necessary and sufficient conditions are

$$\operatorname{Re}(Z_{c_A}(z)) \geq 0, \operatorname{Re}(1/Z_{d_A}(z)) \geq 0, \quad (5.26)$$

and

$$\cos(\angle T(z)) + \frac{2 \operatorname{Re}(Z_{c_A}(z)) \operatorname{Re}(1/Z_{d_A}(z))}{|T(z)|} \geq 1. \quad (5.27)$$

We can make the following observations about (5.26) and (5.27),

- $\operatorname{Re}(Z_{c_A}(z))$  can be interpreted as the damping of the virtual coupling. It must be non-zero and positive for absolute stability to be possible. This damping is what the human operator feels when the virtual environment simulates free motion.

- $\text{Re}(1/Z_{d_A}(z))$  can be interpreted as the conductance of the admittance display. This function dictates the amount of “give” the human operator perceives in the haptic display when the virtual environment simulates a rigid constraint. Some minimum positive value is necessary to achieve absolute stability. The need for compliance in an admittance implementation was previously observed by Kazerooni in his work on man-extendors [55].
- Larger values of  $\text{Re}(1/Z_{d_A}(z))$  permit smaller values of  $\text{Re}(Z_{c_A}(z))$ . This means that reducing the inner loop gains,  $K_{PI}(z)$ , improves the ability of the haptic interface to simulate free motion. At the same time, high values of  $K_{PI}(z)$  are desirable to simulate rigid constraints. The inner loop control must be chosen to strike a trade-off between these conflicting requirements.

Manipulating (5.27) gives us the following condition for absolute stability.

$$\text{Re}(Z_{c_A}(z)) \geq \frac{1 - \cos(\angle T(z))}{2 \text{Re}(1/Z_{d_A}(z))} |T(z)| \quad (5.28)$$

A design procedure for the virtual coupling network is to plot the right-hand side of (5.28) versus frequency, then synthesize  $Z_{c_A}(z)$  so that its real part is positive and exceeds this lower-bound.

As before, absolute stability is satisfied as long as (5.28) holds, regardless of whether an impedance or admittance type environment is used. The alternate hybrid mapping of the virtual coupling network, (5.24), links the haptic display to an admittance environment. For an impedance environment, the virtual coupling is implemented as

$$\begin{bmatrix} v_c^* \\ -v_e^* \end{bmatrix} = \begin{bmatrix} Y_{c_A}(z) & -Y_{c_A}(z) \\ -Y_{c_A}(z) & Y_{c_A}(z) \end{bmatrix} \begin{bmatrix} f_c^* \\ f_e^* \end{bmatrix} \quad (5.29)$$

The alternate hybrid matrix of the combined haptic interface network, (5.25), shows that to maximize transparency,  $Z_{c_A}(z)$  should be as small as possible. In other words, for performance, we want low virtual damping. The best virtual coupling network is one that minimally exceeds the lower-bound for absolute stability. The performance of the admittance implementation can be analyzed by terminating the virtual environment port of (5.25) with  $v_e^* = Y_e f_e^*$ . The resulting one-port function,  $Y_P$ ,

$$Y_P = \frac{v_h}{f_h} = 1/Z_{d_A}(z) + \frac{T(z)Y_e}{1 + Z_{c_A}(z)Y_e}, \quad (5.30)$$

represents the admittance perceived by the human operator for a given virtual environment. The minimum admittance which can be simulated by the haptic interface is found by letting  $Y_e \rightarrow 0$ .

$$Y_{\min_A} = 1/Z_{d_A}(z) \quad (5.31)$$

The maximum admittance is calculated by letting  $Y_e \rightarrow \infty$ .

$$Y_{\max_A} = 1/Z_{d_A}(z) + T(z)/Z_{c_A}(z) \quad (5.32)$$

The lower bound on  $Z$ -width is the inverse of maximum admittance.

$$Z_{\min_A} = \frac{Z_{c_A}(z)}{T(z) + Z_{c_A}(z)/Z_{d_A}(z)} \quad (5.33)$$

The upper bound on  $Z$ -width is the inverse of the minimum admittance function.

$$Z_{\max_A} = Z_{d_A}(z) = Z_{d_I}(z) + K_{PI}(z)ZOH(z) \quad (5.34)$$

We see that high gains in the velocity tracking control law,  $K_{PI}(z)$ , are needed to increase  $Z_{\max_A}$  and better simulate rigid constraints. We observed earlier that to achieve absolute stability and low impedance motion,  $K_{PI}(z)$  must be small. We are faced with a trade-off between performance when simulating free motion (small  $Z_{\min_A}$ , small  $K_{PI}(z)$ ) and performance when simulating rigid objects (large  $Z_{\max_A}$ , large  $K_{PI}(z)$ ).

### 5.3 Duality

The impedance display two-port network, (5.5), is the dual of the admittance display two-port, (5.19). Similarly, the virtual coupling networks, (5.8) and (5.24), are dual, and the combined haptic interface networks, (5.9) and (5.25), for the two cases are dual. The correspondence of parameters is shown in Table 5.1. The impedance matrix in one case is the dual mapping of the admittance matrix in the other, and the hybrid matrix is the dual mapping of the alternate hybrid matrix.

Table 5.1. Correspondence in Impedance/Admittance Display Duality

Impedance Display		Admittance Display
$Z_{d_I}(z)$	$\leftrightarrow$	$1/Z_{d_A}(z)$
$1/Z_{c_I}(z)$	$\leftrightarrow$	$Z_{c_A}(z)$
$ZOH(z)$	$\leftrightarrow$	$T(z)$

This strong relationship between the two cases provides a number of interesting insights into stability problems:

- We observed earlier that a minimum level of damping was needed in the impedance display to guarantee absolute stability. Duality maps this requirement to the need for a minimum level of conductance or “give” in the admittance display.

$$\operatorname{Re}(Z_{d_I}(z)) \geq 0 \leftrightarrow \operatorname{Re}(1/Z_{d_A}(z)) \geq 0 \quad (5.35)$$

- For the impedance display, we have seen that the virtual coupling must have a minimum level of conductance or “give” for the haptic interface to be absolute stable. Duality maps this requirement to the need for a minimum level of real impedance (damping) in the virtual coupling of the admittance display.

$$\operatorname{Re}(1/Z_{c_I}(z)) \geq 0 \leftrightarrow \operatorname{Re}(Z_{c_A}(z)) \geq 0 \quad (5.36)$$

- Worst case stability for the impedance implementation occurs when human operator impedance is low (loose grasp or hands-off) and virtual environment impedance is high (rigid constraint). Worst case stability for the admittance implementation occurs when human operator impedance is high (rigid grasp) and virtual environment impedance is low (free motion).

#### 5.4 Extensions

The benchmark example does not consider velocity estimation effects or structural flexibility in the haptic device. Following similar arguments, equivalent conditions to (5.12) and (5.28) can be derived which include these issues. These issues are addressed in the subsequent chapter. Adding complexity to the model does not change the fundamental relationships and tradeoffs described above. We have also limited the problem to a single degree-of-freedom device. This allows us to find necessary and sufficient conditions for absolute stability and develop explicit design criteria for virtual coupling networks.

Additional axes of motion can be handled with this approach if they are orthogonal or if they can be transformed into an orthogonal system. Otherwise, we must consider a  $2n$ -port representation of the haptic interface, instead of the two-port form used in this paper. A virtual coupling network may still be designed for individual axes using our approach, but post-design analysis using the methods described in [27] or [56] will be needed to guarantee absolute stability.



## Chapter 6

### Advanced Implementations

The simplicity of the benchmark example in the previous chapter permits a clear illustration of some of the fundamental issues in haptic interface design. Unfortunately, most devices are not as elementary as the basic mass-damper system. This chapter presents a more general formulation of the design of absolutely stable haptic interfaces. In particular, issues of velocity estimation and structural flexibility in the haptic device are addressed. Two-port absolute stability criteria are used to develop explicit control law design bounds for three different haptic display implementations: the basic impedance display, the impedance display with force compensation, and the admittance display.

#### 6.1 Device Model

The internal dynamics of a flexible mechanical device can be conveniently represented in second-order form,

$$M\ddot{q}(t) + D\dot{q}(t) + Kq(t) = Gu(t), \quad (6.1)$$

where  $M$ ,  $D$ , and  $K$  are the mass, damping, and stiffness matrices respectively.  $G$  is the control distribution matrix.  $q$  is a vector representing the internal state of the system and  $u$  is the input vector,

$$u(t) = [f_h(t) \quad f_a(t)]^T. \quad (6.2)$$

$f_h$  is the force applied at the handle by the human operator.  $f_a$  is the force generated by the actuator. We are interested in three outputs: velocity at the handle,  $v_h$ , velocity of the actuator,  $v_a$ , and strain gauge force,  $f_s$ .

$$\begin{bmatrix} v_h(t) \\ -v_a(t) \end{bmatrix} = C_v \dot{q}(t) \quad (6.3)$$

$$f_s(t) = C_f q(t) \quad (6.4)$$

The actual force measurement may include additional filtering for noise reduction and anti-aliasing,  $a(s)$ . The output of this filter is the measured force at the handle,  $f_m$ . The equations governing the dynamics of the system can be written in Laplace form,

$$\begin{bmatrix} v_h(s) \\ -v_a(s) \end{bmatrix} = C_v s(Ms^2 + Ds + K)^{-1} G \begin{bmatrix} f_h(s) \\ f_a(s) \end{bmatrix}, \quad (6.5)$$

$$f_m(s) = a(s)C_f(Ms^2 + Ds + K)^{-1} G \begin{bmatrix} f_h(s) \\ f_a(s) \end{bmatrix}. \quad (6.6)$$

The device equations of motion can alternatively be written in terms of individual transfer functions.

$$\begin{bmatrix} v_h(s) \\ -v_a(s) \end{bmatrix} = \begin{bmatrix} Y_{hh}(s) & Y_{ha}(s) \\ Y_{ah}(s) & Y_{aa}(s) \end{bmatrix} \begin{bmatrix} f_h(s) \\ f_a(s) \end{bmatrix} \quad (6.7)$$

$$f_m(s) = \begin{bmatrix} F_{mh}(s) & F_{ma}(s) \end{bmatrix} \begin{bmatrix} f_h(s) \\ f_a(s) \end{bmatrix} \quad (6.8)$$

Note that two subscripts are attached to each transfer function. The first one matches the subscript of the corresponding output variable. The second subscript matches that of the input variable.

## 6.2 Haptic Display Implementations

Within the individual classes of impedance and admittance type haptic displays, a number of implementations are possible. Three of the most common will be described here. It is straightforward to follow the examples below to perform design and analysis for other implementations.

### 6.2.1 Impedance Display - Basic

This is by far the most common implementation of a haptic display. Either optical encoders or potentiometers provide a measure of device position,  $x_a$ , at the point of actuation. This signal is sampled with period  $T$  to create the digital signal,  $x_a^*$ . The device velocity is estimated, most often using a simple first difference approximation, to generate

the output variable,  $v_c^*$ . The digital force command,  $f_c^*$ , is passed through a zero-order hold to provide the control input to the actuators. Fig. 6.1 shows the basic impedance display implementation.

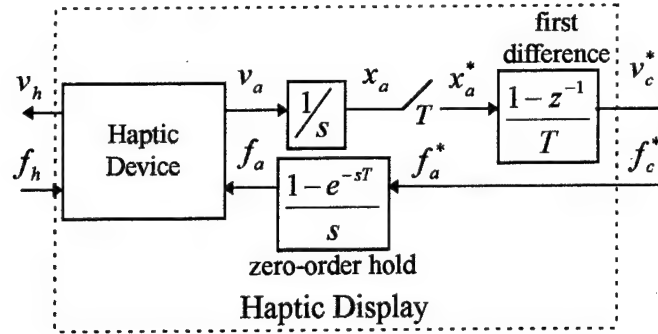


Fig. 6.1. Basic Impedance Display Implementation

The two-port equations for the haptic display can be derived from Fig. 6.1 and the haptic device two-port admittance form, (6.7). Including the integration of device velocity and the zero-order hold at the input, we have,

$$\begin{bmatrix} v_h(s) \\ -x_a(s) \end{bmatrix} = \begin{bmatrix} Y_{hh}(s) & Y_{ha}(s) \left( \frac{1-e^{-sT}}{s} \right) \\ Y_{ah}(s) \left( \frac{1}{s} \right) & Y_{aa}(s) \left( \frac{1-e^{-sT}}{s^2} \right) \end{bmatrix} \begin{bmatrix} f_h(s) \\ f_a^*(s) \end{bmatrix}. \quad (6.9)$$

The Laplace transform of the digital signal  $x_a^*$  is

$$x_a^*(s) = \frac{1}{T} \sum_{k=-\infty}^{\infty} x_a(s + j\omega_s k), \quad \omega_s = 2\pi / T. \quad (6.10)$$

If we can assume that  $x_a(j\omega)$  is zero for  $|\omega| \geq \pi/T$ , then no aliasing will take place when the signal is sampled. This is a normally a reasonable assumption thanks to the low pass properties of the lower two transfer functions in (6.9). We can therefore say

$$x_a^*(s) = \frac{1}{T} x_a(s) \quad \forall \quad 0 \leq \omega \leq \pi/T. \quad (6.11)$$

Applying (6.11) to (6.9) gives us,

$$\begin{aligned}
 \begin{bmatrix} v_h(s) \\ -x_a^*(s) \end{bmatrix} &= \begin{bmatrix} Y_{hh}(s) & Y_{ha}(s) \left( \frac{1-e^{-sT}}{s} \right) \\ \frac{1}{T} Y_{ah}(s) \left( \frac{1}{s} \right) & \frac{1}{T} Y_{aa}(s) \left( \frac{1-e^{-sT}}{s^2} \right) \end{bmatrix} \begin{bmatrix} f_h(s) \\ f_a^*(s) \end{bmatrix} \\
 &= \begin{bmatrix} Y_{hh}(s) & Y_{ha}^*(s) \\ X_{ah}^*(s) & X_{aa}^*(s) \end{bmatrix} \begin{bmatrix} f_h(s) \\ f_a^*(s) \end{bmatrix}. \tag{6.12}
 \end{aligned}$$

The final step is to include the first difference velocity approximation, giving us the equations for the basic impedance type haptic display (in admittance matrix form),

$$\begin{aligned}
 \begin{bmatrix} v_h(s) \\ -v_c^*(s) \end{bmatrix} &= \begin{bmatrix} Y_{hh}(s) & Y_{ha}^*(s) \\ \frac{1}{T}(1-e^{-sT})X_{ah}^*(s) & \frac{1}{T}(1-e^{-sT})X_{aa}^*(s) \end{bmatrix} \begin{bmatrix} f_h(s) \\ f_c^*(s) \end{bmatrix} \\
 &= \begin{bmatrix} Y_{hh}(s) & Y_{hc}^*(s) \\ Y_{ch}^*(s) & Y_{cc}^*(s) \end{bmatrix} \begin{bmatrix} f_h(s) \\ f_c^*(s) \end{bmatrix}. \tag{6.13}
 \end{aligned}$$

This is an effective implementation. Equivalent strategies have been used by numerous researchers [10], [12], [17], [31]. One disadvantage of this approach is that no compensation is made for the open loop impedance of the device. In other words, when moving about in free motion, the human operator will always ‘feel’ the full inertia and friction of the manipulator. For lightweight, highly backdrivable devices, this is acceptable. When device inertia and friction are significant, an alternative implementation is desirable.

### 6.2.2 Impedance Display - with Force Compensation

When force sensing is available, an alternative impedance display implementation can be created using a force tracking loop. This approach, illustrated in Fig. 6.2, attempts to reduce the apparent impedance at the handle by feeding back the difference between the commanded and the measured force. When the commanded force is zero, the operator ‘feels’ less friction and inertia than with the basic impedance display.

$$\begin{aligned}
 \begin{bmatrix} v_h(s) \\ -v_c^*(s) \end{bmatrix} &= \begin{bmatrix} Y_{hh}(s) - \frac{Y_{ha}^*(s)K_f(e^{sT})F_{mh}^*(s)}{1+F_{ma}^*(s)K_f(e^{sT})} & \frac{Y_{ha}^*(s)K_f(e^{sT})}{1+F_{ma}^*(s)K_f(e^{sT})} \\ \left(\frac{1-e^{-sT}}{T}\right)\left(Y_{21}^*(s) - \frac{X_{aa}^*(s)K_f(e^{sT})F_{mh}^*(s)}{1+F_{ma}^*(s)K_f(e^{sT})}\right) & \left(\frac{1-e^{-sT}}{T}\right)\frac{X_{aa}^*(s)K_f(e^{sT})}{1+F_{ma}^*(s)K_f(e^{sT})} \end{bmatrix} \begin{bmatrix} f_h(s) \\ f_c^*(s) \end{bmatrix} \\
 &= \begin{bmatrix} Y_{hh-f}^*(s) & Y_{hc-f}^*(s) \\ Y_{ch-f}^*(s) & Y_{cc-f}^*(s) \end{bmatrix} \begin{bmatrix} f_h(s) \\ f_c^*(s) \end{bmatrix}. \quad (6.17)
 \end{aligned}$$

To optimize the free-motion response of the haptic display, we would like the force regulator gain to be as large as possible.

### 6.2.3 Admittance Display

The presence of high levels of inertia and friction, common in industrial robots, may make a basic impedance display implementation impractical. Stability concerns often limit the degree to which strain gauge feedback can improve performance in an impedance display with force compensation. Another option is to configure the device as an admittance display. This implementation has been used in a number of applications where back-drivability is a concern [50], [51]. Fig. 6.3 shows a block diagram of an admittance display.

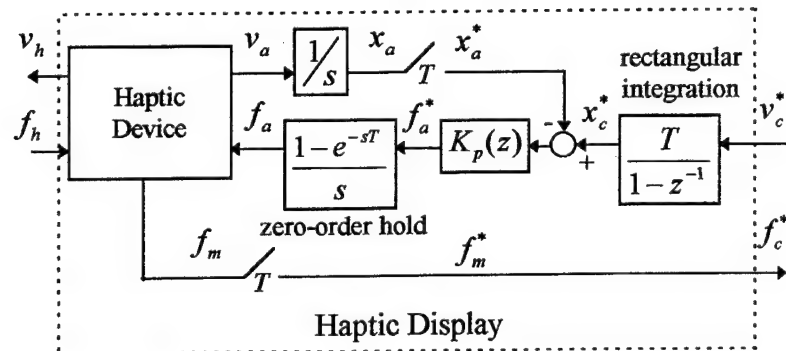


Fig. 6.3. Admittance Display Implementation

$$\begin{aligned}
\begin{bmatrix} v_h(s) \\ -v_c^*(s) \end{bmatrix} &= \begin{bmatrix} Y_{hh}(s) - \frac{Y_{ha}^*(s)K_f(e^{sT})F_{mh}^*(s)}{1+F_{ma}^*(s)K_f(e^{sT})} & \frac{Y_{ha}^*(s)K_f(e^{sT})}{1+F_{ma}^*(s)K_f(e^{sT})} \\ \left(\frac{1-e^{-sT}}{T}\right)\left(Y_{21}^*(s) - \frac{X_{aa}^*(s)K_f(e^{sT})F_{mh}^*(s)}{1+F_{ma}^*(s)K_f(e^{sT})}\right) & \left(\frac{1-e^{-sT}}{T}\right)\frac{X_{aa}^*(s)K_f(e^{sT})}{1+F_{ma}^*(s)K_f(e^{sT})} \end{bmatrix} \begin{bmatrix} f_h(s) \\ f_c^*(s) \end{bmatrix} \\
&= \begin{bmatrix} Y_{hh-f}^*(s) & Y_{hc-f}^*(s) \\ Y_{ch-f}^*(s) & Y_{cc-f}^*(s) \end{bmatrix} \begin{bmatrix} f_h(s) \\ f_c^*(s) \end{bmatrix}. \tag{6.17}
\end{aligned}$$

To optimize the free-motion response of the haptic display, we would like the force regulator gain to be as large as possible.

### 6.2.3 Admittance Display

The presence of high levels of inertia and friction, common in industrial robots, may make a basic impedance display implementation impractical. Stability concerns often limit the degree to which strain gauge feedback can improve performance in an impedance display with force compensation. Another option is to configure the device as an admittance display. This implementation has been used in a number of applications where back-drivability is a concern [50], [51]. Fig. 6.3 shows a block diagram of an admittance display.

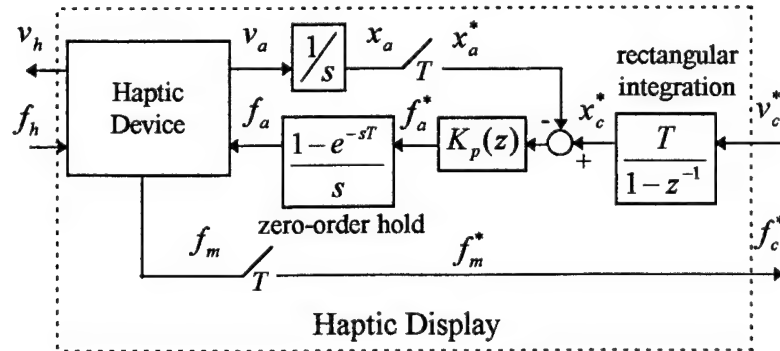


Fig. 6.3. Admittance Display Implementation

For admittance displays, we will limit the virtual coupling two-port to consist of a single series impedance,

$$Z_{c_A}(z) = \frac{m_{c_A} b_{c_A} (z-1)}{(m_{c_A} + b_{c_A} T)z - 1}. \quad (6.21)$$

While the virtual environment may simulate an infinitesimally small mass, there is a limit to what the haptic display can stably render. The admittance display virtual coupling acts as a frequency-dependent damper, providing the required level of impedance to guarantee that the system remains stable. For performance, we would like  $Z_{c_A}(z)$  to be as small as possible, permitting unconstrained free motion, while still meeting the requirements for absolute stability.

The actual implementation of the virtual coupling networks is dictated by the type of haptic display and virtual environment used in a simulation. At one end, the virtual coupling two-port must match the causality of the haptic display. If an impedance display is used, the coupling must accept velocities,  $v_e^*$ , and generate forces,  $f_e^*$ . The inverse is true if the coupling is connected to an admittance display. On the other end the virtual coupling two-port must match the causality of the virtual environment. It is possible for a virtual environment to act as an impedance,  $f_e^* = Z_e v_e^*$ , or as an admittance,  $v_e^* = Z_e f_e^*$ . The four possible virtual coupling implementations are shown in Table 6.1.

For admittance displays, we will limit the virtual coupling two-port to consist of a single series impedance,

$$Z_{c_A}(z) = \frac{m_{c_A} b_{c_A} (z - 1)}{(m_{c_A} + b_{c_A} T)z - 1}. \quad (6.21)$$

While the virtual environment may simulate an infinitesimally small mass, there is a limit to what the haptic display can stably render. The admittance display virtual coupling acts as a frequency-dependent damper, providing the required level of impedance to guarantee that the system remains stable. For performance, we would like  $Z_{c_A}(z)$  to be as small as possible, permitting unconstrained free motion, while still meeting the requirements for absolute stability.

The actual implementation of the virtual coupling networks is dictated by the type of haptic display and virtual environment used in a simulation. At one end, the virtual coupling two-port must match the causality of the haptic display. If an impedance display is used, the coupling must accept velocities,  $v_e^*$ , and generate forces,  $f_e^*$ . The inverse is true if the coupling is connected to an admittance display. On the other end the virtual coupling two-port must match the causality of the virtual environment. It is possible for a virtual environment to act as an impedance,  $f_e^* = Z_e v_e^*$ , or as an admittance,  $v_e^* = Z_e f_e^*$ . The four possible virtual coupling implementations are shown in Table 6.1.



Note that (6.22) is invariant to the choice of virtual environment causality and thus so are the analysis and design results which follow. The difference lies only in the implementation of the virtual coupling. By applying (3.6) to (6.22), we get the conditions for absolute stability of the haptic interface,

$$\operatorname{Re}(Y_{hh}(s)) \geq 0 \quad (6.23)$$

$$2\operatorname{Re}(Y_{hh}^*(s))\operatorname{Re}(Y_{cc}^*(s) + 1/Z_{c_I}(e^{sT})) \geq |Y_{hc}^*(s)Y_{ch}^*(s)| + \operatorname{Re}(Y_{hc}^*(s)Y_{ch}^*(s)). \quad (6.24)$$

By definition,  $Y_{hh}(s)$  is the transfer function from force applied at the handle to velocity at the handle when the force of actuation is zero. Since the unpowered mechanical device is inherently passive, this open loop admittance function will always be positive real and thus (6.23) is satisfied without further consideration. The inequality (6.24) can be rewritten to get an explicit expression which separates the unknown quantities (virtual coupling impedance) from known quantities (haptic display two-port parameters).

$$\operatorname{Re}(1/Z_{c_I}(e^{sT})) \geq \frac{|Y_{hc}^*(s)Y_{ch}^*(s)| + \operatorname{Re}(Y_{hc}^*(s)Y_{ch}^*(s))}{2\operatorname{Re}(Y_{hh}(s))} - \operatorname{Re}(Y_{cc}^*(s)) \quad (6.25)$$

This is the virtual coupling design equation. The right hand side is a real valued function which can be plotted against frequency for  $0 \leq \omega \leq \pi/T$ . To achieve an absolutely stable haptic interface, we must choose the virtual coupling such that the real part of its admittance function exceeds the lower bound formed by this plot. To maximize performance, we want to maximize virtual coupling impedance. The optimum solution is achieved by selecting the spring constant,  $k_{c_I}$ , and damping,  $b_{c_I}$ , which minimize the difference between the left and right hand side of (6.25) under the constraint that the inequality is satisfied. These values can be found by performing a rapid two-dimensional numerical search.

#### 6.4.2 Impedance Display - with Force Compensation

The haptic interface equations in this case are identical to those in the previous one, substituting the terms in (6.17) for those in (6.13). The conditions for absolute stability are,

Note that (6.22) is invariant to the choice of virtual environment causality and thus so are the analysis and design results which follow. The difference lies only in the implementation of the virtual coupling. By applying (3.6) to (6.22), we get the conditions for absolute stability of the haptic interface,

$$\operatorname{Re}(Y_{hh}(s)) \geq 0 \quad (6.23)$$

$$2\operatorname{Re}(Y_{hh}^*(s))\operatorname{Re}(Y_{cc}^*(s) + 1/Z_{c_i}(e^{sT})) \geq |Y_{hc}^*(s)Y_{ch}^*(s)| + \operatorname{Re}(Y_{hc}^*(s)Y_{ch}^*(s)). \quad (6.24)$$

By definition,  $Y_{hh}(s)$  is the transfer function from force applied at the handle to velocity at the handle when the force of actuation is zero. Since the unpowered mechanical device is inherently passive, this open loop admittance function will always be positive real and thus (6.23) is satisfied without further consideration. The inequality (6.24) can be rewritten to get an explicit expression which separates the unknown quantities (virtual coupling impedance) from known quantities (haptic display two-port parameters).

$$\operatorname{Re}(1/Z_{c_i}(e^{sT})) \geq \frac{|Y_{hc}^*(s)Y_{ch}^*(s)| + \operatorname{Re}(Y_{hc}^*(s)Y_{ch}^*(s))}{2\operatorname{Re}(Y_{hh}(s))} - \operatorname{Re}(Y_{cc}^*(s)) \quad (6.25)$$

This is the virtual coupling design equation. The right hand side is a real valued function which can be plotted against frequency for  $0 \leq \omega \leq \pi/T$ . To achieve an absolutely stable haptic interface, we must choose the virtual coupling such that the real part of its admittance function exceeds the lower bound formed by this plot. To maximize performance, we want to maximize virtual coupling impedance. The optimum solution is achieved by selecting the spring constant,  $k_{c_i}$ , and damping,  $b_{c_i}$ , which minimize the difference between the left and right hand side of (6.25) under the constraint that the inequality is satisfied. These values can be found by performing a rapid two-dimensional numerical search.

#### 6.4.2 Impedance Display - with Force Compensation

The haptic interface equations in this case are identical to those in the previous one, substituting the terms in (6.17) for those in (6.13). The conditions for absolute stability are,

Let us create a (fictitious) admittance matrix,

$$Y_{fict} = \left[ \begin{array}{c|c} Y_{hh}(s) & Y_{ha}^*(s) \\ \hline F_{mh}^*(s) & F_{ma}^*(s) + \frac{1}{K_f(e^{sT})} \end{array} \right] \quad (6.28)$$

The two conditions for the absolute stability of (6.28) are,

$$\operatorname{Re}(Y_{hh}(s)) \geq 0 \quad (6.29)$$

$$\operatorname{Re}(1/K_f(e^{sT})) \geq \frac{|Y_{ha}^*(s)F_{mh}^*(s)| + \operatorname{Re}(Y_{ha}^*(s)F_{mh}^*(s))}{2\operatorname{Re}(Y_{hh}^*(s))} - \operatorname{Re}(F_{ma}^*(s)). \quad (6.30)$$

As discussed earlier, the open loop device admittance at the handle is always passive, so (6.29) is satisfied. Therefore, (6.30) is necessary and sufficient for the absolute stability of the alternate hybrid matrix derived from (6.28) using Table 3.4, (we are only interested in the upper left term).

$$G_{fict} = \left[ \begin{array}{c|c} Y_{hh}(s) - \frac{Y_{ha}^*(s)K_f(e^{sT})F_{mh}^*(s)}{1 + F_{ma}^*(s)K_f(e^{sT})} & - \\ \hline - & - \end{array} \right] \quad (6.31)$$

We recognize the upper left term of (6.31) to be  $Y_{hh-f}^*(s)$  from (6.17). This term must be positive real if  $G_{fict}$  is absolutely stable. The right side of (6.30) is a known real function which can be plotted against frequency. Although (6.30) is a sufficient, but not a necessary condition for the satisfaction of (6.26), practice has shown that it provides a tight fit and gives us an explicit design bound for the force regulator.

- The second step is to choose the virtual coupling impedance function,  $Z_{c_i}(e^{sT})$ , such that (6.27) is satisfied.

Just as in the basic impedance case, we must choose a spring constant,  $k_{c_i}$ , and damping,  $b_{c_i}$ , which maximize virtual coupling impedance while satisfying (6.27).

Let us create a (fictitious) admittance matrix,

$$Y_{fict} = \left[ \begin{array}{c|c} Y_{hh}(s) & Y_{ha}^*(s) \\ \hline F_{mh}^*(s) & F_{ma}^*(s) + \frac{1}{K_f(e^{sT})} \end{array} \right] \quad (6.28)$$

The two conditions for the absolute stability of (6.28) are,

$$\operatorname{Re}(Y_{hh}(s)) \geq 0 \quad (6.29)$$

$$\operatorname{Re}(1/K_f(e^{sT})) \geq \frac{|Y_{ha}^*(s)F_{mh}^*(s)| + \operatorname{Re}(Y_{ha}^*(s)F_{mh}^*(s))}{2\operatorname{Re}(Y_{hh}^*(s))} - \operatorname{Re}(F_{ma}^*(s)). \quad (6.30)$$

As discussed earlier, the open loop device admittance at the handle is always passive, so (6.29) is satisfied. Therefore, (6.30) is necessary and sufficient for the absolute stability of the alternate hybrid matrix derived from (6.28) using Table 3.4, (we are only interested in the upper left term).

$$G_{fict} = \left[ \begin{array}{c|c} Y_{hh}(s) - \frac{Y_{ha}^*(s)K_f(e^{sT})F_{mh}^*(s)}{1 + F_{ma}^*(s)K_f(e^{sT})} & - \\ \hline - & - \end{array} \right] \quad (6.31)$$

We recognize the upper left term of (6.31) to be  $Y_{hh-f}^*(s)$  from (6.17). This term must be positive real if  $G_{fict}$  is absolutely stable. The right side of (6.30) is a known real function which can be plotted against frequency. Although (6.30) is a sufficient, but not a necessary condition for the satisfaction of (6.26), practice has shown that it provides a tight fit and gives us an explicit design bound for the force regulator.

- The second step is to choose the virtual coupling impedance function,  $Z_{c_f}(e^{sT})$ , such that (6.27) is satisfied.

Just as in the basic impedance case, we must choose a spring constant,  $k_{c_f}$ , and damping,  $b_{c_f}$ , which maximize virtual coupling impedance while satisfying (6.27).

$$K_p(e^{sT}) = \frac{1}{T}(1 - e^{-sT})Z_{c_i}(e^{sT}) = k_{c_i} + b_{c_i} \frac{1}{T}(1 - e^{-sT}), \quad (6.36)$$

which is guaranteed to satisfy (6.33).

- Second, the admittance display virtual coupling function,  $Z_{c_A}(z)$ , is chosen to satisfy (6.34).

This entails plotting the right side of (6.34) and choosing  $m_{c_A}$  and  $b_{c_A}$  such that the graph of the left side exceeds that curve for all frequencies,  $0 \leq \omega \leq \pi/T$ . For optimal performance in this case, we want to minimize the impedance of the virtual coupling. The parameters are selected to minimize the difference between the left and right sides of (6.34) under the constrain that the inequality is satisfied.

#### 6.4.4 Impact of Human Model on Stability Conditions

A limit on the maximum human operator impedance, as described in Section 4.1, may be included in the stability analysis by simply substituting,

$$Y_{hh}(s) \rightarrow Y_{hh}(s) + 1/Z_{\max}(s) \quad (6.37)$$

in all of the preceding equations.

#### 6.5 Performance

The impedance range of a haptic interface is delineated by the minimum ( $Z_{\min}$ ) and maximum ( $Z_{\max}$ ) impedance which it can *stably* render to the human operator. If the haptic interface is absolutely stable, then it is straightforward to calculate these bounds on realizable impedance. The minimum impedance is simply the input impedance at the human operator port with the virtual environment port short-circuited.

$$Z_{\min}(s) = \left. \frac{f_h(s)}{v_h(s)} \right|_{f_e^*(s) \rightarrow 0} \quad (6.38)$$

The maximum impedance is found with an open-circuit virtual environment.

$$K_p(e^{sT}) = \frac{1}{T}(1 - e^{-sT})Z_{c_i}(e^{sT}) = k_{c_i} + b_{c_i} \frac{1}{T}(1 - e^{-sT}), \quad (6.36)$$

which is guaranteed to satisfy (6.33).

- Second, the admittance display virtual coupling function,  $Z_{c_A}(z)$ , is chosen to satisfy (6.34).

This entails plotting the right side of (6.34) and choosing  $m_{c_A}$  and  $b_{c_A}$  such that the graph of the left side exceeds that curve for all frequencies,  $0 \leq \omega \leq \pi/T$ . For optimal performance in this case, we want to minimize the impedance of the virtual coupling. The parameters are selected to minimize the difference between the left and right sides of (6.34) under the constrain that the inequality is satisfied.

#### 6.4.4 Impact of Human Model on Stability Conditions

A limit on the maximum human operator impedance, as described in Section 4.1, may be included in the stability analysis by simply substituting,

$$Y_{hh}(s) \rightarrow Y_{hh}(s) + 1/Z_{\max}(s) \quad (6.37)$$

in all of the preceding equations.

#### 6.5 Performance

The impedance range of a haptic interface is delineated by the minimum ( $Z_{\min}$ ) and maximum ( $Z_{\max}$ ) impedance which it can *stably* render to the human operator. If the haptic interface is absolutely stable, then it is straightforward to calculate these bounds on realizable impedance. The minimum impedance is simply the input impedance at the human operator port with the virtual environment port short-circuited.

$$Z_{\min}(s) = \left. \frac{f_h(s)}{v_h(s)} \right|_{f_e^*(s) \rightarrow 0} \quad (6.38)$$

The maximum impedance is found with an open-circuit virtual environment.

## Chapter 7

### Design and Experimental Results for the High-Bandwidth Force Display

The High-Bandwidth Force Display (HBFD), is a two degree-of-freedom, planar, haptic display with Cartesian kinematics [18]. A large workspace of  $300 \times 400 \text{ mm}^2$  and a high force output of  $100 \text{ N}$  (peak to  $400 \text{ N}$ ), make the device well suited for full arm manipulation in virtual environments. A 266 MHz Pentium II™ PC provides computational power for the HBFD with interrupt level software running at  $1000 \text{ Hz}$  ( $T = 1.0 \text{ ms}$ ). Incremental encoders are located on the motors and provide  $0.015 \text{ mm}$  spatial resolution. Force is measured by a strain gauge bridge built into the handle which provides a maximum  $0.05 \text{ N}$  resolution. Details on the mechanical design and development of HBFD hardware can be found in [58]. The device is shown in Fig. 7.1.

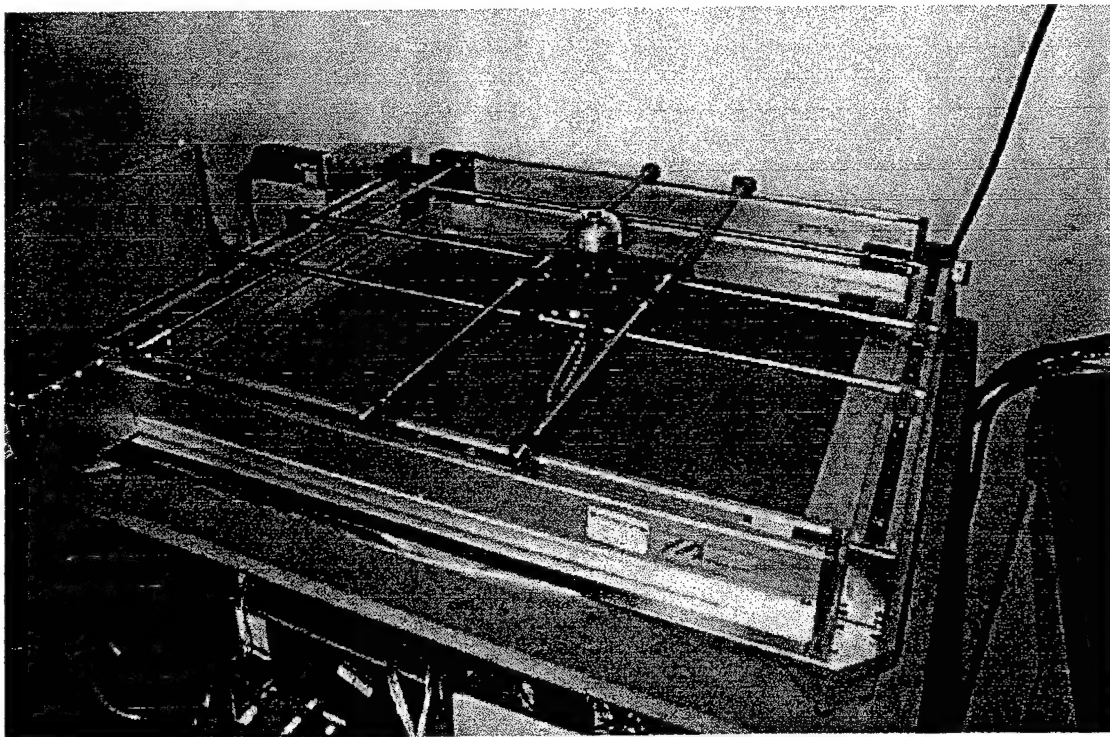


Fig. 7.1. HBFD Hardware

## Chapter 7

### Design and Experimental Results for the High-Bandwidth Force Display

The High-Bandwidth Force Display (HBFD), is a two degree-of-freedom, planar, haptic display with Cartesian kinematics [18]. A large workspace of  $300 \times 400 \text{ mm}^2$  and a high force output of  $100 \text{ N}$  (peak to  $400 \text{ N}$ ), make the device well suited for full arm manipulation in virtual environments. A 266 MHz Pentium II™ PC provides computational power for the HBFD with interrupt level software running at  $1000 \text{ Hz}$  ( $T = 1.0 \text{ ms}$ ). Incremental encoders are located on the motors and provide  $0.015 \text{ mm}$  spatial resolution. Force is measured by a strain gauge bridge built into the handle which provides a maximum  $0.05 \text{ N}$  resolution. Details on the mechanical design and development of HBFD hardware can be found in [58]. The device is shown in Fig. 7.1.

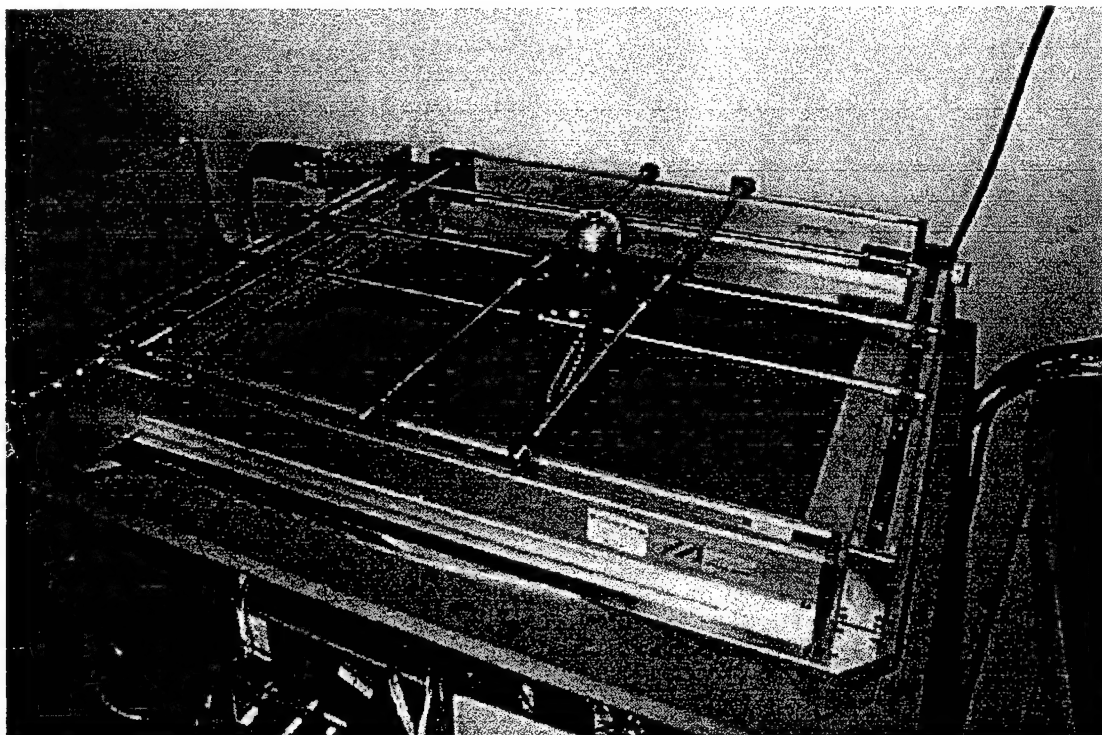


Fig. 7.1. HBFD Hardware



A nominal set of masses which adequately characterize the behavior of the HBFD is  $m_1=0.2$  kg,  $m_2=2.3$  kg,  $m_3=2.0$  kg, and  $m_4=0.5$  kg. The flexibility of the manipulator varies with the location of the stage. The worst-case configuration, where resonant frequencies are the lowest, occurs when the handle is centered between the two stops. The corresponding stiffness values are  $k_1=130$  kN/m,  $k_2=84$  kN/m, and  $k_3=874$  kN/m. Accurately determining damping parameters is difficult, since both viscous and Coulomb friction are present. A damping ratio of 0.01 is assumed in the flexible elements. The resulting parameters are,

$$b_i = 0.1 \times 2 \sqrt{k_i m_i m_{i+1} / (m_i + m_{i+1})}, \quad i = 1, 2, 3. \quad (7.4)$$

The chosen value for rigid body damping,  $b_4=5.0$  N/(m/s), while only an approximation, does a reasonable job of representing the behavior of the device.

Using these values and (6.5)-(6.8), the admittance matrix parameters can be formed ( $Y_{hh}(s)$ ,  $Y_{ah}(s)$ ,  $Y_{ha}(s)$ ,  $Y_{aa}(s)$ ) along with the force output transfer functions ( $F_{mh}(s)$ ,  $F_{ma}(s)$ ).

## 7.2 Design for Absolute Stability

Because it is both back-drivable and equipped with a force sensor, the HBFD can be configured to operate as either an impedance or an admittance type haptic display. The friction and inertia of the device fall between the low typical values for impedance displays such as a PHANTOM, and the high typical values for admittance displays such as PUMA based implementations. In the following, virtual coupling networks are designed for a basic impedance display and an admittance display implementation.

### 7.2.1 Impedance Display - Basic

The basic impedance display, shown in Fig. 6.1, is constructed from the two-port admittance form using (6.12)-(6.13). A virtual coupling of the form (6.20) which guarantees absolute stability of the resulting haptic interface can be found using (6.25). The right side of this inequality is plotted against frequency and shown in Fig. 7.3 as a

A nominal set of masses which adequately characterize the behavior of the HBFD is  $m_1=0.2$  kg,  $m_2=2.3$  kg,  $m_3=2.0$  kg, and  $m_4=0.5$  kg. The flexibility of the manipulator varies with the location of the stage. The worst-case configuration, where resonant frequencies are the lowest, occurs when the handle is centered between the two stops. The corresponding stiffness values are  $k_1=130$  kN/m,  $k_2=84$  kN/m, and  $k_3=874$  kN/m. Accurately determining damping parameters is difficult, since both viscous and Coulomb friction are present. A damping ratio of 0.01 is assumed in the flexible elements. The resulting parameters are,

$$b_i = 0.1 \times 2\sqrt{k_i m_i m_{i+1} / (m_i + m_{i+1})}, \quad i=1,2,3. \quad (7.4)$$

The chosen value for rigid body damping,  $b_4=5.0$  N/(m/s), while only an approximation, does a reasonable job of representing the behavior of the device.

Using these values and (6.5)-(6.8), the admittance matrix parameters can be formed ( $Y_{hh}(s)$ ,  $Y_{ah}(s)$ ,  $Y_{ha}(s)$ ,  $Y_{aa}(s)$ ) along with the force output transfer functions ( $F_{mh}(s)$ ,  $F_{ma}(s)$ ).

## 7.2 Design for Absolute Stability

Because it is both back-drivable and equipped with a force sensor, the HBFD can be configured to operate as either an impedance or an admittance type haptic display. The friction and inertia of the device fall between the low typical values for impedance displays such as a PHANTOM, and the high typical values for admittance displays such as PUMA based implementations. In the following, virtual coupling networks are designed for a basic impedance display and an admittance display implementation.

### 7.2.1 Impedance Display - Basic

The basic impedance display, shown in Fig. 6.1, is constructed from the two-port admittance form using (6.12)-(6.13). A virtual coupling of the form (6.20) which guarantees absolute stability of the resulting haptic interface can be found using (6.25). The right side of this inequality is plotted against frequency and shown in Fig. 7.3 as a

using (6.19). The virtual coupling network, characterized by the impedance function (6.21), is found using the second condition for absolute stability, (6.34). The resulting lower bound on virtual coupling impedance is shown as a dashed line in Fig. 7.4. The thin solid line shows the same bound when a limit on human operator impedance is included in the design. In the admittance display design, the effect of human impedance level is acute. By eliminating the conservatism associated with permitting unrealistic human-device interactions, reduced virtual coupling impedance levels are achieved. The result is improved performance in the form of less restricted free-space motion. The optimal virtual coupling parameters,  $b_{c_A}$  and  $m_{c_A}$ , are those which cause  $Z_{c_A}$  to minimally exceed the design bound. The real part of virtual coupling impedance, with  $b_{c_A} = 1000 \text{ N} / (\text{m} / \text{s})$  and  $m_{c_A} = 11.0 \text{ kg}$ , is shown in Fig. 7.4 as a bold solid line.

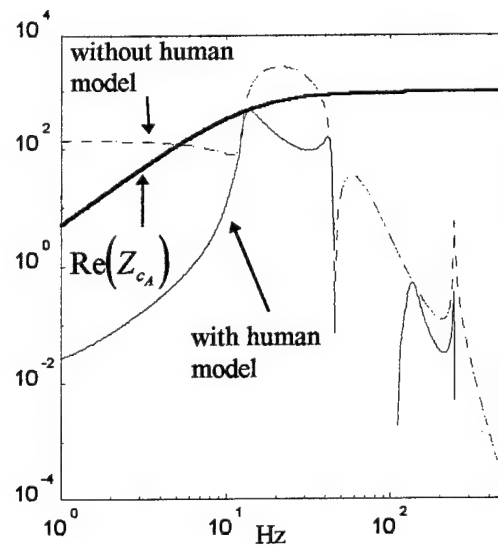


Fig. 7.4. Admittance Display Numerical Design

### 7.3 Experimental Results

The virtual coupling designs described above are implemented in software and tested on the HBFD using a simple virtual environment. For this study, the virtual environment consists of fixed, two-dimensional objects of different shapes and orientations. There is a single moving object,  $O_e$ , whose motion and reaction forces in the  $x$ - and  $y$ -axis are linked

using (6.19). The virtual coupling network, characterized by the impedance function (6.21), is found using the second condition for absolute stability, (6.34). The resulting lower bound on virtual coupling impedance is shown as a dashed line in Fig. 7.4. The thin solid line shows the same bound when a limit on human operator impedance is included in the design. In the admittance display design, the effect of human impedance level is acute. By eliminating the conservatism associated with permitting unrealistic human-device interactions, reduced virtual coupling impedance levels are achieved. The result is improved performance in the form of less restricted free-space motion. The optimal virtual coupling parameters,  $b_{c_A}$  and  $m_{c_A}$ , are those which cause  $Z_{c_A}$  to minimally exceed the design bound. The real part of virtual coupling impedance, with  $b_{c_A} = 1000 \text{ N} / (\text{m} / \text{s})$  and  $m_{c_A} = 11.0 \text{ kg}$ , is shown in Fig. 7.4 as a bold solid line.

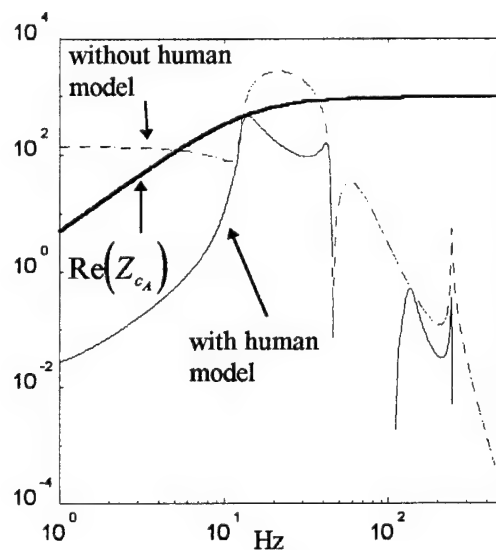


Fig. 7.4. Admittance Display Numerical Design

### 7.3 Experimental Results

The virtual coupling designs described above are implemented in software and tested on the HBFD using a simple virtual environment. For this study, the virtual environment consists of fixed, two-dimensional objects of different shapes and orientations. There is a single moving object,  $O_e$ , whose motion and reaction forces in the  $x$ - and  $y$ -axis are linked

reader is referred to [36] for details. To ideally simulate free motion (zero inertia, zero damping), the virtual environment would have to enforce  $v_e^* = \infty f_e^*$ . In practice, we assume a minimal level of inertia for  $O_e$  in order to ensure numerically stable integration ( $m_e = 0.02 \text{ kg}$ ). The force,  $f_e^*$ , acting on  $O_e$  is determined by the virtual coupling network, which takes the appropriate form from Table 6.1.

Each of the four causality structures (impedance display/impedance environment, impedance display/admittance environment, admittance display/impedance environment, and admittance display/admittance environment) were evaluated on the HBFD hardware using the analytically derived virtual coupling networks. Minimal human impedance was tested by simply letting go of the handle. Maximum human impedance was applied by grasping the handle tightly and extending the elbow to 180 degrees. Minimum virtual environment impedance was simulated by a freely moving object  $O_e$ . Maximum virtual environment impedance was tested by constraining the object  $O_e$  between two rigid virtual walls. The system remained stable, with no undamped oscillations, under all four possible combinations of these extreme human/environment loadings for each of the four causality structures (16 conditions in total). The theoretical guarantee of stability provided by the virtual coupling network is thus confirmed by the experimental results.

The virtual coupling parameters were then tuned experimentally to find the best values under which the haptic simulation remained stable and oscillation-free. The purpose of this tuning step is to determine how close the theoretical limit on virtual coupling impedance is to experimentally determined values. Table 7.1 shows the coupling parameter values at which the simulation becomes marginally stable. In theory, these should exactly match the analytically determined values. In reality, the linear model used to determine the theoretical virtual couplings is not a perfect representation of true system behavior. Errors in the parameter values themselves (parametric modeling error), neglected higher-order structural modes (unstructured modeling error), and nonlinearities

reader is referred to [36] for details. To ideally simulate free motion (zero inertia, zero damping), the virtual environment would have to enforce  $v_e^* = \infty f_e^*$ . In practice, we assume a minimal level of inertia for  $O_e$  in order to ensure numerically stable integration ( $m_e = 0.02 \text{ kg}$ ). The force,  $f_e^*$ , acting on  $O_e$  is determined by the virtual coupling network, which takes the appropriate form from Table 6.1.

Each of the four causality structures (impedance display/impedance environment, impedance display/admittance environment, admittance display/impedance environment, and admittance display/admittance environment) were evaluated on the HBFD hardware using the analytically derived virtual coupling networks. Minimal human impedance was tested by simply letting go of the handle. Maximum human impedance was applied by grasping the handle tightly and extending the elbow to 180 degrees. Minimum virtual environment impedance was simulated by a freely moving object  $O_e$ . Maximum virtual environment impedance was tested by constraining the object  $O_e$  between two rigid virtual walls. The system remained stable, with no undamped oscillations, under all four possible combinations of these extreme human/environment loadings for each of the four causality structures (16 conditions in total). The theoretical guarantee of stability provided by the virtual coupling network is thus confirmed by the experimental results.

The virtual coupling parameters were then tuned experimentally to find the best values under which the haptic simulation remained stable and oscillation-free. The purpose of this tuning step is to determine how close the theoretical limit on virtual coupling impedance is to experimentally determined values. Table 7.1 shows the coupling parameter values at which the simulation becomes marginally stable. In theory, these should exactly match the analytically determined values. In reality, the linear model used to determine the theoretical virtual couplings is not a perfect representation of true system behavior. Errors in the parameter values themselves (parametric modeling error), neglected higher-order structural modes (unstructured modeling error), and nonlinearities

environment simulates free motion. This value is the same as the open loop damping of the device,  $b_{min}=5 \text{ Ns/m}$ .

Solid lines in Fig. 7.6 show the upper and lower bounds for the impedance range of the admittance display implementation. We see by selecting the position regulator according to (7.5) the admittance display has the same upper bound as the impedance display. The bounds on minimum displayable impedance are similar, but not identical. The admittance display achieves very low steady state impedance, while the impedance display exhibits the damping of the open loop device. The admittance display does not do as well in the 1 to 100 rad/s range, where the impedance display achieves lower impedance. To the human operator, the admittance display appears to have much lower damping ( $\sim 0$  vs.  $\sim 5 \text{ Ns/m}$ ) but higher inertia than the impedance display ( $\sim 8$  vs.  $\sim 5 \text{ kg}$ ) when simulating free motion.

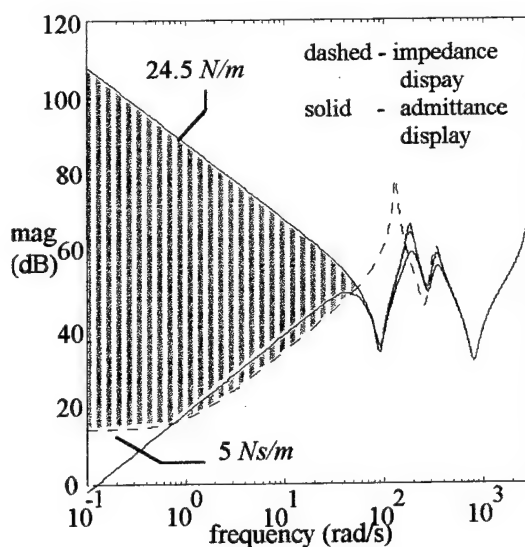


Fig. 7.6. Impedance Range for Impedance and Admittance Display

environment simulates free motion. This value is the same as the open loop damping of the device,  $b_{min}=5 \text{ Ns/m}$ .

Solid lines in Fig. 7.6 show the upper and lower bounds for the impedance range of the admittance display implementation. We see by selecting the position regulator according to (7.5) the admittance display has the same upper bound as the impedance display. The bounds on minimum displayable impedance are similar, but not identical. The admittance display achieves very low steady state impedance, while the impedance display exhibits the damping of the open loop device. The admittance display does not do as well in the  $1$  to  $100 \text{ rad/s}$  range, where the impedance display achieves lower impedance. To the human operator, the admittance display appears to have much lower damping ( $\sim 0$  vs.  $\sim 5 \text{ Ns/m}$ ) but higher inertia than the impedance display ( $\sim 8$  vs.  $\sim 5 \text{ kg}$ ) when simulating free motion.

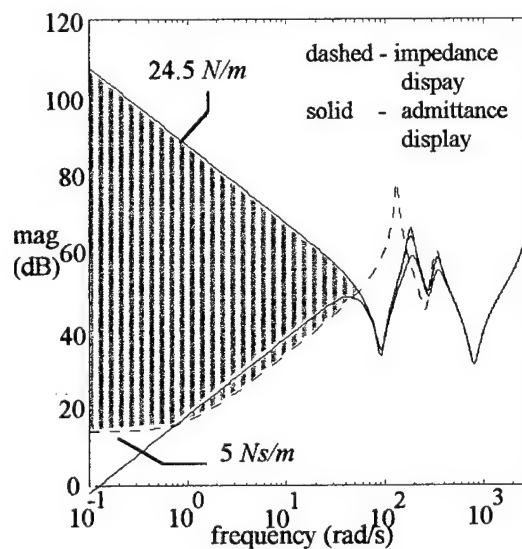


Fig. 7.6. Impedance Range for Impedance and Admittance Display



### 8.1 Modeling

The dynamics of the manipulator are a function of the orientation of the handle within the workspace. All three axes of motion ( $x, y, z$ ) must be considered. For clarity of presentation, we will restrict our attention to a single, worst-case design point for the Excalibur. A successful design for this condition yields a control law which satisfies the stability criteria for all other orientations in all three axes. This worst-case point represents  $x$ -axis motion when the handle is in the neighborhood of  $x = 40 \text{ mm}$ ,  $y = 150 \text{ mm}$ ,  $z = 200 \text{ mm}$ , measured from the lower-left-bottom position as seen in Fig. 8.1. Details on the Excalibur model can be found in [59].

The worst-case design model for Excalibur is defined in terms of the matrices,  $M$ ,  $D$ ,  $K$ ,  $G$ ,  $C_v$ , and  $C_f$ .

$$M = \begin{bmatrix} 0.9271 & 0 & 0 & 0 & 0 \\ 0 & 0.3875 & 0 & 0 & 0 \\ 0 & 0 & 2.4489 & 0.2799 & 0 \\ 0 & 0 & 0.2799 & 0.3343 & 0 \\ 0 & 0 & 0 & 0 & 0.1600 \end{bmatrix} \quad (8.1)$$

$$D = \begin{bmatrix} 8.5600 & -2.7895 & -1.1447 & 0.0487 & 0.0095 \\ -2.7895 & 12.2139 & -7.4320 & 0.0529 & -0.0551 \\ -1.1447 & -7.4320 & 68.2359 & 48.6630 & -47.4150 \\ 0.0487 & 0.0529 & 48.6630 & 49.2727 & -47.3653 \\ 0.0095 & -0.0551 & -47.4150 & -47.3653 & 48.2606 \end{bmatrix} \quad (8.2)$$

$$K = 10^7 \cdot \begin{bmatrix} 0.0236 & -0.0280 & 0.0045 & -0.0003 & -0.0001 \\ -0.0280 & 0.1044 & -0.0764 & 0.0000 & 0.0000 \\ 0.0045 & -0.0764 & 5.3954 & 5.3238 & -5.3235 \\ -0.0003 & 0.0000 & 5.3238 & 5.3270 & -5.3235 \\ -0.0001 & 0.0000 & -5.3235 & -5.3235 & 5.3236 \end{bmatrix} \quad (8.3)$$

$$G = \begin{bmatrix} 0 & -1 \\ 0 & 0 \\ 0 & 0 \\ 0 & 0 \\ 1 & 0 \end{bmatrix} \quad (8.4)$$

### 8.1 Modeling

The dynamics of the manipulator are a function of the orientation of the handle within the workspace. All three axes of motion ( $x, y, z$ ) must be considered. For clarity of presentation, we will restrict our attention to a single, worst-case design point for the Excalibur. A successful design for this condition yields a control law which satisfies the stability criteria for all other orientations in all three axes. This worst-case point represents  $x$ -axis motion when the handle is in the neighborhood of  $x = 40 \text{ mm}$ ,  $y = 150 \text{ mm}$ ,  $z = 200 \text{ mm}$ , measured from the lower-left-bottom position as seen in Fig. 8.1. Details on the Excalibur model can be found in [59].

The worst-case design model for Excalibur is defined in terms of the matrices,  $M$ ,  $D$ ,  $K$ ,  $G$ ,  $C_v$ , and  $C_f$ .

$$M = \begin{bmatrix} 0.9271 & 0 & 0 & 0 & 0 \\ 0 & 0.3875 & 0 & 0 & 0 \\ 0 & 0 & 2.4489 & 0.2799 & 0 \\ 0 & 0 & 0.2799 & 0.3343 & 0 \\ 0 & 0 & 0 & 0 & 0.1600 \end{bmatrix} \quad (8.1)$$

$$D = \begin{bmatrix} 8.5600 & -2.7895 & -1.1447 & 0.0487 & 0.0095 \\ -2.7895 & 12.2139 & -7.4320 & 0.0529 & -0.0551 \\ -1.1447 & -7.4320 & 68.2359 & 48.6630 & -47.4150 \\ 0.0487 & 0.0529 & 48.6630 & 49.2727 & -47.3653 \\ 0.0095 & -0.0551 & -47.4150 & -47.3653 & 48.2606 \end{bmatrix} \quad (8.2)$$

$$K = 10^7 \cdot \begin{bmatrix} 0.0236 & -0.0280 & 0.0045 & -0.0003 & -0.0001 \\ -0.0280 & 0.1044 & -0.0764 & 0.0000 & 0.0000 \\ 0.0045 & -0.0764 & 5.3954 & 5.3238 & -5.3235 \\ -0.0003 & 0.0000 & 5.3238 & 5.3270 & -5.3235 \\ -0.0001 & 0.0000 & -5.3235 & -5.3235 & 5.3236 \end{bmatrix} \quad (8.3)$$

$$G = \begin{bmatrix} 0 & -1 \\ 0 & 0 \\ 0 & 0 \\ 0 & 0 \\ 1 & 0 \end{bmatrix} \quad (8.4)$$

while maximizing virtual coupling impedance, the optimum stability/performance tradeoff is achieved. The left side of (6.25) corresponding to the optimum values,  $k_{c_l} = 51,000 \text{ N/m}$  and  $b_{c_l} = 90 \text{ N/(m/s)}$ , is plotted on Fig. 8.2 as a bold line. The virtual coupling defined by these values provides the stiffest possible interface to rigid virtual environments while guaranteeing the stability of the haptic simulation.

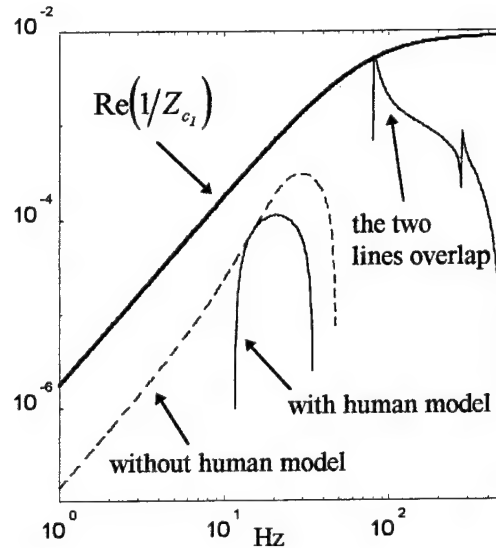


Fig. 8.2. Basic Impedance Display Virtual Coupling Design

### 8.2.2 Impedance Display - with Force Compensation

In this case, we must first design a force regulator  $K_f(z)$  to satisfy (6.26). The right side of (6.30) is plotted in Fig. 8.3 as a dashed line. If we choose a constant gain,  $K_f(z) = k_f$ , its value must be less than 0.07. There is a high degree of conservatism built into this result due to the assumption of arbitrary passive human impedance. The thin solid line in Fig. 8.3 shows the bound, revised to include the human impedance model. We see an order of magnitude increase in the achievable gain when we include this model,  $k_f \leq 0.7$ . The limiting factor is now a peak at the first structural resonance of the device,  $\omega = 50 \text{ Hz}$ . A straightforward approach to reducing this peak is to introduce a notch filter which attenuates the measured force signal at this frequency,

while maximizing virtual coupling impedance, the optimum stability/performance tradeoff is achieved. The left side of (6.25) corresponding to the optimum values,  $k_{c_i} = 51,000 \text{ N/m}$  and  $b_{c_i} = 90 \text{ N/(m/s)}$ , is plotted on Fig. 8.2 as a bold line. The virtual coupling defined by these values provides the stiffest possible interface to rigid virtual environments while guaranteeing the stability of the haptic simulation.

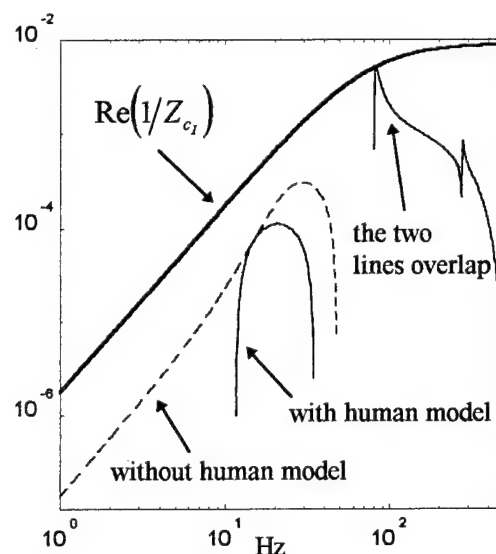


Fig. 8.2. Basic Impedance Display Virtual Coupling Design

### 8.2.2 Impedance Display - with Force Compensation

In this case, we must first design a force regulator  $K_f(z)$  to satisfy (6.26). The right side of (6.30) is plotted in Fig. 8.3 as a dashed line. If we choose a constant gain,  $K_f(z) = k_f$ , its value must be less than 0.07. There is a high degree of conservatism built into this result due to the assumption of arbitrary passive human impedance. The thin solid line in Fig. 8.3 shows the bound, revised to include the human impedance model. We see an order of magnitude increase in the achievable gain when we include this model,  $k_f \leq 0.7$ . The limiting factor is now a peak at the first structural resonance of the device,  $\omega = 50 \text{ Hz}$ . A straightforward approach to reducing this peak is to introduce a notch filter which attenuates the measured force signal at this frequency,

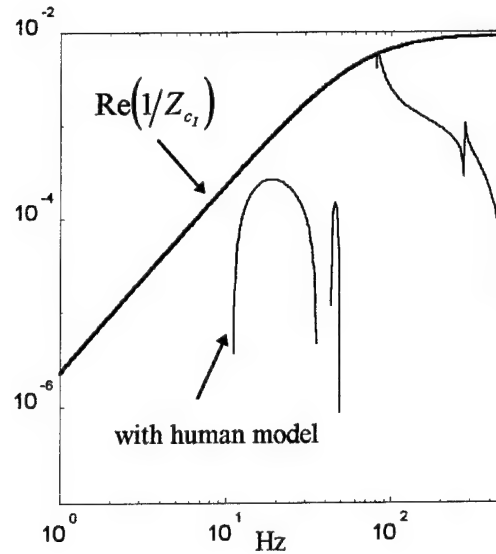


Fig. 8.4. Impedance Display with Force Compensation Virtual Coupling Design

### 8.2.3 Admittance Display

The first step in control law design for the admittance display implementation was accomplished when we found the basic impedance display virtual coupling parameters. Following (6.36), the position regulator is,

$$K_p(z) = 51,000 + 90 \frac{1}{T} (1 - z^{-1}) \text{ N / m.} \quad (8.8)$$

The second step is to use (6.34) to find a virtual coupling which guarantees absolute stability. Fig. 8.5 shows the lower bound on the real part of virtual coupling impedance. The dashed line is the bound calculated without a human impedance model. The thin solid line shows the bound modified to include a limit on maximum human impedance. Here we see that the virtual coupling design is dramatically affected by the introduction of the human model. Conservatism induced by allowing unreasonable levels of human interaction drives the required virtual coupling impedance to excessive levels. The virtual coupling designed using the human model is represented by the bold line in Fig. 8.5.

A two-dimensional numerical search is used to find virtual coupling parameters,  $b_{c_A}$  and  $m_{c_A}$ , which satisfy the inequality (6.34). Values are chosen which meet this inequality

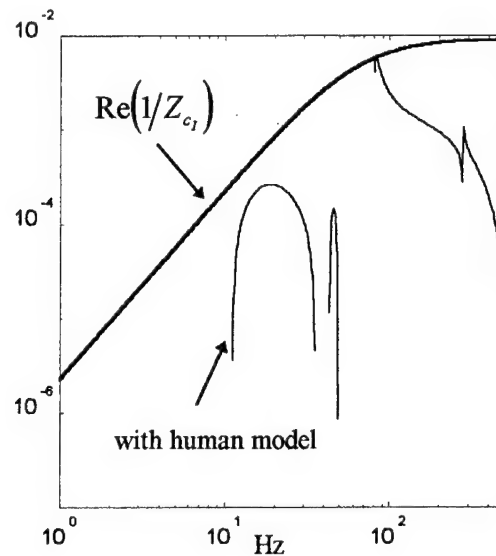


Fig. 8.4. Impedance Display with Force Compensation Virtual Coupling Design

### 8.2.3 Admittance Display

The first step in control law design for the admittance display implementation was accomplished when we found the basic impedance display virtual coupling parameters. Following (6.36), the position regulator is,

$$K_p(z) = 51,000 + 90 \frac{1}{T} (1 - z^{-1}) \text{ N/m}. \quad (8.8)$$

The second step is to use (6.34) to find a virtual coupling which guarantees absolute stability. Fig. 8.5 shows the lower bound on the real part of virtual coupling impedance. The dashed line is the bound calculated without a human impedance model. The thin solid line shows the bound modified to include a limit on maximum human impedance. Here we see that the virtual coupling design is dramatically affected by the introduction of the human model. Conservatism induced by allowing unreasonable levels of human interaction drives the required virtual coupling impedance to excessive levels. The virtual coupling designed using the human model is represented by the bold line in Fig. 8.5.

A two-dimensional numerical search is used to find virtual coupling parameters,  $b_{c_A}$  and  $m_{c_A}$ , which satisfy the inequality (6.34). Values are chosen which meet this inequality

blocks in the virtual environment, its position is constrained to lie on the surface of the obstruction. The blocks may also be vertically mated together by aligning their knobs and overcoming inter-block friction. The equations of motion are integrated using an Euler velocity approximation and a trapezoidal position estimate. As noted by Brown and Colgate [34], since an explicit integration routine is used, the virtual environment does not strictly satisfy discrete-time passivity. The implication here is that we cannot simulate an infinitesimally small mass while maintaining a stable numerical integration of the equations of motion. The cursor and block masses must always be at least 0.25 kg. Simulations show that a lighter mass results in a divergence in the integration routine. This value was theoretically verified by Brian Capozzi of the University of Washington Control Systems Laboratory.

Each of the three control designs described above provide a stable haptic simulation in the VBB system. We use the term stable here to imply that there are no divergent oscillations or perceivable vibrations under any combination of virtual environment state and human operator grasp. The important virtual environment states are: free motion, unilateral block-block collision, and bilaterally constrained block. Possible human operator grasp conditions are: hands-off, relaxed operation, and tight grip with arm fully extended. The first condition corresponds to zero human impedance, the last to maximum grasp impedance.

The control parameters were tuned to find the values which make the system marginally stable. Table 8.1 shows these experimentally derived gains along with their theoretical counterparts. For the basic impedance display virtual coupling, damping was held constant and stiffness increased until instability was first detected. This occurred when the value was augmented by 50% in the virtual environment/human operator combination of bilateral constraint/hands-off. For the impedance implementation with force compensation, the theoretical force gain was increased by 25% until instability occurred in the free-motion/relaxed combination. In this case, the experimental virtual coupling

blocks in the virtual environment, its position is constrained to lie on the surface of the obstruction. The blocks may also be vertically mated together by aligning their knobs and overcoming inter-block friction. The equations of motion are integrated using an Euler velocity approximation and a trapezoidal position estimate. As noted by Brown and Colgate [34], since an explicit integration routine is used, the virtual environment does not strictly satisfy discrete-time passivity. The implication here is that we cannot simulate an infinitesimally small mass while maintaining a stable numerical integration of the equations of motion. The cursor and block masses must always be at least 0.25 *kg*. Simulations show that a lighter mass results in a divergence in the integration routine. This value was theoretically verified by Brian Capozzi of the University of Washington Control Systems Laboratory.

Each of the three control designs described above provide a stable haptic simulation in the VBB system. We use the term stable here to imply that there are no divergent oscillations or perceivable vibrations under any combination of virtual environment state and human operator grasp. The important virtual environment states are: free motion, unilateral block-block collision, and bilaterally constrained block. Possible human operator grasp conditions are: hands-off, relaxed operation, and tight grip with arm fully extended. The first condition corresponds to zero human impedance, the last to maximum grasp impedance.

The control parameters were tuned to find the values which make the system marginally stable. Table 8.1 shows these experimentally derived gains along with their theoretical counterparts. For the basic impedance display virtual coupling, damping was held constant and stiffness increased until instability was first detected. This occurred when the value was augmented by 50% in the virtual environment/human operator combination of bilateral constraint/hands-off. For the impedance implementation with force compensation, the theoretical force gain was increased by 25% until instability occurred in the free-motion/relaxed combination. In this case, the experimental virtual coupling



responses are calculated using the worst-case design model and the theoretical control laws applied to (6.40)-(6.43).

The lower bound represents the free-motion response of the haptic interface. For the basic impedance display, this is simply the open-loop response of the system. Below 10 Hz, this response is dominated by rigid body damping (  $20 \text{ N/(m/s)}$  ) and total inertia (  $3.9 \text{ kg}$  ). At these frequencies, the effect of adding force compensation to the impedance display is to scale down the apparent impedance by a factor of  $1/(1+k_f)$ . In this case, the human operator 'feels' 55% less damping and inertia than in the open loop device (  $9 \text{ N/(m/s)}$  and  $1.8 \text{ kg}$  ). The lower bound for the admittance display implementation is driven by the virtual coupling impedance. At frequencies below 10 Hz, the response is dominated by the coupling mass of  $5.0 \text{ kg}$ . In this case, the operator 'feels' greater inertia than in the impedance implementation, but with zero damping. When the virtual environment simulates free motion, the handle literally floats around the workspace like a frictionless mass.

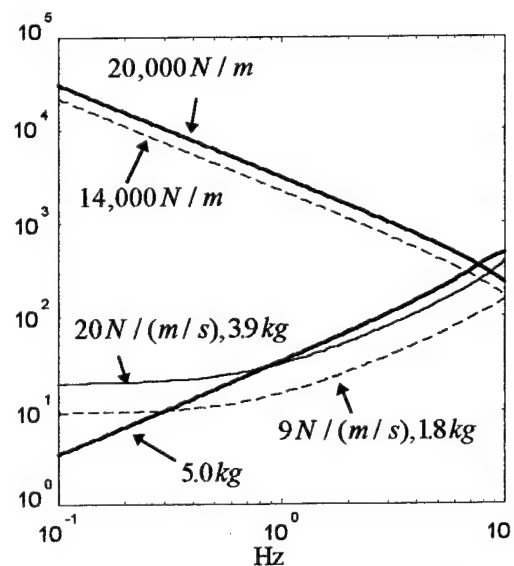


Fig. 8.6. Impedance Range for Three Haptic Display Implementations  
( thin line - impedance display, dashed line - impedance display w/force comp.,  
bold line - admittance display)

responses are calculated using the worst-case design model and the theoretical control laws applied to (6.40)-(6.43).

The lower bound represents the free-motion response of the haptic interface. For the basic impedance display, this is simply the open-loop response of the system. Below 10 Hz, this response is dominated by rigid body damping (  $20 \text{ N/(m/s)}$  ) and total inertia (  $3.9 \text{ kg}$  ). At these frequencies, the effect of adding force compensation to the impedance display is to scale down the apparent impedance by a factor of  $1/(1+k_f)$ . In this case, the human operator 'feels' 55% less damping and inertia than in the open loop device (  $9 \text{ N/(m/s)}$  and  $1.8 \text{ kg}$  ). The lower bound for the admittance display implementation is driven by the virtual coupling impedance. At frequencies below 10 Hz, the response is dominated by the coupling mass of  $5.0 \text{ kg}$ . In this case, the operator 'feels' greater inertia than in the impedance implementation, but with zero damping. When the virtual environment simulates free motion, the handle literally floats around the workspace like a frictionless mass.

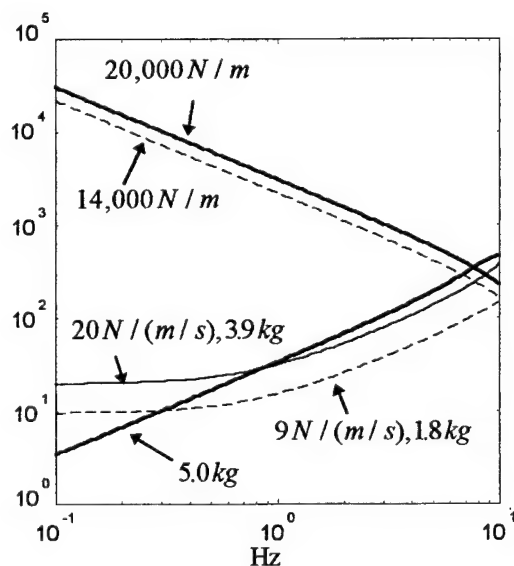


Fig. 8.6. Impedance Range for Three Haptic Display Implementations  
( thin line - impedance display, dashed line - impedance display w/force comp.,  
bold line - admittance display)

for a device which has high levels of non-linear friction and high gear ratios. A significant consideration is that in the latter two implementations, considerable cost must be incurred to add end-point sensing to the device.

An important difference between the impedance display with force compensation and the admittance display is the arrangement of feedback signals. The position measurement is often taken near or at the point of actuation, providing sensor/actuator *collocation*. The force measurement is usually taken near or at the handle, creating sensor/actuator *non-collocation* when flexibility or nonlinearities exist between handle and actuator. The admittance display first closes the loop on the collocated sensor/actuator pair, then feeds back the non-collocated force signal in an outer loop. The collocated inner loop increases damping in the flexible modes, providing an extra margin of stability for the non-collocated outer loop. Both the human operator and the virtual environment tend to filter the force signal before it is fed back to the inner loop. Conversely, in the impedance display with force compensation, the non-collocated loop is closed first. Feeding handle force back to the actuators reduces the damping in the flexible modes, quickly driving them unstable. The feedback gain on measured force, and thus the free-motion performance improvement, is very limited in this case, since the non-collocated input-output pair provide very little gain margin.

We cannot reduce the minimum realizable impedance for the impedance display with force compensation beyond that shown in Fig. 8.6. The ability to tailor the performance of the admittance display is highlighted in Fig. 8.7. By reducing the inner loop position gain to  $10,000 \text{ N/m}$ , the virtual coupling impedance parameters can be reduced to  $b_{c_A} = 450 \text{ N/(m/s)}$  and  $m_{c_A} = 1.5 \text{ kg}$ . The new impedance range bounds show the corresponding improvement in free-motion response ( $1.7 \text{ kg}$ ) and degradation in rigid-constraint performance ( $8,000 \text{ N/m}$ ). The ability to tailor performance in an admittance display implementation makes this approach the most suitable for devices with significant inertia and friction when good free motion performance is required.

for a device which has high levels of non-linear friction and high gear ratios. A significant consideration is that in the latter two implementations, considerable cost must be incurred to add end-point sensing to the device.

An important difference between the impedance display with force compensation and the admittance display is the arrangement of feedback signals. The position measurement is often taken near or at the point of actuation, providing sensor/actuator *collocation*. The force measurement is usually taken near or at the handle, creating sensor/actuator *non-collocation* when flexibility or nonlinearities exist between handle and actuator. The admittance display first closes the loop on the collocated sensor/actuator pair, then feeds back the non-collocated force signal in an outer loop. The collocated inner loop increases damping in the flexible modes, providing an extra margin of stability for the non-collocated outer loop. Both the human operator and the virtual environment tend to filter the force signal before it is fed back to the inner loop. Conversely, in the impedance display with force compensation, the non-collocated loop is closed first. Feeding handle force back to the actuators reduces the damping in the flexible modes, quickly driving them unstable. The feedback gain on measured force, and thus the free-motion performance improvement, is very limited in this case, since the non-collocated input-output pair provide very little gain margin.

We cannot reduce the minimum realizable impedance for the impedance display with force compensation beyond that shown in Fig. 8.6. The ability to tailor the performance of the admittance display is highlighted in Fig. 8.7. By reducing the inner loop position gain to  $10,000 \text{ N/m}$ , the virtual coupling impedance parameters can be reduced to  $b_{c_A} = 450 \text{ N/(m/s)}$  and  $m_{c_A} = 1.5 \text{ kg}$ . The new impedance range bounds show the corresponding improvement in free-motion response ( $1.7 \text{ kg}$ ) and degradation in rigid-constraint performance ( $8,000 \text{ N/m}$ ). The ability to tailor performance in an admittance display implementation makes this approach the most suitable for devices with significant inertia and friction when good free motion performance is required.

## Chapter 9

### Virtual Building Block Training Study

This chapter describes an experiment, conducted to investigate the benefits of force feedback for virtual reality training. Three groups of test operators receive different levels of training before completing a manual task, the construction of a LEGO™ biplane model. One group trains on a Virtual Building Block (VBB) simulation which emulates the real task in a virtual environment, including haptic feedback. A second group also trains on the VBB system, but without the benefit of force feedback. The last group receives no virtual reality training. Completion times are compared for these different groups in building the actual biplane model in the real world. Results show that training with haptic feedback provides a significant performance benefit. Fig. 9.1 shows the virtual and real LEGO™ biplane models.

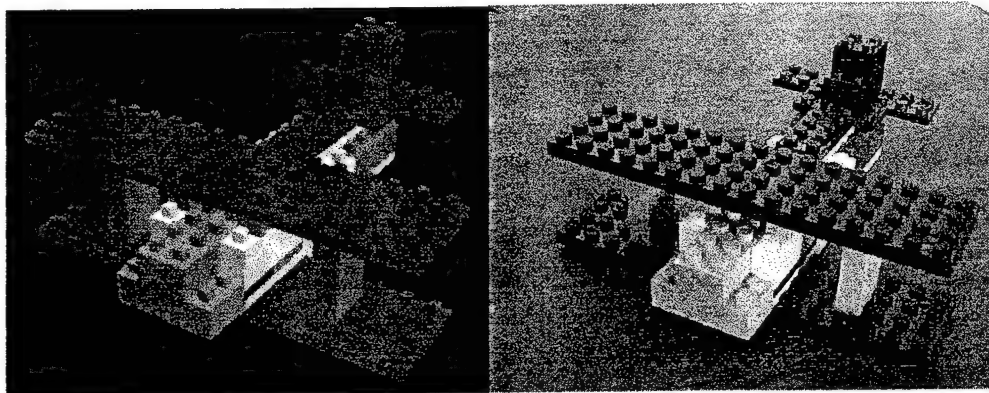


Fig. 9.1. Virtual and Real Biplane Models

This study is made possible by the results on system stability described in previous chapters. A basic impedance display implementation, based on the Excalibur force display, is used in conjunction with the virtual coupling design described in Chapter 8. The absolute stability of the resulting haptic interface provides a high degree of confidence

## Chapter 9

### Virtual Building Block Training Study

This chapter describes an experiment, conducted to investigate the benefits of force feedback for virtual reality training. Three groups of test operators receive different levels of training before completing a manual task, the construction of a LEGO™ biplane model. One group trains on a Virtual Building Block (VBB) simulation which emulates the real task in a virtual environment, including haptic feedback. A second group also trains on the VBB system, but without the benefit of force feedback. The last group receives no virtual reality training. Completion times are compared for these different groups in building the actual biplane model in the real world. Results show that training with haptic feedback provides a significant performance benefit. Fig. 9.1 shows the virtual and real LEGO™ biplane models.

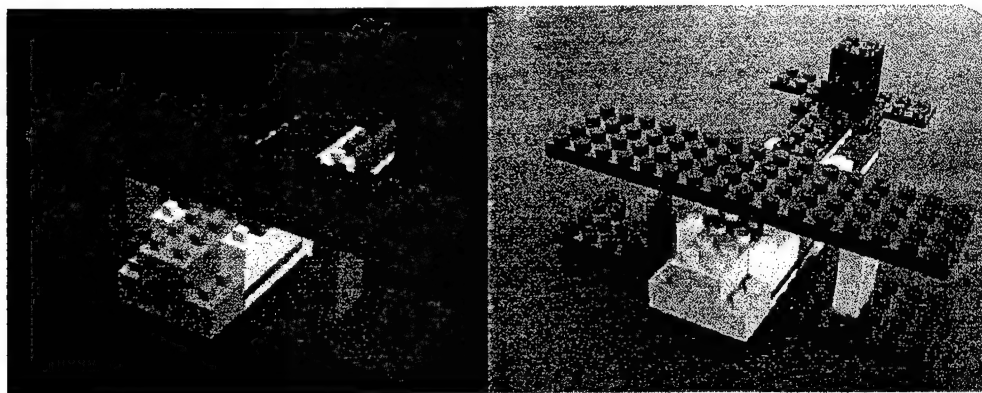


Fig. 9.1. Virtual and Real Biplane Models

This study is made possible by the results on system stability described in previous chapters. A basic impedance display implementation, based on the Excalibur force display, is used in conjunction with the virtual coupling design described in Chapter 8. The absolute stability of the resulting haptic interface provides a high degree of confidence

Can training in a virtual environment be successfully transferred to a manual task in the real world? While a number of researchers have attempted to address this issue with mixed results [63], [64], [65], the answer to this question must manifestly be yes. Ideally, the user of a virtual reality system cannot distinguish between what is virtual and what is real. Thus, to the trainee, there is no difference between a virtual training experience and training on the actual task. Any difference between the virtual and real world can be attributed to technological limitations. Field-of-view constraints on visual displays, slow refresh rates, delays in head mounted tracking systems, and insufficient detail in the rendering of a virtual scene all detract from the visual sense of immersion in a virtual environment. Even with a perfect visual virtual reality display, the scene is incomplete without haptic feedback. The trainee's hand passes unimpeded through objects. The user cannot feel the tool in his or her hand and it provides no resistance when coming into contact with the environment.

## 9.2 Apparatus

The VBB system consists of the Excalibur force display equipped with a stabilizing virtual coupling network and a virtual environment which emulates the behavior of LEGO™ blocks. In one hand, the user grasps the handle of the force display. In the other hand, the subject holds a two-button wireless mouse. The operator sees a 3-D graphical representation of the scene on a large monitor and feels a 3-D haptic rendering of the scene through the Excalibur display. Fig. 9.2 shows the VBB system.

### 9.2.1 Excalibur Force Display

Details on the Excalibur device can be found in Chapter 8 and in [59]. For this study, a basic impedance display implementation is used. This configuration was chosen for its simplicity and robustness, critical factors when conducting tests with human test operators. The experimentally tuned virtual coupling, described in Section 8.3, is used ( $k_{c_i} = 75,000 \text{ N/m}$  and  $b_{c_i} = 90 \text{ N/(m/s)}$ ).

Can training in a virtual environment be successfully transferred to a manual task in the real world? While a number of researchers have attempted to address this issue with mixed results [63], [64], [65], the answer to this question must manifestly be *yes*. Ideally, the user of a virtual reality system cannot distinguish between what is virtual and what is real. Thus, to the trainee, there is no difference between a virtual training experience and training on the actual task. Any difference between the virtual and real world can be attributed to technological limitations. Field-of-view constraints on visual displays, slow refresh rates, delays in head mounted tracking systems, and insufficient detail in the rendering of a virtual scene all detract from the visual sense of immersion in a virtual environment. Even with a perfect visual virtual reality display, the scene is incomplete without haptic feedback. The trainee's hand passes unimpeded through objects. The user cannot feel the tool in his or her hand and it provides no resistance when coming into contact with the environment.

## 9.2 Apparatus

The VBB system consists of the Excalibur force display equipped with a stabilizing virtual coupling network and a virtual environment which emulates the behavior of LEGO™ blocks. In one hand, the user grasps the handle of the force display. In the other hand, the subject holds a two-button wireless mouse. The operator sees a 3-D graphical representation of the scene on a large monitor and feels a 3-D haptic rendering of the scene through the Excalibur display. Fig. 9.2 shows the VBB system.

### 9.2.1 Excalibur Force Display

Details on the Excalibur device can be found in Chapter 8 and in [59]. For this study, a basic impedance display implementation is used. This configuration was chosen for its simplicity and robustness, critical factors when conducting tests with human test operators. The experimentally tuned virtual coupling, described in Section 8.3, is used ( $k_{c_i} = 75,000 \text{ N/m}$  and  $b_{c_i} = 90 \text{ N/(m/s)}$ ).



selected block. When this block comes into contact with others in the environment, a collision takes place and the selected block is constrained. If force feedback is activated, the user feels the inter-block reaction forces. A high level of virtual coupling stiffness gives an extremely compelling crispness to contact between building blocks. When the selected block is properly aligned with another in the horizontal plane, they can be 'snapped' together along the vertical axis. Since Excalibur is a three-axis device, only translational movements are possible. The blocks always remain orthogonally aligned with each other.

When the software is in SELECT mode, the operator can hold down the right mouse button and use the cursor to 'cluster' a group of blocks together. The clustered bricks can then be moved as an assembly. Keyboard commands are used to adjust the working view of the environment right, left, up, down, in, or out. The virtual model can also be flipped upside-down to easily permit work on the underside. The VBB software currently supports 10 different types of blocks, with up to 50 blocks simulated at once.

### **9.3 Experimental Design**

The purpose of the VBB training study is to assess the influence of haptic feedback on the efficacy of virtual reality training. A total of 15 subjects are exposed to one of three different treatments: virtual training with haptics, virtual training without haptics, and no virtual training. They then build a real LEGO™ biplane model five times in succession. The dependent variable is completion time for the real model.

There are two primary considerations in designing a suitable experiment for the VBB training study: skill transfer and subject aptitude. The nature of the training study precludes the use of a within-subjects design, in which each subject is subjected to all treatments. The problem is once an individual has undergone one level of training and performed the actual biplane construction task, the skills learned will not be forgotten if the subject is then re-trained at a different level. There is a very high degree of skill transfer from one treatment to another. It is also likely this transfer will be asymmetrical,

selected block. When this block comes into contact with others in the environment, a collision takes place and the selected block is constrained. If force feedback is activated, the user feels the inter-block reaction forces. A high level of virtual coupling stiffness gives an extremely compelling crispness to contact between building blocks. When the selected block is properly aligned with another in the horizontal plane, they can be 'snapped' together along the vertical axis. Since Excalibur is a three-axis device, only translational movements are possible. The blocks always remain orthogonally aligned with each other.

When the software is in SELECT mode, the operator can hold down the right mouse button and use the cursor to 'cluster' a group of blocks together. The clustered bricks can then be moved as an assembly. Keyboard commands are used to adjust the working view of the environment right, left, up, down, in, or out. The virtual model can also be flipped upside-down to easily permit work on the underside. The VBB software currently supports 10 different types of blocks, with up to 50 blocks simulated at once.

### **9.3 Experimental Design**

The purpose of the VBB training study is to assess the influence of haptic feedback on the efficacy of virtual reality training. A total of 15 subjects are exposed to one of three different treatments: virtual training with haptics, virtual training without haptics, and no virtual training. They then build a real LEGO™ biplane model five times in succession. The dependent variable is completion time for the real model.

There are two primary considerations in designing a suitable experiment for the VBB training study: skill transfer and subject aptitude. The nature of the training study precludes the use of a within-subjects design, in which each subject is subjected to all treatments. The problem is once an individual has undergone one level of training and performed the actual biplane construction task, the skills learned will not be forgotten if the subject is then re-trained at a different level. There is a very high degree of skill transfer from one treatment to another. It is also likely this transfer will be asymmetrical,

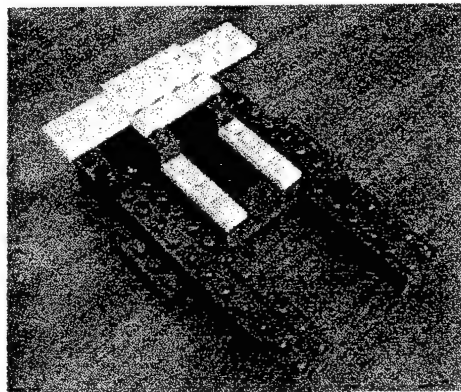


Fig. 9.3. Matching Test Hydrofoil Boat Model

The matching test is completed at least two weeks prior to administration of the actual experiment. The likelihood of significant skill transfer, in the form of increased LEGO<sup>TM</sup> assembly aptitude, from the matching test to the experimental task is considered low. If any skill transfer does take place, it should apply equally to all three treatment groups. The hydrofoil boat construction pre-test is therefore not prone to bias the results of the VBB study.

A total of 15 subjects are pre-tested. These subjects are then rank ordered from 1 to 15 according to their matching test score and grouped into 5 matched subject triads. The first three individuals, those with the fastest average pre-test times, make up the first matched subject triad. The second three make up another, and so forth, to form a total of 5 triads. Each of the three subjects in a triad are randomly assigned to one of the three treatments. Thus a total of 5 subjects, one from each triad, undergo each treatment.

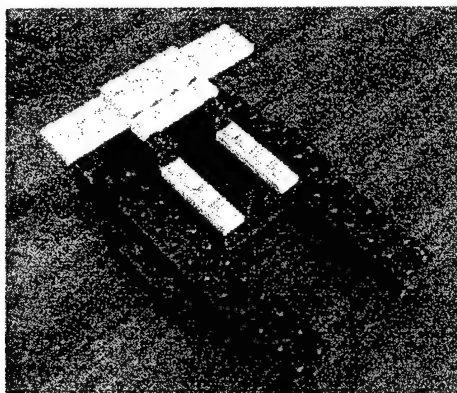


Fig. 9.3. Matching Test Hydrofoil Boat Model

The matching test is completed at least two weeks prior to administration of the actual experiment. The likelihood of significant skill transfer, in the form of increased LEGO™ assembly aptitude, from the matching test to the experimental task is considered low. If any skill transfer does take place, it should apply equally to all three treatment groups. The hydrofoil boat construction pre-test is therefore not prone to bias the results of the VBB study.

A total of 15 subjects are pre-tested. These subjects are then rank ordered from 1 to 15 according to their matching test score and grouped into 5 matched subject triads. The first three individuals, those with the fastest average pre-test times, make up the first matched subject triad. The second three make up another, and so forth, to form a total of 5 triads. Each of the three subjects in a triad are randomly assigned to one of the three treatments. Thus a total of 5 subjects, one from each triad, undergo each treatment.

$$H_1: \beta_1 = \beta_2 = \beta_3 = \beta_4 = \beta_5 \quad (9.2)$$

If  $H_1$  is rejected, then we can say inter-subject variability, as predicted by the matching test, is significant.

#### 9.4 Results

Table 9.1 shows completion times for the real LEGO™ biplane test. Results are presented for only 14 of the original 15 subjects. One subject in the third treatment group was not able to complete the biplane experiment.

Table 9.1. LEGO™ Model Completion Times in Seconds

treatment	matched triad	iteration 1	iteration 2	iteration 3	iteration 4	iteration 5	test average	pre-test average
1	1	80	64	57	62	78	68	68
1	2	92	80	72	80	67	78	73
1	3	109	212	105	93	100	124	92
1	4	233	170	113	95	90	140	102
1	5	172	134	90	88	88	114	110
treatment 1 average		<b>137.2</b>	<b>132.0</b>	<b>87.4</b>	<b>83.6</b>	<b>84.6</b>	<b>105.0</b>	<b>89.0</b>
standard deviation		<b>64.2</b>	<b>61.6</b>	<b>23.1</b>	<b>13.4</b>	<b>12.6</b>	<b>30.6</b>	<b>18.0</b>
2	1	111	104	74	80	67	87	62
2	2	145	180	97	78	68	114	80
2	3	173	101	92	80	88	107	94
2	4	188	144	101	100	94	125	98
2	5	293	158	209	83	75	164	106
treatment 2 average		<b>182.0</b>	<b>137.4</b>	<b>114.6</b>	<b>84.2</b>	<b>78.4</b>	<b>119.3</b>	<b>88.1</b>
standard deviation		<b>68.6</b>	<b>34.4</b>	<b>53.8</b>	<b>9.0</b>	<b>12.1</b>	<b>28.4</b>	<b>17.6</b>
3	1	235	109	104	82	80	122	70
3	2	279	151	112	107	114	153	87
3	3	194	157	93	107	97	130	94
3	5	240	199	148	142	146	175	124
treatment 3 average		<b>237.0</b>	<b>154.0</b>	<b>114.3</b>	<b>109.5</b>	<b>109.3</b>	<b>144.8</b>	<b>93.7</b>
standard deviation		<b>34.8</b>	<b>36.8</b>	<b>23.8</b>	<b>24.7</b>	<b>28.2</b>	<b>24.0</b>	<b>22.7</b>

$$H_1: \beta_1 = \beta_2 = \beta_3 = \beta_4 = \beta_5 \quad (9.2)$$

If  $H_1$  is rejected, then we can say inter-subject variability, as predicted by the matching test, is significant.

#### 9.4 Results

Table 9.1 shows completion times for the real LEGO™ biplane test. Results are presented for only 14 of the original 15 subjects. One subject in the third treatment group was not able to complete the biplane experiment.

Table 9.1. LEGO™ Model Completion Times in Seconds

treatment	matched triad	iteration 1	iteration 2	iteration 3	iteration 4	iteration 5	test average	pre-test average
1	1	80	64	57	62	78	68	68
1	2	92	80	72	80	67	78	73
1	3	109	212	105	93	100	124	92
1	4	233	170	113	95	90	140	102
1	5	172	134	90	88	88	114	110
treatment 1 average		<b>137.2</b>	<b>132.0</b>	<b>87.4</b>	<b>83.6</b>	<b>84.6</b>	<b>105.0</b>	<b>89.0</b>
standard deviation		<b>64.2</b>	<b>61.6</b>	<b>23.1</b>	<b>13.4</b>	<b>12.6</b>	<b>30.6</b>	<b>18.0</b>
2	1	111	104	74	80	67	87	62
2	2	145	180	97	78	68	114	80
2	3	173	101	92	80	88	107	94
2	4	188	144	101	100	94	125	98
2	5	293	158	209	83	75	164	106
treatment 2 average		<b>182.0</b>	<b>137.4</b>	<b>114.6</b>	<b>84.2</b>	<b>78.4</b>	<b>119.3</b>	<b>88.1</b>
standard deviation		<b>68.6</b>	<b>34.4</b>	<b>53.8</b>	<b>9.0</b>	<b>12.1</b>	<b>28.4</b>	<b>17.6</b>
3	1	235	109	104	82	80	122	70
3	2	279	151	112	107	114	153	87
3	3	194	157	93	107	97	130	94
3	5	240	199	148	142	146	175	124
treatment 3 average		<b>237.0</b>	<b>154.0</b>	<b>114.3</b>	<b>109.5</b>	<b>109.3</b>	<b>144.8</b>	<b>93.7</b>
standard deviation		<b>34.8</b>	<b>36.8</b>	<b>23.8</b>	<b>24.7</b>	<b>28.2</b>	<b>24.0</b>	<b>22.7</b>

time also shows a significant training effect. The fact the initial iteration is significantly affected by VBB training is not surprising. It is this first trial when untrained subjects, having only passively watched the biplane built in a 4 minute video, struggle the most to figure out how the pieces are arranged. The subjects who have had the benefit of the VBB training system have already formed an internal model of the process in their memories. If the virtual environment adequately represents the real task, this internal model assists these subjects in performing the initial biplane assembly. It is also understandable that the training effect is less pronounced in subsequent iterations. Having performed the actual task once or more, the untrained subject is much better equipped to handle the task. After enough iterations of the real task have been performed, we would expect the level at which a subject is pre-trained to become insignificant. Fig. 9.4 shows the progression of the mean completion time for each treatment group with iteration number.

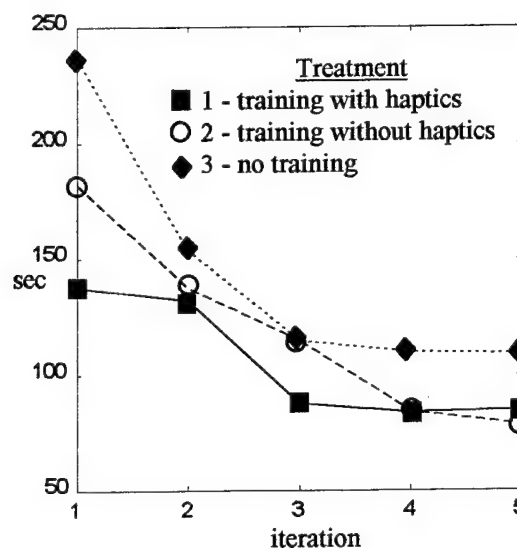


Fig. 9.4. Mean Biplane Completion Time versus Iteration

It is surprising to find a significant training effect in the fourth iteration of biplane construction, with subjects having had the opportunity to build the actual model three times. Closer analysis of the data reveals that although the mean differences in completion times are small at this latter stage, the variance in the data decreases faster (with iteration)

time also shows a significant training effect. The fact the initial iteration is significantly affected by VBB training is not surprising. It is this first trial when untrained subjects, having only passively watched the biplane built in a 4 minute video, struggle the most to figure out how the pieces are arranged. The subjects who have had the benefit of the VBB training system have already formed an internal model of the process in their memories. If the virtual environment adequately represents the real task, this internal model assists these subjects in performing the initial biplane assembly. It is also understandable that the training effect is less pronounced in subsequent iterations. Having performed the actual task once or more, the untrained subject is much better equipped to handle the task. After enough iterations of the real task have been performed, we would expect the level at which a subject is pre-trained to become insignificant. Fig. 9.4 shows the progression of the mean completion time for each treatment group with iteration number.

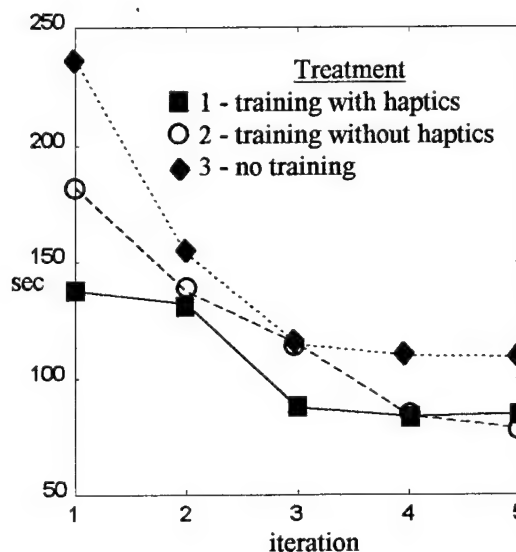


Fig. 9.4. Mean Biplane Completion Time versus Iteration

It is surprising to find a significant training effect in the fourth iteration of biplane construction, with subjects having had the opportunity to build the actual model three times. Closer analysis of the data reveals that although the mean differences in completion times are small at this latter stage, the variance in the data decreases faster (with iteration)



different than those trained with haptics or those with no training. For iteration 4, subjects trained on the VBB system both with and without haptics performed significantly better than those with no training. Again though, the difference between those trained with haptics and those trained without is not significant.

Table 9.3. Pair-Wise Comparisons Using Tukey HSD

hypothesis	iteration 1	iteration 4
$\tau_1 = \tau_3$ (training with haptics and graphics versus no training)	* .049	* .037
$\tau_2 = \tau_3$ (training with graphics only versus no training)	.295	* .041
$\tau_1 = \tau_2$ (training with haptics and graphics versus training with graphics only)	.386	.997

\* - significant at 5% level

The VBB training study succeeds in showing a significant benefit in the use of virtual reality training with force feedback. Results were inconclusive as to whether training with haptics improves performance versus training without force feedback. The variance in human performance (completion time) is high in comparison to mean differences between types of training. Data from this study implies at least twice the number of subjects (30) would be required to show a significant difference between treatments 1 and 2 for the first iteration.

different than those trained with haptics or those with no training. For iteration 4, subjects trained on the VBB system both with and without haptics performed significantly better than those with no training. Again though, the difference between those trained with haptics and those trained without is not significant.

Table 9.3. Pair-Wise Comparisons Using Tukey HSD

hypothesis	iteration 1	iteration 4
$\tau_1 = \tau_3$ (training with haptics and graphics versus no training)	* .049	* .037
$\tau_2 = \tau_3$ (training with graphics only versus no training)	.295	* .041
$\tau_1 = \tau_2$ (training with haptics and graphics versus training with graphics only)	.386	.997

\* - significant at 5% level

The VBB training study succeeds in showing a significant benefit in the use of virtual reality training with force feedback. Results were inconclusive as to whether training with haptics improves performance versus training without force feedback. The variance in human performance (completion time) is high in comparison to mean differences between types of training. Data from this study implies at least twice the number of subjects (30) would be required to show a significant difference between treatments 1 and 2 for the first iteration.

greatly enhances the users' perception of the environment. This enhanced sense of immersion allows the trainee to operate more effectively in the virtual world and more rapidly construct a cognitive model of the task. Subjects who had the benefit of force feedback completed the biplane in the virtual world an average of twice in 30 minutes. Subjects who trained without haptics completed the virtual model an average of only one time in this period. Notice that even with haptics, it took users an average of 15 minutes to build the virtual biplane compared to less than 4 minutes for the first iteration of untrained users working on the real model.

greatly enhances the users' perception of the environment. This enhanced sense of immersion allows the trainee to operate more effectively in the virtual world and more rapidly construct a cognitive model of the task. Subjects who had the benefit of force feedback completed the biplane in the virtual world an average of twice in 30 minutes. Subjects who trained without haptics completed the virtual model an average of only one time in this period. Notice that even with haptics, it took users an average of 15 minutes to build the virtual biplane compared to less than 4 minutes for the first iteration of untrained users working on the real model.

or constraint based. This natural separation of hardware and software is an important step in the growth of haptics as an industry. It will allow innovative businesses and individuals to build devices and write software that are compatible and safe.

A Virtual Building Block simulator has been built around an absolutely stable haptic interface, designed using the above techniques. This system was used to conduct a study regarding the benefits of force feedback in training for a manual task in a virtual environment. Three different levels of treatments were applied to matched subject groups before asking them to build a LEGO™ biplane model: training with haptics, training without haptics, and no training. Statistical analysis of the resulting completion times for the real LEGO™ biplane demonstrate training with haptic feedback has a significant effect on performance.

Future work on stable haptic interaction should focus on methods for efficient implementation of virtual environments. The primary computational bottleneck in building advanced haptic simulations is the need to perform collision detection and response at deterministic frame rates of 1000 Hz or greater. Current collision algorithms which handle complex object interactions require operations such as time back-stepping which are not conducive to real time implementations. The performance of these algorithms for interesting physics-based simulations is almost two orders of magnitude too slow for haptic application, with typical frame rates of about 10 Hz. Rapid gains in cheap computing power and parallel computing architectures will continue to ameliorate the computational problem, but advances on the theoretical front are also needed.

or constraint based. This natural separation of hardware and software is an important step in the growth of haptics as an industry. It will allow innovative businesses and individuals to build devices and write software that are compatible and safe.

A Virtual Building Block simulator has been built around an absolutely stable haptic interface, designed using the above techniques. This system was used to conduct a study regarding the benefits of force feedback in training for a manual task in a virtual environment. Three different levels of treatments were applied to matched subject groups before asking them to build a LEGO™ biplane model: training with haptics, training without haptics, and no training. Statistical analysis of the resulting completion times for the real LEGO™ biplane demonstrate training with haptic feedback has a significant effect on performance.

Future work on stable haptic interaction should focus on methods for efficient implementation of virtual environments. The primary computational bottleneck in building advanced haptic simulations is the need to perform collision detection and response at deterministic frame rates of 1000 Hz or greater. Current collision algorithms which handle complex object interactions require operations such as time back-stepping which are not conducive to real time implementations. The performance of these algorithms for interesting physics-based simulations is almost two orders of magnitude too slow for haptic application, with typical frame rates of about 10 Hz. Rapid gains in cheap computing power and parallel computing architectures will continue to ameliorate the computational problem, but advances on the theoretical front are also needed.

[12]

Massie, T.H. and Salisbury J.K., "The Phantom Haptic Interface: A Device for Probing Virtual Objects," *Proc. ASME International Mechanical Engineering Congress and Exhibition*, Chicago, pp. 295-302, 1994.

[13]

Buttolo, P. and Hannaford, B., "Pen Based Force Display for Precision Manipulation of Virtual Environments," *Proc. IEEE Virtual Reality Annual Int. Symposium*, Raleigh, NC, pp. 217-225, 1995.

[14]

Buttolo, P., Oboe R., Hannaford B., and McNeely W., "Force Feedback in Shared Virtual Simulations," *Proceedings MICAD*, Paris, 1996.

[15]

Hollis, R.L., Salcudean, S.E., and Allan A.P., "A Six-Degree-of-Freedom Magnetically Levitated Variable Compliance Fine-Motion Wrist: Design, Modeling, and Control," *IEEE Trans. Robotics and Automation*, vol. 7, no. 3, pp. 320-332, 1991.

[16]

Salcudean, S.E., Wong, N.M., and Hollis, R.L., "Design and Control of a Force-Reflecting Teleoperation System with Magnetically Levitated Master and Wrist", *IEEE Transactions on Robotics and Automation*, vol. 11, no. 6, pp. 844-858, 1995.

[17]

Salcudean, S.E., and Vlaar, T.D., "On the Emulation of Stiff Walls and Static Friction with a Magnetically Levitated Input/Output Device," *Trans. ASME, Journal of Dynamic Systems, Measurement, and Control*, vol. 119, no. 1, pp. 127-132, 1997.

[18]

Moreyra, M. R. and Hannaford, B., "A Practical Measure of Dynamic Response of Haptic Devices," *Proceedings IEEE Int. Conf. Robotics and Automation*, Leuven, Belgium, pp. 369-374, 1998.

[19]

Bergamasco, M., et. al., "An Arm Exoskeleton System for Teleoperation and Virtual Environments Applications," *Proc. IEEE Int. Conf. Robotics and Automation*, Los Alamitos, CA, pp. 1449-54, 1994.

[20]

Maekawa, H., Hollerbach, J.M., "Haptic Display for Object Grasping and Manipulating in Virtual Environment," *Proceedings IEEE Int. Conf. Robotics and Automation*, Leuven, Belgium, pp. 2566-73, 1998.

[12]

Massie, T.H. and Salisbury J.K., "The Phantom Haptic Interface: A Device for Probing Virtual Objects," *Proc. ASME International Mechanical Engineering Congress and Exhibition*, Chicago, pp. 295-302, 1994.

[13]

Buttolo, P. and Hannaford, B., "Pen Based Force Display for Precision Manipulation of Virtual Environments," *Proc. IEEE Virtual Reality Annual Int. Symposium*, Raleigh, NC, pp. 217-225, 1995.

[14]

Buttolo, P., Oboe R., Hannaford B., and McNeely W., "Force Feedback in Shared Virtual Simulations," *Proceedings MICAD*, Paris, 1996.

[15]

Hollis, R.L., Salcudean, S.E., and Allan A.P., "A Six-Degree-of-Freedom Magnetically Levitated Variable Compliance Fine-Motion Wrist: Design, Modeling, and Control," *IEEE Trans. Robotics and Automation*, vol. 7, no. 3, pp. 320-332, 1991.

[16]

Salcudean, S.E., Wong, N.M., and Hollis, R.L., "Design and Control of a Force-Reflecting Teleoperation System with Magnetically Levitated Master and Wrist", *IEEE Transactions on Robotics and Automation*, vol. 11, no. 6, pp. 844-858, 1995.

[17]

Salcudean, S.E., and Vlaar, T.D., "On the Emulation of Stiff Walls and Static Friction with a Magnetically Levitated Input/Output Device," *Trans. ASME, Journal of Dynamic Systems, Measurement, and Control*, vol. 119, no. 1, pp. 127-132, 1997.

[18]

Moreyra, M. R. and Hannaford, B., "A Practical Measure of Dynamic Response of Haptic Devices," *Proceedings IEEE Int. Conf. Robotics and Automation*, Leuven, Belgium, pp. 369-374, 1998.

[19]

Bergamasco, M., et. al., "An Arm Exoskeleton System for Teleoperation and Virtual Environments Applications," *Proc. IEEE Int. Conf. Robotics and Automation*, Los Alamitos, CA, pp. 1449-54, 1994.

[20]

Maekawa, H., Hollerbach, J.M., "Haptic Display for Object Grasping and Manipulating in Virtual Environment," *Proceedings IEEE Int. Conf. Robotics and Automation*, Leuven, Belgium, pp. 2566-73, 1998.



[31]

Colgate, J.E., Grainger, P.E., Stanley, M.C., and Schenkel, G., "Implementation of Stiff Virtual Walls in Force-Reflecting Interfaces," *Proc. IEEE Virtual Reality Annual Int. Symposium*, Seattle, pp. 202-208, 1993.

[32]

Colgate, J.E. and Schenkel, G., "Passivity of a Class of Sampled-Data Systems: Application to Haptic Interfaces," *Proc. American Control Conference*, Baltimore, pp. 3236-40, 1994.

[33]

Colgate, J.E., Stanley, M.C., and Brown, J.M., "Issues in the Haptic Display of Tool Use," *Proceedings of the IEEE/RSJ International Conference on Intelligent Robots and Systems*, Pittsburgh, PA, pp. 140-145, 1995.

[34]

Brown, J.M. and Colgate, J.E., "Passive Implementation of Multibody Simulations for Haptic Display," *Proceedings of the ASME International Mechanical Engineering Congress and Exhibition*, Dallas, TX, pp. 85-92, 1997.

[35]

Brown, J.M. and Colgate, J.E., "Minimum Mass for Haptic Display Simulations," *Proceedings of the ASME International Mechanical Engineering Congress and Exhibition*, Anaheim, CA, pp. 249-56, 1998.

[36]

Zilles, C.B. and Salisbury, J.K., "A Constraint-based God-object Method for Haptic Display," *Proc. IEEE/RSJ Int. Conf. on Intelligent Robots and Systems*, Pittsburgh, PA, pp. 146-151, 1995.

[37]

Ruspini, D.C., Kolarov, K., and Khatib, O., "The Haptic Display of Complex Graphical Environments," *Computer Graphics Proceedings, SIGGRAPH '97*, Los Angeles, 345-352, 1997.

[38]

Yoshikawa, T., Yokokohji, Y., Matsumoto, T., Zheng, X.-Z., "Display of Feel for the Manipulation of Dynamic Virtual Objects," *Trans. ASME, Journal of Dynamic Systems, Measurement, and Control*, vol. 117, no. 4, pp. 554-8, 1995.

[39]

Kuh, E.S. and Rohrer, R.A., *Theory of Linear Active Networks*, San Francisco: Holden-Day, Inc., 1967.

[31]

Colgate, J.E., Grafing, P.E., Stanley, M.C., and Schenkel, G., "Implementation of Stiff Virtual Walls in Force-Reflecting Interfaces," *Proc. IEEE Virtual Reality Annual Int. Symposium*, Seattle, pp. 202-208, 1993.

[32]

Colgate, J.E. and Schenkel, G., "Passivity of a Class of Sampled-Data Systems: Application to Haptic Interfaces," *Proc. American Control Conference*, Baltimore, pp. 3236-40, 1994.

[33]

Colgate, J.E., Stanley, M.C., and Brown, J.M., "Issues in the Haptic Display of Tool Use," *Proceedings of the IEEE/RSJ International Conference on Intelligent Robots and Systems*, Pittsburgh, PA, pp. 140-145, 1995.

[34]

Brown, J.M. and Colgate, J.E., "Passive Implementation of Multibody Simulations for Haptic Display," *Proceedings of the ASME International Mechanical Engineering Congress and Exhibition*, Dallas, TX, pp. 85-92, 1997.

[35]

Brown, J.M. and Colgate, J.E., "Minimum Mass for Haptic Display Simulations," *Proceedings of the ASME International Mechanical Engineering Congress and Exhibition*, Anaheim, CA, pp. 249-56, 1998.

[36]

Zilles, C.B. and Salisbury, J.K., "A Constraint-based God-object Method for Haptic Display," *Proc. IEEE/RSJ Int. Conf. on Intelligent Robots and Systems*, Pittsburgh, PA, pp. 146-151, 1995.

[37]

Ruspini, D.C., Kolarov, K., and Khatib, O., "The Haptic Display of Complex Graphical Environments," *Computer Graphics Proceedings, SIGGRAPH '97*, Los Angeles, 345-352, 1997.

[38]

Yoshikawa, T., Yokokohji, Y., Matsumoto, T., Zheng, X.-Z., "Display of Feel for the Manipulation of Dynamic Virtual Objects," *Trans. ASME, Journal of Dynamic Systems, Measurement, and Control*, vol. 117, no. 4, pp. 554-8, 1995.

[39]

Kuh, E.S. and Rohrer, R.A., *Theory of Linear Active Networks*, San Francisco: Holden-Day, Inc., 1967.

[49]

Hayward, V., Choksi, J., Lanvin, G., and Ramstein, C., "Design and Multi-Objective Optimization of a Linkage for a Haptic Interface," *Advances in Robot Kinematics and Computational Geometry*, Boston: Kluwer Academic, pp. 352-359, 1994.

[50]

Yokokohji, Y., Hollis, R.L., and Kanade, T., "What You See Is What You Can Feel-Development of a Visual/Haptic Interface to Virtual Environment," *Proc. IEEE Virtual Reality Annual Int. Symposium*, Los Alimitos, CA, pp. 46-53, 1996.

[51]

Clover, C.L., Luecke, G.R., Troy, J.J., and McNeely, W.A., "Dynamic Simulations of Virtual Mechanisms with Haptic Feedback Using Industrial Robotics Equipment," *Proc. IEEE Int. Conf. Robotics and Automation*, Albuquerque, NM, pp. 3205-10, 1997.

[52]

Colgate, J.E. and Brown, J.M., "Factors Affecting the Z-Width of a Haptic Display," *Proceedings of the IEEE International Conference on Robotics and Automation*, San Diego, CA, , pp. 3205-10, 1994.

[53]

Adams, R.J. and Hannaford, B., "Stable Haptic Interaction with Virtual Environments," *IEEE Transactions on Robotics and Automation*, vol. 15, No. 3, pp. 465-474, 1999.

[54]

Anderson, R.J., "Modular Architecture for Robotics and Teleoperation," U.S. Patent 5581666, 1996.

[55]

Kazerooni, H., "Human/Robot Interaction via the Transfer of Power and Information Signals, Part I: Dynamics and Control Analysis," *Proceedings IEEE Int. Conf. Robotics and Automation*, Scottsdale, AZ, pp. 1632-40, 1989.

[56]

Ly, J.H., Safonov, M.G., and Chiang, R.Y., "Real/Complex Multivariable Stability Margin Computation via Generalized Popov Multiplier-LMI Approach," *Proc. of the ACC*, Baltimore, MD, pp. 425-9, 1994.

[57]

Glosser, G.D. and Newman, W.S., "The Implementation of a Natural Admittance Controller on an Industrial Robot," *Proceedings of the IEEE International Conference on Robotics and Automation*, San Diego, CA, pp. 1209-15, 1994.

[58]

Moreyra, M. R., "Design of a Planar High Bandwidth Force Display with Force Sensing," M.S. Thesis, University of Washington, Department of Electrical Engineering, Seattle, 1996.

[59]

Adams, R.J., Moreyra, M.R., Hannaford, B., "Excalibur - A Three Axis Force Display," to appear in *Proc. ASME International Mechanical Engineering Congress and Exhibition*, Nashville, TN, 1999.

[60]

Loftin, R.B., and Kenney, P.J., "Training the Hubble Space Telescope Flight Team," *IEEE Computer Graphics and Applications*, vol. 15, no. 5, pp. 31-37, Sep, 1995.

[61]

Mastaglio, T.W., and Callahan, R., "A Large-Scale Complex Virtual Environment for Team Training," *Computer*, vol. 28, no. 7, pp. 49-56, July, 1995.

[62]

McLin, D.M., and Chung, J.C., "Combining Virtual Reality and Multimedia Techniques for Effective Maintenance Training," *Proceeding of the 24th AIPR Workshop: Tools and Techniques for Modeling and Simulation*, SPIE, vol. 2645, pp. 204-210, 1996.

[63]

Kenyon, R.V., and Afenya, M.B., "Training in Virtual and Real Environments," *Annals of Biomedical Engineering*, vol. 23, pp. 445-455, 1995.

[64]

Kozak, J.J., Hancock, P.A., Arthur, E.J., and Chrysler, S.T., "Transfer of Training from Virtual Reality," *Ergonomics*, vol. 26, pp. 777-784, 1993.

[65]

Philbin, D.A., Ribarsky, W., Walker, N., and Hubbard, C.E., "Training in Virtual Environments: Analysis of Task Appropriateness," *Proceeding of the IEEE 1998 Virtual Reality Annual International Symposium*, pp. 210, 1998

[66]

Pitrella, F.D., and Kruger, W., "Design and Validation of Matching Tests to Form Equal Groups for Tracking Experiments," *Ergonomics*, vol. 26, no. 9, pp. 833-845, 1983.

[67]

Cobb, George W., *Design and Analysis of Experiments*, New York, NY: Springer, 1997.

## VITA

Richard J. Adams  
Captain, USAF

## EDUCATION

**M.S. in Aeronautics and Astronautics**

University of Washington, 1990

**B.S. in Engineering Sciences**

U.S. Air Force Academy, 1989

## EXPERIENCE

Jul 94 - Aug 96

**Exchange Scientist, Engineer and Scientist Exchange Program**  
Automatic Control Department  
Centre d'Etudes et de Recherches de Toulouse  
CERT-ONERA, Toulouse France

Jan 91 - Dec 93

**Senior Stability and Control Engineer**  
Control Analysis Section, Flight Dynamics Directorate,  
Wright Laboratory, Wright-Patterson AFB, OH

## AWARDS

**Distinguished Graduate**, U.S. Air Force Academy, Jun 89

**General Foulois Award**, 480 member Flight Dynamics  
Directorate's highest award for engineering excellence,  
Wright Laboratory, Apr 94

**Scientific Achievement Award**, from USAF for development of a  
full envelope flight control system design technique, Apr 94.

**AIAA Best Paper Award**, first author of best paper in conference  
at the 1994 AIAA Guidance, Navigation, and Control  
Conference, "Active Vortex Flow Control for Vista F-16  
Envelope Expansion," Aug 95.

## PUBLICATIONS

### Monographs

Adams, R.J., Buffington, J.M., Sparks, A.G., and Banda, S.S., *Robust Multivariable Flight Control*, Springer-Verlag, London, 1994.

### Journal Papers

Adams, R.J. and Banda S.S., "Combined LQG and  $H_\infty$  Control of a Benchmark Problem," *Journal of Guidance, Control, and Dynamics*, vol. 15, No. 5, 1992, pp. 1134-39.

Adams, R.J., Sparks, A.G., and Banda S.S., "Full Envelope Mutivariable Control Law Synthesis for a High Performance Test Aircraft," *Journal of Guidance, Control, and Dynamics*, vol. 16, No. 5, 1993, pp. 948-955.

Adams, R.J., Buffington, J.M., and Banda S.S., "Implementation of a Full Envelope PID Controller for a High Performance Fighter Aircraft," *Journal of Guidance, Control, and Dynamics*, vol. 17, No. 3, 1994, pp. 578-583.

Adams, and Banda S.S., "Robust Flight Control Design Using Dynamic Inversion and Structured Singular Value Synthesis," *IEEE Transactions on Control Systems Technology*, vol. 1, No. 2, 1993, pp. 80-92.

Osborne, R.C., Adams, R.J., Hsu, C.S., and Banda, S.S., "Reduced Order  $H_\infty$  Compensator Design for an Aircraft Control Problem," *Journal of Guidance, Control, and Dynamics*, vol. 17, No. 2, 1994, pp. 341-345.

Adams, R.J., Buffington, J.M., and Banda S.S., "Design of Nonlinear Control Laws for High Angle-of-Attack Flight," *Journal of Guidance, Control, and Dynamics*, vol. 17, No. 4, 1994, pp. 737-746.

Buffington, J.M. and Adams, R.J., "Nonlinear Vortex Flow Control for High Angle-of-Attack Maneuvering," *Control Engineering Practice*, vol.3, No.5, 1995, pp. 631-642.

Berg, J., Adams, R.J., Malas, J.C., and Banda, S.S., "Nonlinear Optimization-Based Design of Ram Velocity Profiles for Isothermal Forging," *IEEE Transactions on Control Systems Technology*, vol. 3, No. 3, 1995, pp. 269-278.

Adams, R.J., "Improved Scaling Functions for Robust Synthesis," *International Journal of Robust and Nonlinear Control*, vol. 8, No. 3, 1998, pp. 231-245.

Apkarian, P. and Adams, R.J., "Advanced Gain-Scheduling Techniques for Uncertain Systems," *IEEE Transactions on Control Systems Technology*, vol. 6, No. 1, 1998, pp. 21-32.

Adams, R.J. and Hannaford, B., "Stable Haptic Interaction with Virtual Environments," *IEEE Transactions on Robotics and Automation*, vol. 15, No. 3, 1999, pp. 465-474.

### Conference Papers

Adams, R.J. and Banda S.S., "An  $H_\infty$  Constrained Robust  $H_2$  Solution for a Benchmark Problem," *Proceeding of the 1992 American Control Conference*, pp. 2049-52, Chicago, 1992.

Adams, R.J., Sparks, A.G., and Banda S.S., "A Gain Scheduled Multivariable Design for a Manual Flight Control System," *Proceedings of the 1992 IEEE Conference on Control Applications*, pp. 584-589, Dayton, 1992.

Sparks, A.G., Adams, R.J., and Banda S.S., "Control Law Development for the Lateral Axis of a Fighter Aircraft," *Proceedings of the 1992 AIAA Guidance, Navigation, and Control Conference*, pp. 506-516, Hilton Head, 1992.

Adams, R.J., Buffington, J.M., and Banda S.S., "Gain Scheduled Linear PID Autopilot for the AIAA Controls Design Challenge Aircraft," *Proceedings of the 1992 AIAA Guidance, Navigation, and Control Conference*, pp. 1548-1558, Hilton Head, 1992.

Adams, R.J., and Banda S.S., "An Integrated Approach to Flight Control Design Using Dynamic Inversion and m-Synthesis," *Proceeding of the 1993 American Control Conference*, pp. 1385-89, San Francisco, 1993.

Buffington, J.M., Adams, R.J., and Banda S.S., "A Robust, Nonlinear, High Angle-of-Attack Control Design for a Supermaneuverable Vehicle," *Proceedings of the 1993 AIAA Guidance, Navigation, and Control Conference*, pp. 690-700, Monterey, 1993.

Berg, J., Adams, R.J., and Banda, S.S., "Design of Ram Velocity Profiles for Isothermal Forging via Nonlinear Optimization," *Proceeding of the 1994 American Control Conference*, pp. 323-7, Baltimore, 1994.

Adams, R.J., Buffington, J.M., and Banda S.S., "Active Vortex Flow Control for VISTA F-16 Envelope Expansion," *Proceedings of the 1994 AIAA Guidance, Navigation, and Control Conference*, Scottsdale AZ, 1994, AIAA Paper 4-3681. (AIAA Award for Best Paper in Conference)

Adams, R.J. and Chrétien, J-P., "Non-Conservative Robustness Analysis for Second-Order Systems," *Proceedings of the 1995 American Control Conference*, pp. 3866-70, Seattle, 1995.

Adams, R.J., Chrétien, J-P., and Spillman, M., "Enhanced m-Synthesis Through Improved D-Scalings," *Proceedings of the 1995 Conference on Decision and Control*, pp. 3121-22, New Orleans, 1995.

Adams, R.J., Apkarian, P., and Chrétien, J-P., "Robust Control Approaches for a Two-Link Flexible Manipulator," *Proceedings of the 3rd International Conference on Dynamics and Control of Structures in Space*, pp. 101-117, Cranfield, U.K., 1996.

Apkarian, P. and Adams, R.J., "Advanced Gain-Scheduling Techniques for Uncertain Systems," *Proceedings of the 1997 American Control Conference*, pp. 3331 -35, Albuquerque, 1997.

Adams, R.J. and Hannaford, B., "A Two-Port Framework for the Design of Unconditionally Stable Haptic Interfaces," *Proceedings of the 1998 IEEE/RSJ International Conference on Intelligent Robots and Systems*, pp. 1254-9, Victoria, B.C., 1998.

Adams, R.J., Moreyra, M., and Hannaford, B., "Stability and Performance of Haptic Displays: Theory and Experiments," *Proceedings of the ASME International Mechanical Engineering Congress and Exhibition*, pp. 227-34., Anaheim, CA, 1998.